

Crystallography of TWIP Steel

By

Bo Qin

Graduate Institute of Ferrous Technology

Pohang University of Science and Technology

San 31, Hyoja-Dong, Nam-gu, Pohang, Kyungbuk

Republic of Korea

A dissertation submitted for the

degree of Master of Engineering

at Pohang University of Science and Technology

July 2007

Preface

This dissertation is submitted for the degree of Master of Engineering in Computational Metallurgy at Pohang University of Science and Technology. The research described herein was conducted under the supervision of Professor H. K. D. H. Bhadeshia, Adjunct Professor of Computational Metallurgy in the Graduate Institute of Ferrous Technology, Pohang University of Science and Technology and Professor of Physical Metallurgy, University of Cambridge, between May 2006 and June 2007.

This work is to the best of my knowledge original, except where acknowledgements and references are made to previous work. Neither this, nor any substantially similar dissertation has been or is being submitted for any other degree, diploma or other qualification at any other university.

Bo Qin
June 2007

Acknowledgements

I am extremely grateful to my supervisor, Professor H. K. D. H. Bhadeshia, for his constant guidance, support, great friendship and for his unique and charming way of teaching the simplicity and beauty of science.

I would like to express my sincere thanks to all the people in the Graduate Institute of Ferrous Technology in Pohang University of Science and Technology, especially those members in Computational Metallurgy Laboratory, for all their help and for all the happiness we shared.

I acknowledge Professor Hae-Geon Lee from whom I learnt about this project, and POSCO from which I got a scholarship to pursue this M. Eng. degree.

I would also like to thank all the members of Phase Transformation and Complex Properties Research Group for their friendship and assistance during my stay in the University of Cambridge. Especially I want to thank Dr. Saurabh Kundu for his help and for all the discussions with him.

I thank all my friends for their encouragement and friendship.

Special thanks to Ying from whom I have always got peace, strength, and through whom I have strengthened my faith.

Finally, I would like to take this opportunity to express my gratitude to my family members for their love, unfailing encouragement and support.

Abstract

Austenitic twinning induced plasticity (TWIP) steels have low to intermediate stacking fault energy and hence undergo extensive mechanical twinning during deformation, which in turn leads a good combination of both strength and ductility. Considerable experimental research has been conducted to examine its microstructure and texture evolution, and a limited amount of work has also been done to model its work-hardening behavior. However, no attempt exists to quantitatively estimate the strain from twinning and to qualitatively estimate the resulting texture change during the deformation of polycrystalline austenitic TWIP steel. The present work is aimed at solving this problem.

A physical model based on the mathematical geometry of crystallography of mechanical twinning has been developed in this work and computer programs have been written to implement the calculations. The results give the exact values of true strain due to twinning, which is a function of the volume fraction of twin plates, matrix texture and intensity of texture. Compared with experimental results on ductility, which is generally above 85% elongation, the calculated true strain is substantially smaller, consistent with the occurrence of mechanisms of plastic deformation other than twinning.

The attempt to calculate the texture change is partially successful because the twinning mode only dominates at low strains, for instance during tensile testing with a true strain less than 0.4.

A program of future work has been compiled in the light of these results.

Nomenclature and Abbreviations

Abbreviations

AFM	Atomic force microscopy
BCC	Body-centered cubic
BCT	Body-centered tetragonal
CR	Cold rolling
DP	Dual phase
FCC	Face-centered cubic
FORTRAN	Formula translation
IF	Interstitial free
IPS	Invariant plane strain
ND	Normal direction
ODF	Orientation distribution function
ppm	parts per million
RD	Rolling direction
SFE	Stacking fault energy
TD	Transverse direction
TeD	Tensile direction
TEM	Transmission electron microscopy
TRIP	Transformation induced plasticity
TWIP	Twinning induced plasticity

Nomenclature

ε	True strain
ε_{un}	Uniform elongation
ε_f	Total elongation
$R_{p0.2}$	0.2% proof strength
R_m	Tensile strength

γ_{SFE}	The value of stacking fault energy
γ_{FCC}	The stacking fault energy for austenite
γ	Austenite
\mathbf{a}_i	Basis vectors of basis A
\mathbf{b}_i	Basis vectors of basis B
\mathbf{p}	Unit twinning plane normal
\mathbf{d}	Unit twinning direction
\mathbf{q}	Unit normal of section plane \mathbf{pd}
$(A J B)$	Coordinate transformation matrix between basis A and B
$(A P A)$	Deformation matrix with respect to basis A
J_{ij}	Components of orthonormal 3×3 matrix
s	Twinning shear
σ_{ij}	Normal components of a stress tensor
τ_{ij}	Shear components of a stress tensor
\mathbf{t}	Traction vector
E	Strain energy
M_1	The basis of reference grain in austenite polycrystalline
$M_i (i > 1)$	The basis of ordinary grains in austenite polycrystalline
T_{ij}	The basis of j^{th} favorable twinning system in grain i
G	The basis of single austenite grain
S	The basis of sample reference frame
$(S J M_i)$	The coordinate transformation matrix between sample reference frame and grain i
$(S J T_{ij})$	The coordinate transformation matrix between sample reference frame and j^{th} favorable twin in grain i
\mathbf{b}	The Burger's vector of dislocation

\mathbf{b}_p	The Burger's vector of partial dislocation
α	The angle between vector \mathbf{u} and basis axis \mathbf{a}_1
β	The angle between vector \mathbf{u} and basis axis \mathbf{a}_2
δ	The angle between vector \mathbf{u} and basis axis \mathbf{a}_3
α_i	The angles between basis axis \mathbf{b}_i of B and basis axis \mathbf{a}_1 of A
β_i	The angles between basis axis \mathbf{b}_i of B and basis axis \mathbf{a}_2 of A
δ_i	The angles between basis axis \mathbf{b}_i of B and basis axis \mathbf{a}_3 of A
(ϕ, θ, ψ)	Euler angles, mathematic representation
$(\varphi_1, \Phi, \varphi_2)$	Euler angles, texture analysis representation
η_i	Compression / expansion ratio of Bain strain along \mathbf{b}_i
p_i	Components of unit twinning plane normal \mathbf{p}
d_i	Components of unit twinning direction \mathbf{d}
q_i	Components of unit normal of section plane \mathbf{pd}
a_γ	Austenite lattice parameter
d_{111}	Interplannar distance of plane (111)

Contents

Chapter 1	1
Introduction.....	1
1-1 Strength and ductility	1
1-2 TWIP steel.....	2
1-3 Why twinning occurs	3
1-4 Objectives.....	6
Chapter 2	8
Geometry of Crystallography	8
2-1 Crystal structure and definition of a Basis	8
2-2 Representation of rotation matrix.....	10
2-2-1 Direction cosine matrix	10
2-2-2 Rotation axis-angle pairs.....	12
2-2-3 Euler angles.....	13
2-3 Homogeneous deformation	15
2-3-1 Similarity transformation	16
2-3-2 Deformation matrix in mechanical twinning.....	17
2-4 Texture representation.....	18
2-4-1 Pole figures.....	18
2-4-2 Orientation distribution function.....	21
Chapter 3	23
Simulation of Twinning	23
3-1 Twinning in FCC.....	23
3-2 Twinning shear, deformation matrix and orientation relationship of twin	25
3-3 Criterion for the initiation of mechanical twinning.....	28
3-4 The calculation	29
3-4-1 The calculation of strain.....	31
3-4-2 The calculation of texture.....	33
Chapter 4.....	35
Results and Discussions.....	35
4-1 Texture	35
4-1-1 Modeling of important orientations in FCC orientations	35
4-1-2 Twinning effect on textures.....	44
4-1-3 Comparison with experimental results	51

Cold rolling	51
Tensile testing.....	53
4-2 True Strain.....	61
4-2-1 Orientation dependence of strain, single crystal.....	61
4-2-2 Dependence of strain on twinning system.....	68
4-2-3 Dependence of strains on texture	71
4-2-4 Comparison with literature data	79
4-2-5 Multi-axial stresses.....	80
4-3 Conclusions.....	83
4-3-1 The strain.....	83
4-3-2 The texture	83
Chapter 5	85
Summary and Future Work.....	85
5-1 Summary	85
5-2 Future work.....	86
Appendix A	89
Appendix B	97
Bibliography	100

Chapter 1

Introduction

Austenitic steels are used widely in many applications because of their excellent strength and ductility, good wear resistance and corrosion resistance [Lacombe et al., 1993; Bhadeshia and Honeycombe, 2006]. In the automotive industries, it is always useful to make components light and efficient. This can be achieved using novel steels with improved strength and formability.

TWIP (Twinning-Induced Plasticity) steels have exceptionally good combinations of strength, ductility and damage tolerance which satisfy the requirements for automotive industries [Grassel and Frommeyer, 1998]. There have been some investigations of its mechanical properties [Grassel *et al.*, 2000; Frommeyer *et al.*, 2003; Vercammen *et al.*, 2004a; Yang *et al.*, 2006] and of high work hardening rate [Bouaziz and Guelton, 2001; Allain *et al.*, 2004a]. However the contribution of mechanical twinning to total elongation is only qualitatively understood and there has been no method for predicting the evolution of texture due to twinning. This chapter is a review of TWIP steels to set the context for the research presented later.

1-1 Strength and ductility

Steels have variety of properties and applications but its success in engineering structures comes from the combination of strength, ductility and ease of manufacture. For some time now, increases of strength could not be combined with an increase in ductility, leading to an empirical ‘law’ that the product of strength and ductility is a constant. The challenge is to overcome this law and produce better steels. Some successes come from collaborative research [IISI, 2006] which leads to steels such as transformation induced plasticity (TRIP) steel and dual-phase (DP) steel, as illustrated in Figure 1-1.

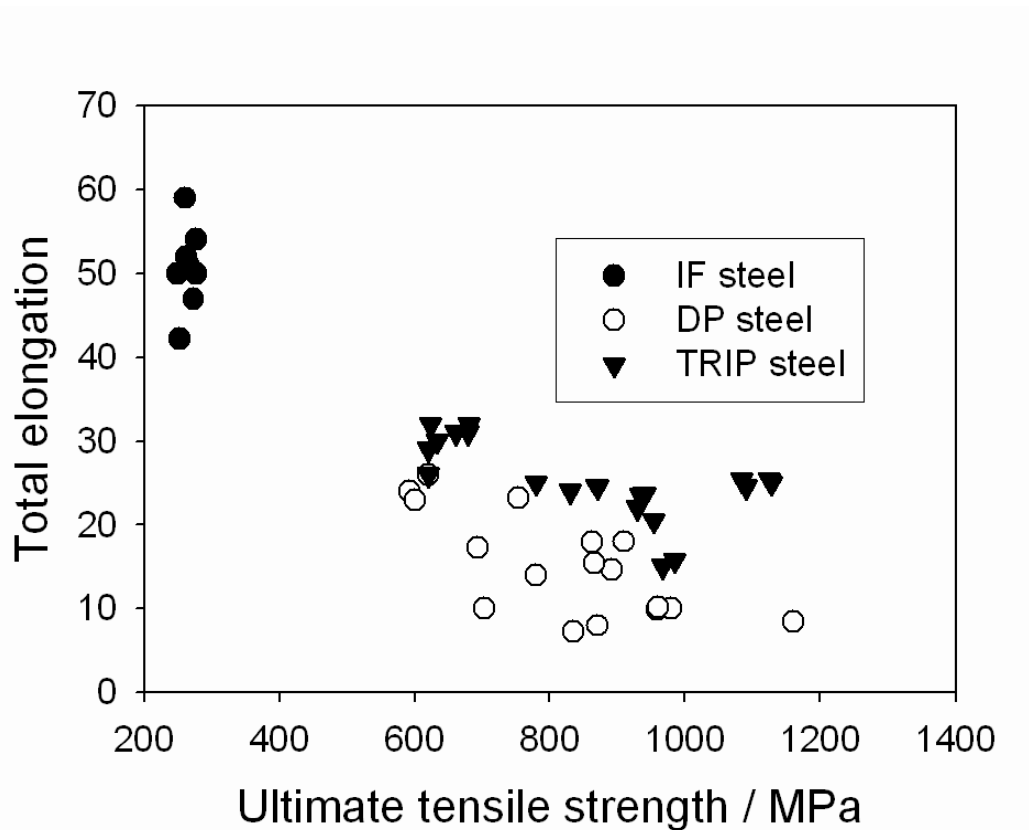


Fig. 1-1: Strength-elongation relationships for some steels. DP: dual-phase steel; TRIP: transformation induced steel. Intestinal free (IF) steel is listed for comparasion [Sun and Pugh, 2002; Decooman, 2004; Adamczyk and Grajcar, 2005; Lis *et al.*, 2005; Srivastava *et al.*, 2006; Panda *et al.*, 2007; Sarwar *et al.*, 2007; Srivastava *et al.*, 2007; Wei *et al.*, 2007; Zhao *et al.*, 2007].

TRIP steels outperform the others with a microstructure of ferrite, bainite and retained austenite. During deformation the austenite transforms into martensite, thus enhancing the work hardening rate and ensuring a greater extent of uniform elongation. It is worth emphasizing that the plasticity from the shape deformation due to martensitic transformation is limited, so it is more meaningful to call such alloys TRIP-assisted rather than TRIP steels [Bhadeshia, 2002].

1-2 TWIP steel

About ten years ago, a steel based on plasticity induced by mechanical twinning (TWIP), with a remarkable combination of strength and ductility was discovered. According to experiments, it can achieve 800 MPa with a total elongation above 85%

[Grassel and Frommeyer, 1998]. These values vary with deformation temperature, strain rate and chemical composition [Grassel *et al.*, 2000; Frommeyer *et al.*, 2003]. Figure 1-2 shows the mechanical properties of Fe-20Mn-3Al-3Si wt. % TWIP steel. Its properties are a function of the test temperature. Near room temperature, its uniform elongation (ϵ_{un}) and total elongation (ϵ_f) reach maximum, at 78% and 88%, respectively.

The high elongation is due to the maintenance of work-hardening rate, as shown in Figure 1-3. Compared with the stress strain curve of TRIP steel, there is no drastic change in curvature for TWIP steel.

It is possible by using optical and transmission electron microscopy (TEM) to characterize the microstructure of TWIP steel, as shown in Figure 1-4. Twins are evident as thin plates inside the austenite matrix. The twinning is responsible for maintaining the work-hardening rate by hindering the glide of dislocations.

1-3 Why twinning occurs

The main difference between TRIP-assisted and TWIP steel is that the austenite in the former is stable on cooling but not under mechanical load, i.e. phase transformation happens when the material is loaded. In contrast, there is no phase transformation in a TWIP steel during cooling or deformation, but the orientation of part of austenite will change due to mechanical twinning. The different behavior of the austenite is attributed to its stacking fault energy.

The crystal can be seen as a stack of close-packed layers of atoms arranged in a periodic sequence. However the sequence may contain errors, called stacking faults. Like all defects, a stacking fault causes a change in energy, called stacking fault energy (SFE), denoted γ_{SFE} ($J m^{-2}$). SFE changes with the alloy composition and deformation temperature. Its magnitude controls the ease of cross-slip of dislocations and thus different mechanisms can be activated at different stages of deformation. As SFE decreases the faults become wider and cross-slip more difficult and mechanical twinning is hence becoming the favoured deformation mode [Hull and Bacon, 2001].

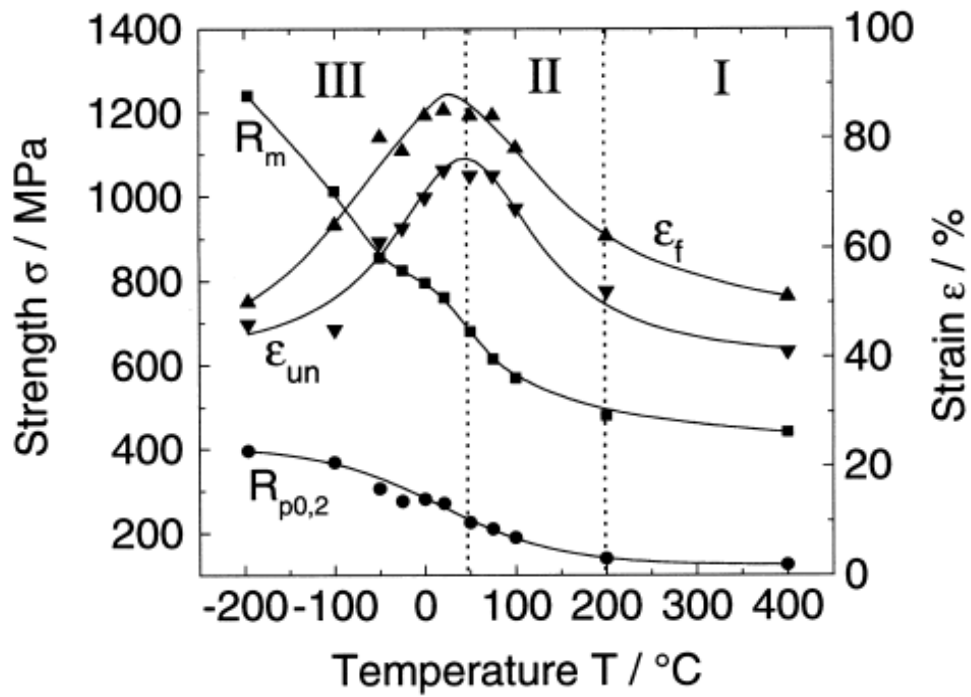


Fig. 1-2: Dependence of 0.2% proof strength ($R_{p0.2}$), tensile strength (R_m), uniform elongation (ϵ_{un}) and total elongation (ϵ_f) on temperature. Fe-20Mn-3Al-3Si wt. % TWIP steel [Frommeyer *et al.*, 2003].

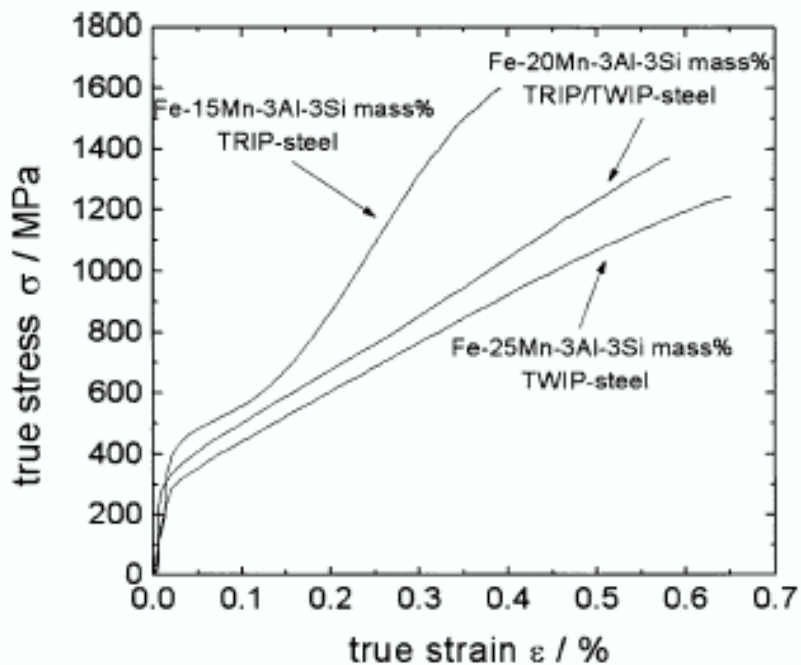
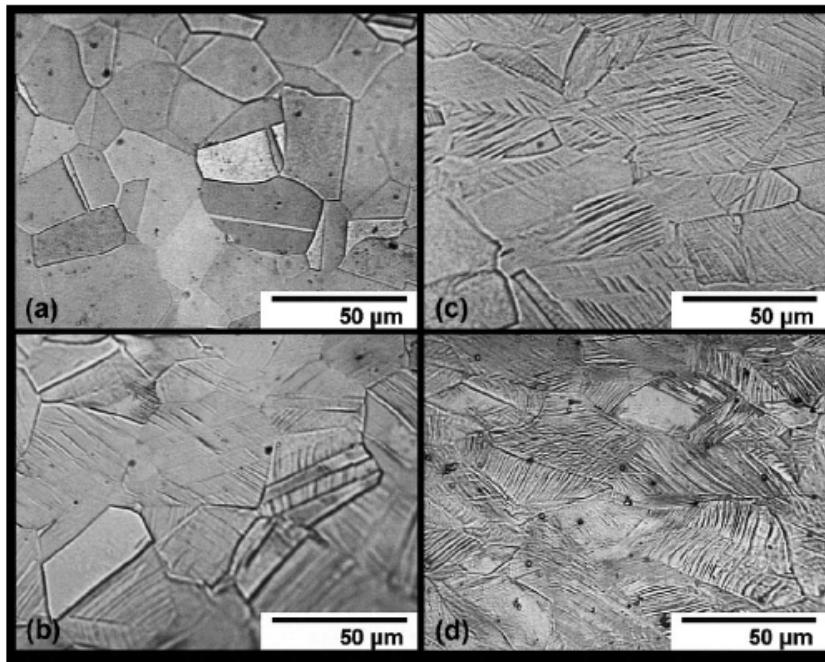
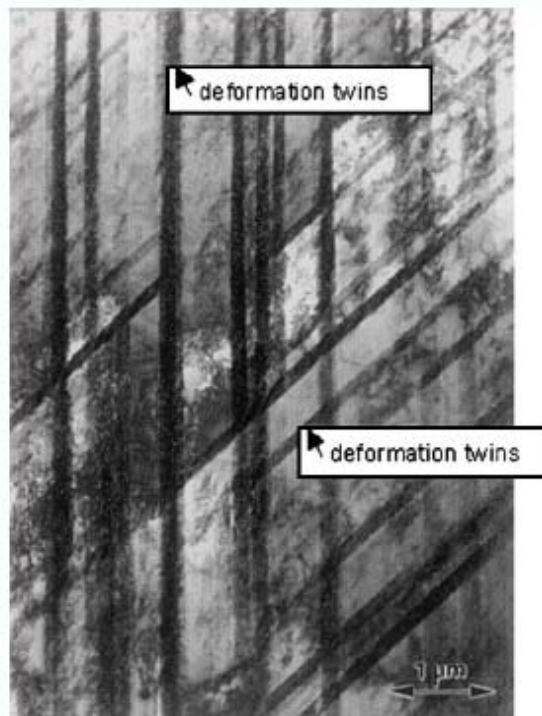


Fig. 1-3: True stress vs. true strain curves of the TRIP and TWIP steels. Test temperature: 20°C; strain rate: 10^{-3}s^{-1} [Frommeyer *et al.*, 2003].



(a-d)



(e)

Fig. 1-4: Microstructure of TWIP steel: (1) Optical micrographs of typical TWIP steel (a) unstrained, (b) 18% strain, (c) 26% strain, (d) 34% strain [Allain *et al.*, 2004b]; (e) Bright field transmission electron micrograph illustrating deformation twins on two intersecting $\{111\}$ planes [Frommeyer *et al.*, 2003].

However, at very low stacking fault energies, strain-induced epsilon martensite becomes predominant [Christian and Mahajan, 1995]. Low SFE ($\gamma_{\text{FCC}} < 16 \text{ mJ m}^{-2}$) favors the $\gamma \rightarrow \epsilon$ transformation in FCC [Ishida and Nishizawa, 1974] while higher SFE suppresses this transformation.

Table 1-1 lists the stacking fault energy and deformation modes for some materials. It is evident that mechanical twinning becomes favorable at low SFE range.

Other parameters such as the shear modulus or grain size also influence the deformation mechanisms, for instance as shown in Table 1-1, mechanical twinning has been found in nanocrystalline aluminum [Chen *et al.*, 2003], whereas in coarse-grained pure aluminum, it has never been observed.

TWIP steels usually contain large concentrations of Mn. Its typical composition is 3 Si, 3 Al, and more than 20 Mn, in wt. %. Table 1-2 lists the compositions of some TRIP / TWIP steels used in experiments. When the manganese concentration is 15 wt. %, only TRIP effects was observed whereas when it is 20 wt. %, both TWIP and TRIP effects were found. The exact concentrations may vary subject to the other alloying elements used. In general, as additional elements, Mn is used to stabilize the austenite and at the same time to reduce the stacking fault energy; aluminum to raise the SFE and silicon to reduce it.

By changing the composition and deformation temperature, the stacking fault energy can be adjusted to the range where mechanical twinning favours. This energy for TWIP steel is found usually less than 25 mJ m^{-2} , but higher than 16 mJ m^{-2} , below which the formation of hexagonal close-packed ϵ is favoured [Frommeyer *et al.*, 2003].

1-4 Objectives

Thin mechanical twin plates with different orientations are generated in the austenite of TWIP steel during deformation. Obviously, differently oriented twins contribute to different extents to the total elongation. At the same time, the whole piece of steel cannot be completely twinned, and there appears to be a saturation volume fraction of twinning which is experimentally proved by Karaman and Choi in Hadfield steel [Choi *et al.*, 1999; Karaman *et al.*, 2002]. On the other hand, the

orientation of the matrix austenite can be changed due to rotation and mechanical twinning in the course of deforming. So one objective of this work is to calculate the elongation from twinning itself by using mathematical crystallography; another one is to calculate the texture of TWIP steel, for different stress states. An expected outcome is the ability to predict the full plastic strain in all directions for an arbitrary stress tensor.

Table 1-1: Stacking fault energies (γ_{SFE}) of several materials and their deformation modes [Karaman *et al.*, 1998; Pan *et al.*, 1998; El-Danaf *et al.*, 1999; Chen *et al.*, 2003].

Alloy code	composition / wt. %	$\gamma_{SFE} / \text{mJ m}^{-2}$	deformation mode
MP35N	35Ni-35Co-20Cr-10Mo	13	Disl. / twin
70/30 Brass	70Cu-30Zn	7	Disl. / twin
80/20 Brass	80Cu-20Zn	9	Disl. / twin
90/10 Brass	90Cu-10Zn	18	Disl. / twin
Hadfield Steel	12.34Mn-1.03C-Fe balance	25	Disl. / twin
Magnesium	Mg	125	Disl.
Zinc	Zn	140	Disl.
Aluminum	AL	166	Disl. / twin

Table 1-2: Typical composition of TRIP / TWIP steel [Grassel *et al.*, 2000; Meng *et al.*, 2007].

Mn / wt. %	Si / wt. %	Al / wt. %	C / ppm	Fe / wt. %	steel category
15.8	3.3	2.9	200	bal.	TRIP
20.1	2.8	2.9	400	bal.	TWIP / TRIP
26.5	3.0	2.8	300	bal.	TWIP
29.2	3.0	2.8	200	bal.	TWIP
33.0	3.0	2.93		bal.	TWIP

Chapter 2

Geometry of Crystallography

Deformation strains and texture changes are related to the changes of the lengths and orientations of vectors in the austenite matrix during the process of mechanical twinning. To simulate this requires mathematical crystallography based on matrix algebra. This chapter contains the background to this geometry of crystals.

2-1 Crystal structure and definition of a basis

In the calculation of strains, it is necessary to specify the directions and magnitudes of vectors to discover how they change during deformation. To estimate texture, it is necessary to specify the orientation of a grain within the sample reference frame. There will therefore be two bases, one defined with respect to the crystal structure and a second to represent the sample shape.

Figure 2-1 (a) shows the unit cell of austenite. Three vectors parallel to the unit cell edges and of magnitude equal to the austenitic lattice parameter form the crystallographic basis, as shown in Figure 2-1 (b).

The set of vectors \mathbf{a}_i ($i = 1, 2, 3$) are called the basis vectors and the basis itself can be identified by a basis symbol A . Now, any vector \mathbf{u} in the structure can then be written as:

$$\mathbf{u} = u_1 \mathbf{a}_1 + u_2 \mathbf{a}_2 + u_3 \mathbf{a}_3$$

where u_1, u_2, u_3 are its components in the basis A .

These components of line vector can conveniently be written as a single column matrix:

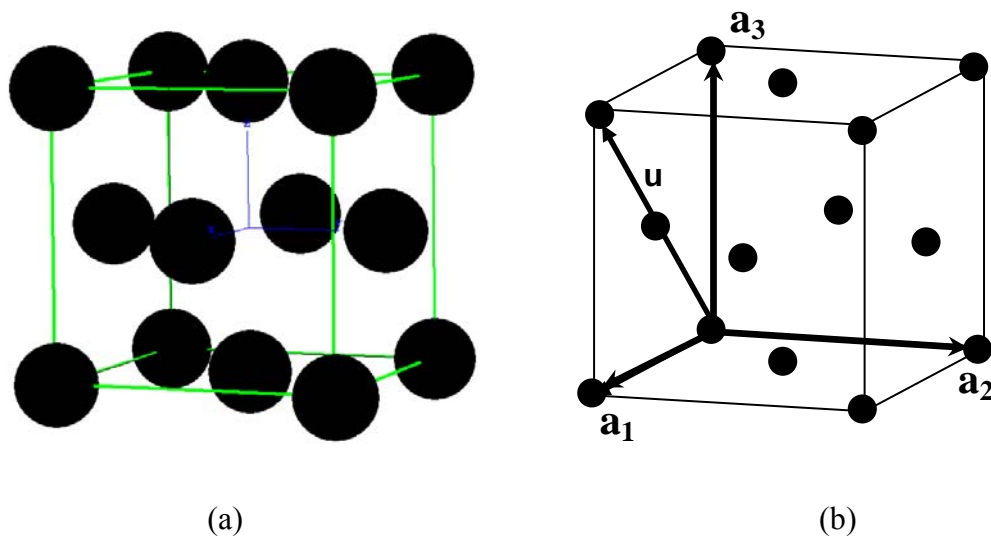


Fig. 2-1: (a) Austenite structure; (b) Coordinate system representing the lattice.

$$\begin{bmatrix} u_1 \\ u_2 \\ u_3 \end{bmatrix}$$

However, for the convenience, this can also be written using square brackets as $[u_1 \ u_2 \ u_3]$. It follows from this that the matrix representation of the vector \mathbf{u} with respect to the basis \mathbf{A} is $[\mathbf{A}; \mathbf{u}] = [u_1 \ u_2 \ u_3]$. For instance in Figure 2-1(b),

$$[\mathbf{A}; \mathbf{u}] = [1 \ 0 \ 1].$$

A single row matrix $(u_1 \ u_2 \ u_3)$ with round brackets can also be used to represent the vector \mathbf{u} , which is $(\mathbf{u}; \mathbf{A}) = (u_1 \ u_2 \ u_3)$. Notice that the column matrix $[\mathbf{A}; \mathbf{u}]$ is the transpose of row matrix $(\mathbf{u}; \mathbf{A})$.

The external shape of the specimen determines a specific coordinate system. In the case of rolled sheet steel, it is normal to choose a coordinate system \mathbf{S} whose axes \mathbf{s}_1 , \mathbf{s}_2 and \mathbf{s}_3 lie along the rolling direction (RD), transverse direction (TD) and normal direction (ND) of the sheet, respectively, as shown in Figure 2-2

The preference of crystallographic orientation of each grain within the sample is the essence of texture. There are usually two ways to represent texture, the pole figure and the orientation distribution function, both of which will be discussed later in this chapter.

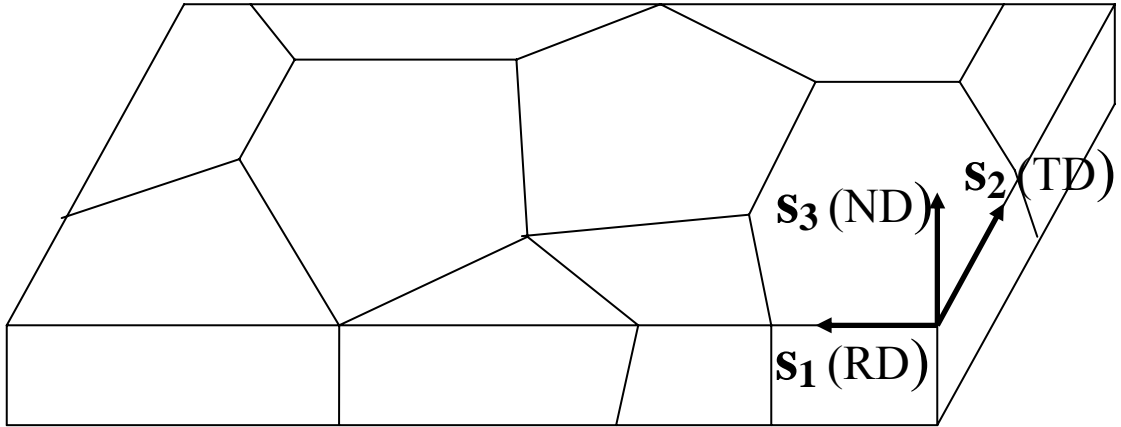


Fig. 2-2: Sample reference frame.

2-2 Representation of rotation matrix

2-2-1 Direction cosine matrix

The components of any vector \mathbf{u} , i.e. $[u_1 \ u_2 \ u_3]$, together with the basis vectors, give its orientation and magnitude. For an orthonormal basis, a new unit vector parallel to \mathbf{u} can be obtained by normalizing the vector as

$$\left[\frac{u_1}{\sqrt{u_1^2 + u_2^2 + u_3^2}} \quad \frac{u_2}{\sqrt{u_1^2 + u_2^2 + u_3^2}} \quad \frac{u_3}{\sqrt{u_1^2 + u_2^2 + u_3^2}} \right]$$

or

$$[\cos \alpha \quad \cos \beta \quad \cos \delta]$$

where α , β , δ are the angles between \mathbf{u} and \mathbf{a}_1 , \mathbf{a}_2 and \mathbf{a}_3 , respectively. $\cos \alpha$, $\cos \beta$ and $\cos \delta$ are called the direction cosines of \mathbf{u} .

It's evident that the choice of the basis vectors \mathbf{a}_i is arbitrary, though in this case convenient. In the case of orthonormal bases, the orientation of a second basis B can be specified by specifying the direction cosines of its three axes \mathbf{b}_1 , \mathbf{b}_2 and \mathbf{b}_3 in basis A, that is:

$$\mathbf{b}_1 = \cos \alpha_1 \times \mathbf{a}_1 + \cos \beta_1 \times \mathbf{a}_2 + \cos \delta_1 \times \mathbf{a}_3$$

$$\mathbf{b}_2 = \cos \alpha_2 \times \mathbf{a}_1 + \cos \beta_2 \times \mathbf{a}_2 + \cos \delta_2 \times \mathbf{a}_3$$

$$\mathbf{b}_3 = \cos \alpha_3 \times \mathbf{a}_1 + \cos \beta_3 \times \mathbf{a}_2 + \cos \delta_3 \times \mathbf{a}_3$$

where $\alpha_i, \beta_i, \delta_i$ ($i=1,2,3$) are the angles between basis axes \mathbf{a}_i and \mathbf{b}_1 , \mathbf{a}_i and \mathbf{b}_2 , \mathbf{a}_i and \mathbf{b}_3 , respectively

The matrix relating this transform from basis A to basis B is denoted as a rotation matrix (A J B):

$$(A \ J \ B) = \begin{pmatrix} \cos \alpha_1 & \cos \alpha_2 & \cos \alpha_3 \\ \cos \beta_1 & \cos \beta_2 & \cos \beta_3 \\ \cos \delta_1 & \cos \delta_2 & \cos \delta_3 \end{pmatrix}$$

A simple example is rotation of a right handed angle ϕ about a common axis $\mathbf{a}_3 \parallel \mathbf{b}_3$, in which case the rotation matrix can be written as:

$$(A \ J \ B) = \begin{pmatrix} \cos \phi & -\sin \phi & 0 \\ \sin \phi & \cos \phi & 0 \\ 0 & 0 & 1 \end{pmatrix}$$

and when the rotation is about $\mathbf{a}_1 \parallel \mathbf{b}_1$ by angle ψ ,

$$(A \ J \ B) = \begin{pmatrix} 1 & 0 & 0 \\ 0 & \cos \psi & -\sin \psi \\ 0 & \sin \psi & \cos \psi \end{pmatrix}$$

These examples are simple because the rotation and the relationship between A and B are obvious. In fact any rotation matrix (A J B) is orthonormal which means that its transverse equals its inverse and a general rule that each column of a rotation matrix (A J B) represents the components of a corresponding basis vector of B with respect to basis A is always held.

The transformation of components of any vector \mathbf{u} then follows the straightforward rule,

$$[A; \mathbf{u}] = (A \ J \ B) [B; \mathbf{u}] \quad (2-1)$$

or:

$$[B; \mathbf{u}] = (B \ J \ A) [A; \mathbf{u}]$$

where (B J A) is the inverse of (A J B).

2-2-2 Rotation axis-angle pairs

The rotation matrix (A J B) can also be represented by a pair of rotation axis \mathbf{u} and a right handed rotation angle θ . Supposing $\mathbf{u} = [u_1 \ u_2 \ u_3]$ in basis B, if \mathbf{u} happens to lie along the rotation axis relating bases A and B, then not only the components of \mathbf{u} in both bases remain the same, but its direction remains invariant to the rotation operation so that $[\mathbf{B}; \mathbf{u}] = [\mathbf{A}; \mathbf{u}]$. Substituting it into equation 2-1 we get,

$$[\mathbf{B}; \mathbf{u}] = (\mathbf{A} \mathbf{J} \mathbf{B}) [\mathbf{B}; \mathbf{u}]$$

that is,

$$\{(\mathbf{A} \mathbf{J} \mathbf{B}) - \mathbf{I}\} [\mathbf{B}; \mathbf{u}] = 0 \quad (2-2)$$

where I is a 3×3 identity matrix.

It can be proven that equation 2-2 always has non-zero solution as long as the matrix (A J B) is not an identity matrix which represents a null rotation.

The sense and magnitude of the rotation angle θ also need to be specified. Consider the following example. Supposing a rotation matrix is

$$(\mathbf{A} \mathbf{J} \mathbf{B}) = \frac{1}{3} \begin{pmatrix} 2 & 2 & \bar{1} \\ \bar{1} & 2 & 2 \\ 2 & \bar{1} & 2 \end{pmatrix}$$

solving equation 2-2 gives $u_1 = u_2 = u_3$ which means $[1 \ 1 \ 1]_{\mathbf{B}}$ is the rotation axis. A vector $[\mathbf{B}; \mathbf{v}] = [1 \ \bar{1} \ 0]$ which is normal to the rotation axis \mathbf{u} , becomes a new vector $[\mathbf{A}; \mathbf{w}] = [1 \ \bar{1} \ 0]$ due to rotation. The vector \mathbf{w} can then be represented in basis B as $[\mathbf{B}; \mathbf{w}] = (\mathbf{B} \mathbf{J} \mathbf{A}) [\mathbf{A}; \mathbf{w}] = [1 \ 0 \ \bar{1}]$. The cross product of \mathbf{w} and \mathbf{v} gives a vector parallel to $[1 \ 1 \ 1]_{\mathbf{B}}$, which means the rotation was right-handed.

Naturally, if the rotation axis and angle are known, then the rotation matrix can be derived as [Bunge, 1982]:

$$(\mathbf{A} \mathbf{J} \mathbf{B}) = \begin{pmatrix} u_1 u_1 (1 - \cos \theta) + \cos \theta & u_1 u_2 (1 - \cos \theta) + u_3 n & u_1 u_3 (1 - \cos \theta) - u_2 n \\ u_1 u_2 (1 - \cos \theta) - u_3 n & u_2 u_2 (1 - \cos \theta) + \cos \theta & u_2 u_3 (1 - \cos \theta) + u_1 n \\ u_1 u_3 (1 - \cos \theta) + u_2 n & u_2 u_3 (1 - \cos \theta) - u_1 n & u_3 u_3 (1 - \cos \theta) + \cos \theta \end{pmatrix}$$

where u_1, u_2, u_3 are the components of a unit rotation axis and θ is the

corresponding right-handed rotation angle. By this way only three independent values are needed to define the rotation matrix: any two components of the unit rotation axis and one rotation angle.

2-2-3 Euler angles

The rotation relating crystals can also be represented using *Euler angles* (ϕ, θ, ψ) , which split the complete rotation into three constitutive rotations, as shown in Figure 2-3 (a), each of which can be described by rotation matrices.

The first rotation (Figure 2-3 (b)) by a right-handed angle ϕ about \mathbf{a}_3 axis gives a rotation matrix:

$$R_\phi = \begin{pmatrix} \cos \phi & -\sin \phi & 0 \\ \sin \phi & \cos \phi & 0 \\ 0 & 0 & 1 \end{pmatrix} \quad (2-3)$$

the second by θ about the \mathbf{a}_1 (Figure 2-3 (c)) gives:

$$R_\theta = \begin{pmatrix} 1 & 0 & 0 \\ 0 & \cos \theta & -\sin \theta \\ 0 & \sin \theta & \cos \theta \end{pmatrix} \quad (2-4)$$

and the third rotation is by an angle ψ about \mathbf{a}_3 again (Figure 2-3(d)) which gives:

$$R_\psi = \begin{pmatrix} \cos \psi & -\sin \psi & 0 \\ \sin \psi & \cos \psi & 0 \\ 0 & 0 & 1 \end{pmatrix} \quad (2-5)$$

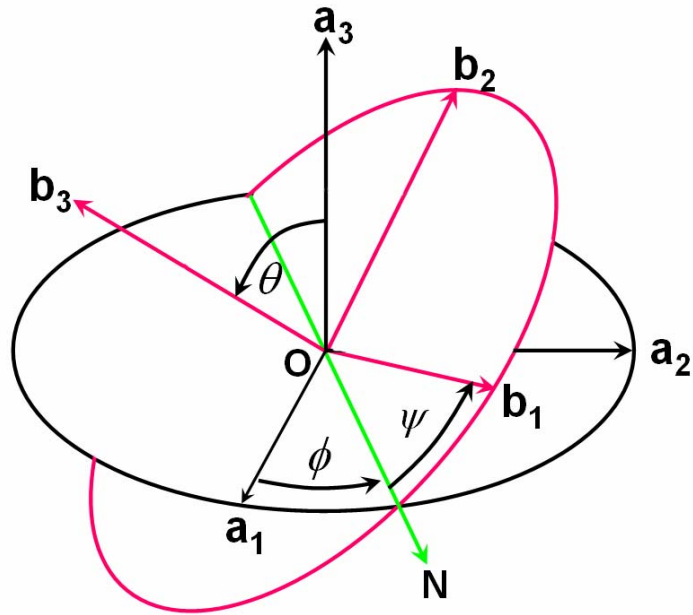
The final effect of these three rotations is

$$(A J B) = R_\psi \times R_\theta \times R_\phi \quad (2-6)$$

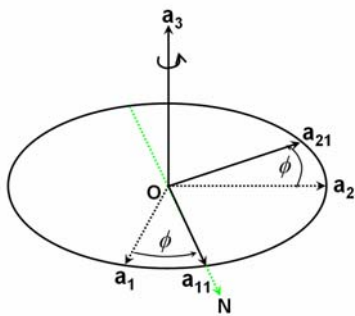
$$(A J B) = \begin{pmatrix} \cos \psi \cos \phi - \cos \theta \sin \phi \sin \psi & \cos \psi \sin \phi + \cos \theta \cos \phi \sin \psi & \sin \psi \sin \theta \\ -\sin \psi \cos \phi - \cos \theta \sin \phi \cos \psi & -\sin \psi \sin \phi + \cos \theta \cos \phi \cos \psi & \cos \psi \sin \theta \\ \sin \theta \sin \phi & -\sin \theta \cos \phi & \cos \theta \end{pmatrix} \quad (2-7)$$

Hence given any orthonormal rotation matrix

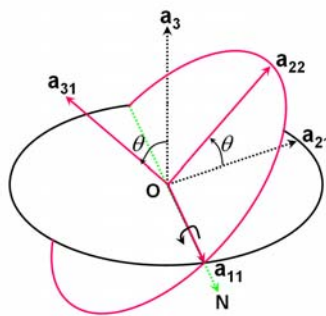
$$(A J B) = \begin{pmatrix} J_{11} & J_{12} & J_{13} \\ J_{21} & J_{22} & J_{23} \\ J_{31} & J_{32} & J_{33} \end{pmatrix} \quad (2-8)$$



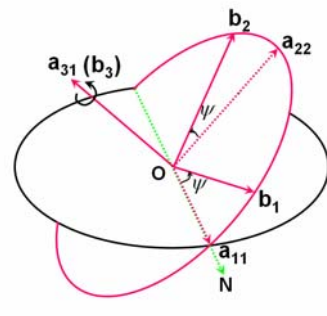
(a)



(b)



(c)



(d)

Fig. 2-3: The split of a complete rotation into three constitutive rotations. Intersection of two planes is called *line of nodes* (\mathbf{ON}). ϕ is the angle between \mathbf{a}_1 and \mathbf{ON} ; ψ is the angle between \mathbf{b}_1 and \mathbf{ON} and θ is the angle between \mathbf{a}_3 and \mathbf{b}_3 . (b) First rotation about \mathbf{a}_3 axis by the angle of ϕ so that \mathbf{a}_1 meets \mathbf{ON} ; (c) second rotation about \mathbf{a}_{11} (rotated \mathbf{a}_1) which lies along \mathbf{ON} , by the angle of θ until \mathbf{a}_3 changes to the position of \mathbf{a}_{31} which is parallel \mathbf{b}_3 ; (d) third rotation about \mathbf{a}_{31} by the angle of ψ when \mathbf{a}_{11} and \mathbf{a}_{22} meet \mathbf{b}_1 and \mathbf{b}_2 . All the rotations are right-handed.

the corresponding Euler angles are:

$$\begin{cases} \phi = \arctan(J_{31} / J_{32}) \\ \theta = \arccos(J_{33}) \\ \psi = -\arctan(J_{13} / J_{23}) \end{cases} \quad (2-9)$$

It is necessary to note that the definition of Euler angles is not unique. In the literature many different conventions are used [Biedenharn and Louck, 1981]. These conventions depend on the axes about which the rotation sequence was made. The particular convention used here has a sequence of rotation about $\mathbf{a}_3 - \mathbf{a}_1 - \mathbf{a}_3$, which is also called 3-1-3 Euler angles sequence.

2-3 Homogeneous deformation

A rotation matrix only describes the orientation change. However both the orientation and magnitude of a vector may change during deformation. For example the Bain strain is a deformation of an FCC austenite structure into one that is body-centered cubic (BCC). An FCC structure can be represented by two different sets of bases: one defined with the FCC unit cell (denoted A) and the other using a body-centered tetragonal unit cell (BCT, denoted B), as shown in Figure 2-4 (a). The BCT to BCC transformation can be accomplished by a compression of $\eta_3 = (a_\alpha / a_\gamma)$ along $[0\ 0\ 1]_B$ coupled with an expansion of $\eta_1 = \eta_2 = (\sqrt{2}a_\alpha / a_\gamma)$ along $[1\ 0\ 0]_B$ and $[0\ 1\ 0]_B$, respectively, as shown in Figure 2-4 (b).

The deformation described can be written as a 3×3 deformation matrix (A S A), which is referred to the austenite basis, with the same basis symbol A on both sides of S. Thus the effect of the deformation changes a vector \mathbf{u} into a new vector \mathbf{u}' as shown in Figure 2-4 (b):

$$[\mathbf{A}; \mathbf{u}'] = (\mathbf{A} \mathbf{S} \mathbf{A}) [\mathbf{A}; \mathbf{u}] \quad (2-10)$$

where

$$(\mathbf{A} \mathbf{S} \mathbf{A}) = \begin{pmatrix} \eta_1 & 0 & 0 \\ 0 & \eta_2 & 0 \\ 0 & 0 & \eta_3 \end{pmatrix}$$

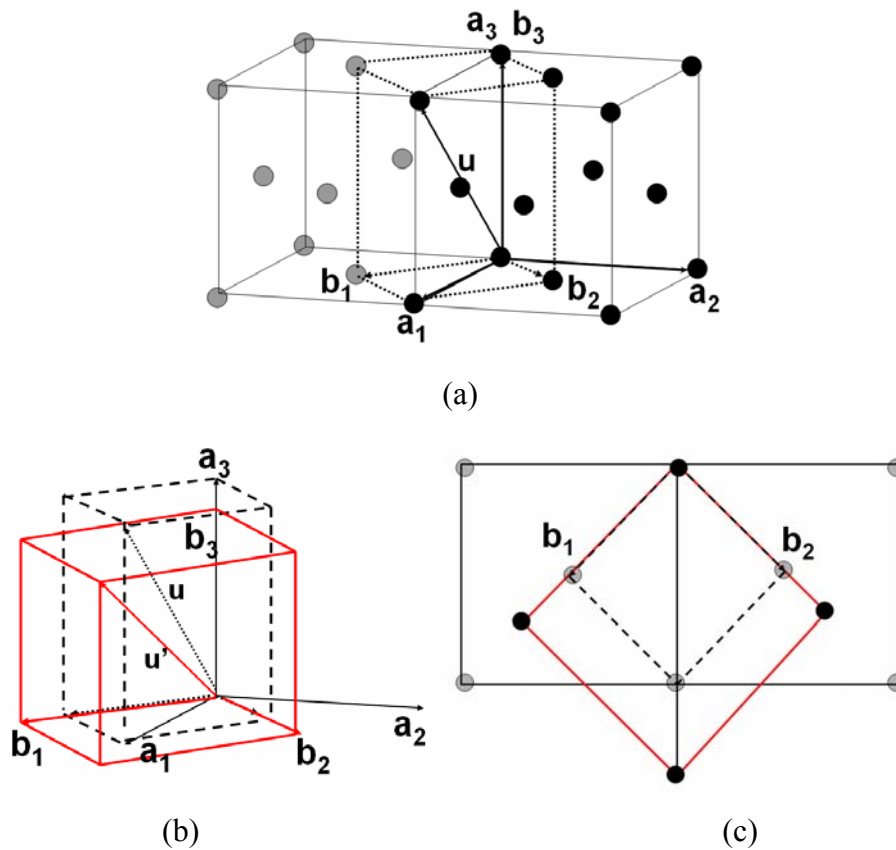


Fig. 2-4: (a) Austenite structure represented by a face-centered cubic (bold dark lines) or by a body-centered tetragonal cell (dashed lines). (b) A compression along $[0\ 0\ 1]_B$ coupled with an expansion along $[1\ 0\ 0]_B$ and $[0\ 1\ 0]_B$ is the Bain strain; (c) top view of Bain strain.

2-3-1 Similarity transformation

A change of coordinate system does not change the physical effect of the deformation. The deformation matrix $(A\ S\ A)$ can also be defined with respect to another coordinate system B, which satisfies:

$$[B; \mathbf{u}'] = (B\ S\ B) [B; \mathbf{u}]$$

If the coordinate transformation matrix relating A and B is $(A\ J\ B)$, then:

$$[A; \mathbf{u}] = (A\ J\ B) [B; \mathbf{u}] \text{ and } [B; \mathbf{u}'] = (B\ J\ A) [A; \mathbf{u}']$$

Substituting equation 2-10 into these equations we get,

$$[B; \mathbf{u}'] = (B\ J\ A) (A\ S\ A) (A\ J\ B) [B; \mathbf{u}]$$

hence

$$(B\ J\ B) = (B\ J\ A)(A\ S\ A)(A\ J\ B) \quad (2-11)$$

This is called a similarity transformation, which refers a deformation to a different basis.

2-3-2 Deformation matrix in mechanical twinning

The deformation which always leaves one plane of the parent crystal completely undistorted and unrotated is an invariant-plane strain (IPS). There are different types of invariant-plane strains as shown in Figure 2-5. Mechanical twinning, which only involves a simple shear and which is the topic of this thesis, is one of them, as shown in (b). Its deformation matrix can be represented as:

$$(Z P Z) = \begin{pmatrix} 1 & 0 & s \\ 0 & 1 & 0 \\ 0 & 0 & 1 \end{pmatrix}$$

where basis Z is specifically chosen to make each column of $(Z P Z)$ represents the components of a new vector generated by deformation of a vector equal to one of the basis vectors of Z .

The orientation relationship between crystallographic basis A and basis Z is

$$[A; \mathbf{d}] \parallel [Z; \mathbf{z}_1], \quad [A; \mathbf{q}] \parallel [Z; \mathbf{z}_2], \quad [A; \mathbf{p}] \parallel [Z; \mathbf{z}_3]$$

where \mathbf{d} is a unit vector parallel to the twinning direction, \mathbf{p} is a unit vector normal to twinning plane and $\mathbf{q} = \mathbf{p} \wedge \mathbf{d}$.

The rotation matrix between basis Z and basis A is hence derived as:

$$(A J Z) = \begin{pmatrix} d_1 & q_1 & p_1 \\ d_2 & q_2 & p_2 \\ d_3 & q_3 & p_3 \end{pmatrix}$$

where d_i, q_i, p_i ($i = 1, 2, 3$) are components of vector \mathbf{d} , \mathbf{q} and \mathbf{p} , respectively.

Using a similarity transformation this gives:

$$(A P A) = (Z J A)(A P A)(A J Z) = \begin{pmatrix} 1 + sd_1p_1 & sd_1p_2 & sd_1p_3 \\ sd_2p_1 & 1 + sd_2p_2 & sd_2p_3 \\ sd_3p_1 & sd_3p_2 & 1 + sd_3p_3 \end{pmatrix}$$

writing A^* as reciprocal of basis A , this equation simplifies as:

$$(A P A) = I + s [A; \mathbf{d}] (\mathbf{p}; A^*) \quad (2-12)$$

where s is the magnitude of twinning strain i.e. $1/\sqrt{2}$, and I is a 3×3 unit matrix.

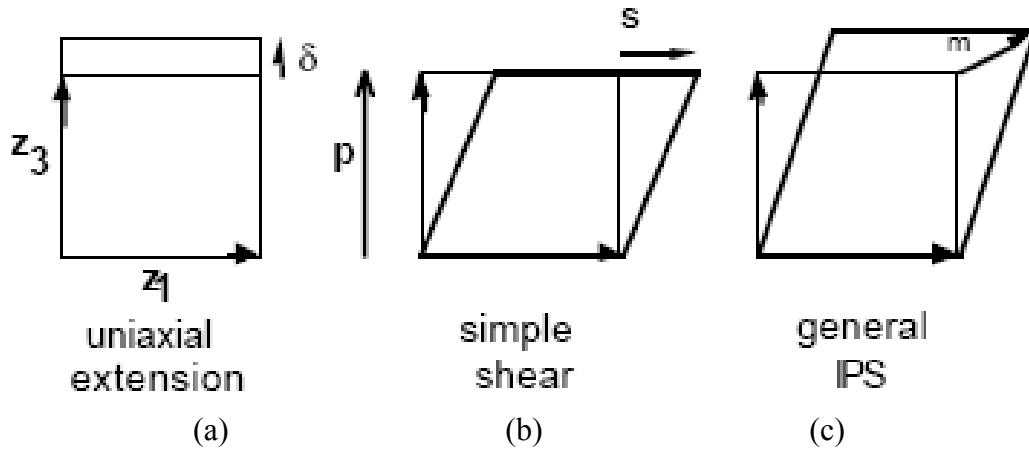


Fig. 2-5: Three different types of invariant plane strain (a) dilatation (b) simple shear (c) deformation in general. The basis Z is orthonormal. The squares represent the matrix before deformation. δ , s and m represent the magnitudes of dilatation, shear strain and general displacement, respectively. \mathbf{p} is a unit vector normal to the invariant plane parallel to the basis axis \mathbf{z}_3 , the shear strain s is parallel to \mathbf{z}_1 whereas the δ is parallel to \mathbf{z}_3 .

2-4 Texture representation

2-4-1 Pole figures

A pole figure is a two dimensional graphical representation of the distribution of crystal orientations relative to the polycrystalline sample reference frame. It is defined and constructed as follows:

Definition of a pole

Consider a crystal with a sphere around it (Figure 2-6 (a)). The crystal is located at the center of the sphere, designated as O . The orientation of plane P is given by its normal \mathbf{OP}' and its intersection with the sphere and the plane is a *great circle*; the intersection of the normal and the sphere is a *pole*. Clearly, at least two non-parallel poles are required to uniquely define an orientation.

Stereographic projection

Consider the xy plane, whose trace is the equator of the sphere (Figure 2-6 (b)). A line is connected joining the South Pole S (on the lower hemisphere) with the pole of interest P'. The intersection of SP' and the equatorial plane is the stereographic projection of pole P', denoted as P''.

Pole figure for texture

Consider a single crystal first. To draw a pole figure, choosing a particular form of crystal planes, $\{111\}$ for instance (Figure 2-6 (c)), plot the stereographic poles of all equivalent planes such as $(\bar{1}11)$, $(1\bar{1}1)$ and $(11\bar{1})$ relative to a reference frame. In the case of rolled metal, this latter frame may consist of the rolling direction (RD), transverse direction (TD) and normal direction (ND).

For polycrystalline samples, all $\{111\}$ poles for all grains are plotted.

Mathematics

Supposing the sphere has unit radius, then any pole P' can be represented by a unit vector with components $[u, v, w]$ in the sample reference. Using similar triangles, as shown in Figure 2-6 (d):

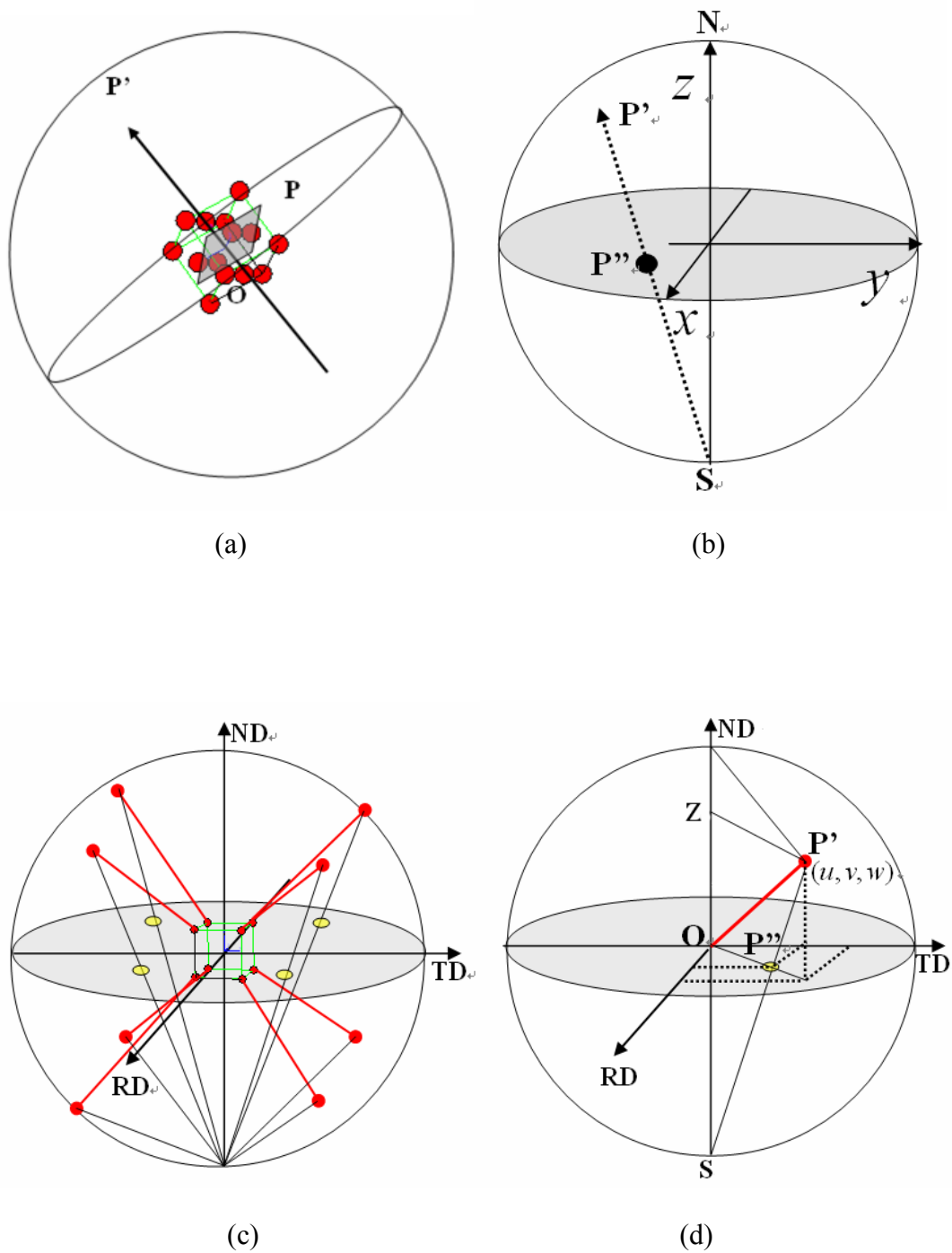
$$|OP''| = \frac{1}{1+w}$$

so, the coordinate of P'' on the equatorial plane is:

$$\begin{aligned}x &= \frac{u}{1+w} \\y &= \frac{v}{1+w}\end{aligned}\tag{2-13-1}$$

However, if OP' does not point to the northern hemisphere (i.e. $w < 0$), then the projection is from the North Pole with:

$$\begin{aligned}x &= \frac{u}{1-w} \\y &= \frac{v}{1-w}\end{aligned}\tag{2-13-2}$$



2-4-2 Orientation distribution function.

As discussed in Section 2.2, any crystal can be described using three independent Euler angles, (ϕ, θ, ψ) with respect to sample basis A. In materials science, as a convention these angles are generally written as $(\varphi_1, \Phi, \varphi_2)$, a set which constitutes “Euler space” in which the orientation of each grain is represented by a point. Figure 2-7 shows the orientation of 500 textured grains in Euler space.

However, three-dimensional graphs are not always easy to interpret, so intersections of Euler space are frequently plotted. In this method, the Euler space is divided into ‘slices’ at $\varphi_2 = 5^\circ$ intervals. Then these slices are arranged in a grid, putting all the dots in the interval to the nearest slice, and this is called an orientation distribution function as shown in Figure 2-8 (a). Figure 2-8 (b) gives the most common section, with $\varphi_2 = 45^\circ$.

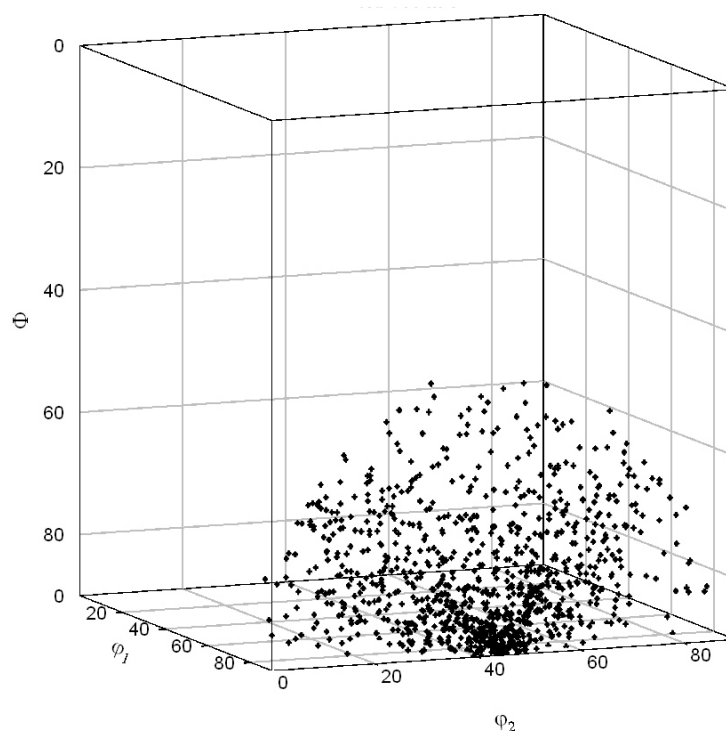
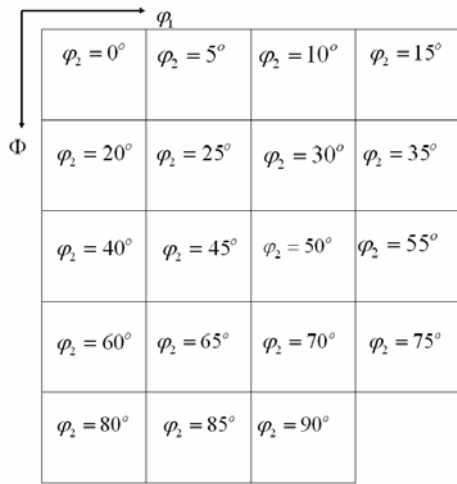
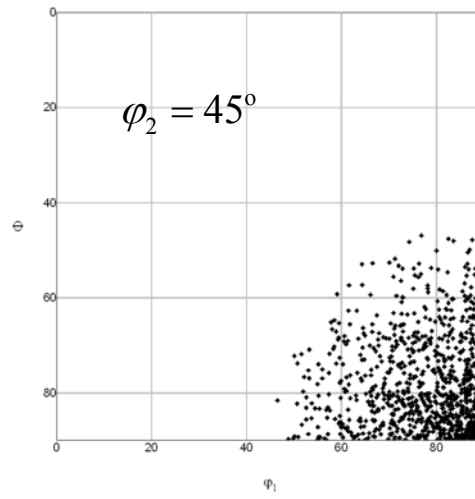


Fig. 2-7: Euler space of a textured material: each dot represents the orientation of one grain relative to a reference frame.



(a)



(b)

Fig. 2-8: (a) Orientation distribution function with $\varphi_2 = 5^\circ$ intervals. (b) $\varphi_2 = 45^\circ$ section of (a).

Chapter 3

Simulation of Twinning

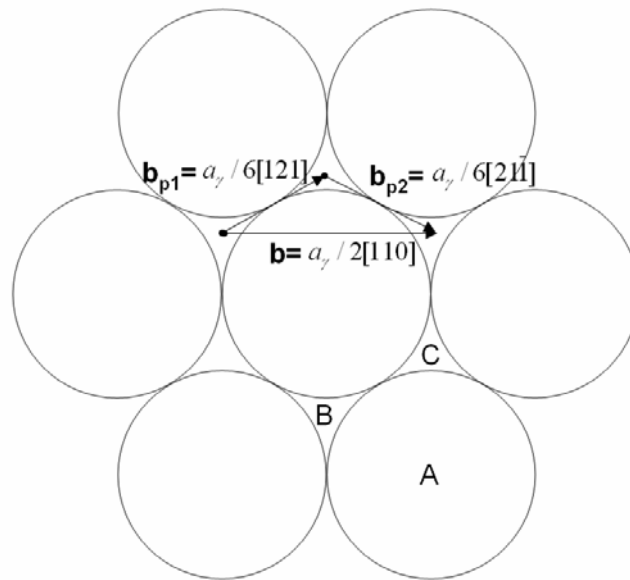
As an important plastic deformation mode deformation twinning happens in many materials, especially for those metals with body-centered cubic, hexagonal close packed and other lower symmetry structures, such as cobalt alloys [Mahajan and Chin, 1973]. A wider range of materials including FCC metals and alloys such as aluminum, copper [Asgari *et al.*, 1997; El-Danaf *et al.*, 1999; Chen *et al.*, 2003], silver-gold alloy [Suzuki and Barrett, 1958] and alumina-manganese alloy [Gray-III, 1988], intermetallic compounds [Christian and Laughlin, 1988], semiconductors [Pirouz, 1987]. A more comprehensive list of materials with mechanical twinning has been compiled by a number of authors [Gray-III, 1988; Christian and Mahajan, 1995]. In this work, only the FCC case is of interest.

3-1 Twinning in FCC

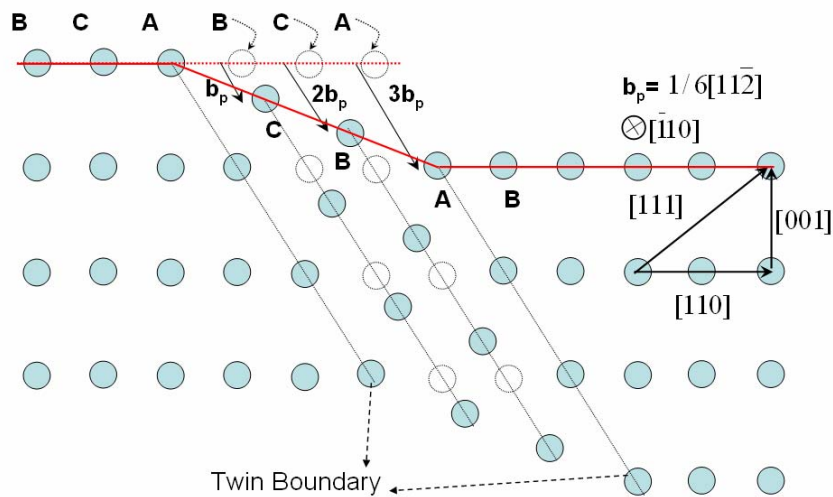
The close-packed plane in FCC is $\{111\}$ type plane with a stacking sequence of...ABCABC... [Callister, 2004]. Figure 3-1 (a) is a schematic representation of a $\{111\}$ plane in FCC where the Burger's vector \mathbf{b} of a lattice dislocation equal to $a_\gamma/2 \langle 110 \rangle$ is illustrated. The positions labeled A, B and C indicate three possible locations for the stacking of $\{111\}$ planes. The Burger's vector \mathbf{b} can dissociate into two partial Burger's vectors \mathbf{b}_{p1} and \mathbf{b}_{p2} along $\langle 112 \rangle$ directions, with dislocation reaction:

$$\frac{a_\gamma}{2}[110] \rightarrow \frac{a_\gamma}{6}[121] + \frac{a_\gamma}{6}[21\bar{1}]$$

This occurs because there is a reduction in energy since $|\mathbf{b}_{p1}|^2 + |\mathbf{b}_{p2}|^2 < |\mathbf{b}|^2$. The



(a)



(b)

Fig. 3-1: (a) Projection of a FCC $(\bar{1} 1 \bar{1})$ plane. A Burger's vector \mathbf{b} lies along $[110]$ and dissociates into two partial dislocations \mathbf{b}_{p1} along $[121]$ and \mathbf{b}_{p2} along $[2\bar{1}\bar{1}]$. (b) Schematic representation of the formation of twinning. FCC $[\bar{1}10]$ projection: $\{111\}$ layer B moving $\mathbf{b}_p = a_\gamma/6[1\bar{1}\bar{2}]$ to the new position C; C moving $2 \times a_\gamma/6[1\bar{1}\bar{2}]$ to B: a $a_\gamma/6[1\bar{1}\bar{2}]$ to A and then another $a_\gamma/6[1\bar{1}\bar{2}]$ to B; similarly A moving $3 \times a_\gamma/6[1\bar{1}\bar{2}]$ and still takes A position.

compounds of the two partial dislocations which are parallel to \mathbf{b} tend to repel each other, thus creating a stacking fault between them [Hull and Bacon, 2001]. However, the stacking fault energy per unit area exerts an attractive force between the partials which leads to an equilibrium separation between the partials at the point where the two forces balance.

Figure 3-1 (b) is a schematic representation of the formation of mechanical twinning: the sequential movement of close packed layers along $a_\gamma/6[1\bar{1}2]$ on (111) plane forms a twin plate.

It is obvious that movement along the opposite direction of \mathbf{b}_{p1} is unfavorable because the translation required would be $-2\mathbf{b}_{p1}$ which doubles the shear and hence is not favored from an energy point of view. The direct consequence of this fact is the polarization of twinning direction: on each {111} twinning plane, only three $\langle 112 \rangle$ directions out of six can be the twinning direction. Consequently there are 12 twinning systems in FCC, as listed in Table 4-1.

Table 4-1: The twinning systems in FCC materials. Due to the polarization of the twinning shear there are 12 possible twinning systems.

Twinning Plane	(1 1 1)	(1 $\bar{1}$ $\bar{1}$)	($\bar{1}$ 1 $\bar{1}$)	($\bar{1}$ $\bar{1}$ 1)
Twinning Directions	[1 1 $\bar{2}$]	[1 $\bar{1}$ 2]	[$\bar{1}$ 1 2]	[$\bar{1}$ $\bar{1}$ $\bar{2}$]
	[1 $\bar{2}$ 1]	[1 2 $\bar{1}$]	[$\bar{1}$ $\bar{2}$ $\bar{1}$]	[$\bar{1}$ 2 1]
	[$\bar{2}$ 1 1]	[$\bar{2}$ $\bar{1}$ $\bar{1}$]	[2 1 $\bar{1}$]	[2 $\bar{1}$ 1]

3-2 Twinning shear, deformation matrix and orientation relationship of twin

Mechanical twinning is a simple shear on the twinning plane which remains undistorted and unrotated. Consider a block of material illustrated in Figure 3-2,

which twins on plane K_1 . The plane denoted K_2 is undistorted but is rotated. In FCC, if K_1 plane is $(1\ 1\ 1)$ then K_2 is $(1\ 1\ \bar{1})$ plane.

The shear strain is defined as:

$$s = \frac{d}{h} = \frac{|a/6 \langle 112 \rangle|}{d_{111}} = \frac{a\sqrt{6}/6}{a/\sqrt{3}} = \frac{1}{\sqrt{2}}$$

where d_{111} is the interplanar spacing of the $(1\ 1\ 1)$ planes.

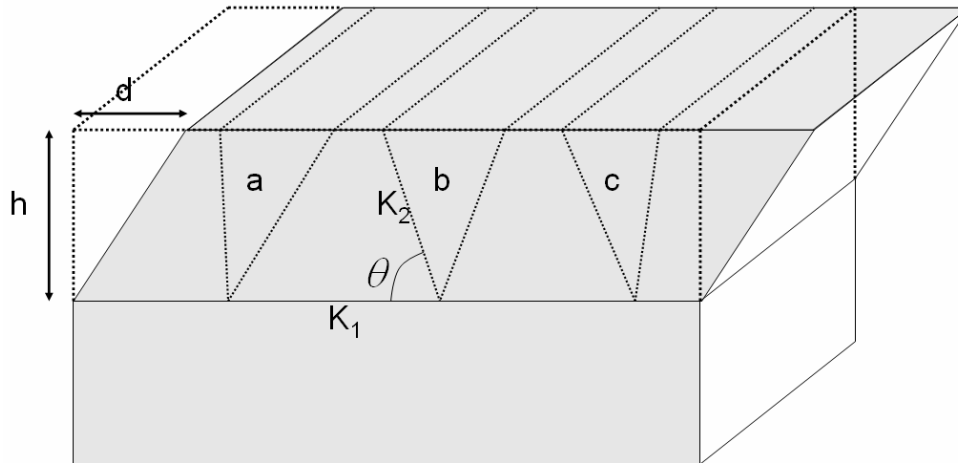


Fig. 3-2: Schematic representation of mechanical twinning of a block material. The interplanar distance for type a plane is lengthened, for c shortened and for b keeps the same

It is possible now to find the deformation matrix for every twinning system using equation 2-12, and the corresponding coordinate transformation matrix which describes the orientation relationship with matrix using the methods introduced in Chapter 2.

Table 3-2 Deformation matrices and coordinate transformation matrices for all 12 twinning systems in FCC.

Twinning system	deformation matrix (M P M)	coordinate transformation matrix (M J T)
$(1\ 1\ 1)[1\bar{1}\bar{2}]$	$\begin{pmatrix} 0.8333 & -0.1667 & 0.1667 \\ -0.1667 & 0.8333 & 0.1667 \\ 0.3333 & 0.3333 & 0.6667 \end{pmatrix}$	$\begin{pmatrix} 0.3333 & -0.6667 & -0.6667 \\ -0.6667 & 0.3333 & -0.6667 \\ -0.6667 & -0.6667 & 0.3333 \end{pmatrix}$

$$\begin{array}{l}
(1\ 1\ 1)[\bar{1}\bar{2}1] \quad \begin{pmatrix} 0.8333 & -0.1667 & 0.1667 \\ 0.3333 & 1.3333 & -0.3333 \\ -0.1667 & -0.1667 & 1.1667 \end{pmatrix} \quad \begin{pmatrix} 0.3333 & -0.6667 & -0.6667 \\ -0.6667 & 0.3333 & -0.6667 \\ -0.6667 & -0.6667 & 0.3333 \end{pmatrix} \\
(1\ 1\ 1)[\bar{2}11] \quad \begin{pmatrix} 1.3333 & 0.3333 & -0.3333 \\ -0.1667 & 0.8333 & 0.1667 \\ -0.1667 & -0.1667 & 1.1667 \end{pmatrix} \quad \begin{pmatrix} 0.3333 & -0.6667 & -0.6667 \\ -0.6667 & 0.3333 & -0.6667 \\ -0.6667 & -0.6667 & 0.3333 \end{pmatrix} \\
(1\ \bar{1}\ \bar{1})[1\ \bar{1}\ 2] \quad \begin{pmatrix} 0.8333 & -0.1667 & 0.1667 \\ 0.1667 & 1.1667 & -0.1667 \\ -0.3333 & -0.3333 & 1.3333 \end{pmatrix} \quad \begin{pmatrix} 0.3333 & 0.6667 & 0.6667 \\ 0.6667 & 0.3333 & -0.6667 \\ 0.6667 & -0.6667 & 0.3333 \end{pmatrix} \\
(1\ \bar{1}\ \bar{1})[1\ 2\ \bar{1}] \quad \begin{pmatrix} 0.8333 & -0.1667 & 0.1667 \\ -0.3333 & 0.6667 & 0.3333 \\ 0.1667 & 0.1667 & 0.8333 \end{pmatrix} \quad \begin{pmatrix} 0.3333 & 0.6667 & 0.6667 \\ 0.6667 & 0.3333 & -0.6667 \\ 0.6667 & -0.6667 & 0.3333 \end{pmatrix} \\
(1\ \bar{1}\ \bar{1})[\bar{2}\ \bar{1}\ \bar{1}] \quad \begin{pmatrix} 1.3333 & 0.3333 & -0.3333 \\ 0.1667 & 1.1667 & -0.1667 \\ 0.1667 & 0.1667 & 0.8333 \end{pmatrix} \quad \begin{pmatrix} 0.3333 & 0.6667 & 0.6667 \\ 0.6667 & 0.3333 & -0.6667 \\ 0.6667 & -0.6667 & 0.3333 \end{pmatrix} \\
(\bar{1}\ 1\ \bar{1})[\bar{1}\ 1\ 2] \quad \begin{pmatrix} 1.1667 & -0.1667 & 0.1667 \\ -0.1667 & 1.1667 & -0.1667 \\ -0.3333 & 0.3333 & 0.6667 \end{pmatrix} \quad \begin{pmatrix} 0.3333 & 0.6667 & -0.6667 \\ 0.6667 & 0.3333 & 0.6667 \\ -0.6667 & 0.6667 & 0.3333 \end{pmatrix} \\
(\bar{1}\ 1\ \bar{1})[\bar{1}\ \bar{2}\ \bar{1}] \quad \begin{pmatrix} 1.1667 & -0.1667 & 0.1667 \\ 0.3333 & 0.6667 & 0.3333 \\ 0.1667 & -0.1667 & 1.1667 \end{pmatrix} \quad \begin{pmatrix} 0.3333 & 0.6667 & -0.6667 \\ 0.6667 & 0.3333 & 0.6667 \\ -0.6667 & 0.6667 & 0.3333 \end{pmatrix} \\
(\bar{1}\ 1\ \bar{1})[2\ 1\ \bar{1}] \quad \begin{pmatrix} 0.6667 & 0.3333 & -0.3333 \\ -0.1667 & 1.1667 & -0.1667 \\ 0.1667 & -0.1667 & 1.1667 \end{pmatrix} \quad \begin{pmatrix} 0.3333 & 0.6667 & -0.6667 \\ 0.6667 & 0.3333 & 0.6667 \\ -0.6667 & 0.6667 & 0.3333 \end{pmatrix} \\
(\bar{1}\ \bar{1}\ 1)[\bar{1}\ \bar{1}\ \bar{2}] \quad \begin{pmatrix} 1.1667 & 0.1667 & -0.1667 \\ 0.1667 & 1.1667 & -0.1667 \\ 0.3333 & 0.3333 & 0.6667 \end{pmatrix} \quad \begin{pmatrix} 0.3333 & -0.6667 & 0.6667 \\ -0.6667 & 0.3333 & 0.6667 \\ 0.6667 & 0.6667 & 0.3333 \end{pmatrix} \\
(\bar{1}\ \bar{1}\ 1)[\bar{1}\ 2\ 1] \quad \begin{pmatrix} 1.1667 & 0.1667 & -0.1667 \\ -0.3333 & 0.6667 & 0.3333 \\ -0.1667 & -0.1667 & 1.1667 \end{pmatrix} \quad \begin{pmatrix} 0.3333 & -0.6667 & 0.6667 \\ -0.6667 & 0.3333 & 0.6667 \\ 0.6667 & 0.6667 & 0.3333 \end{pmatrix} \\
(\bar{1}\ \bar{1}\ 1)[2\ \bar{1}\ \bar{1}] \quad \begin{pmatrix} 0.6667 & -0.3333 & 0.3333 \\ 0.1667 & 1.1667 & -0.1667 \\ -0.1667 & -0.1667 & 1.1667 \end{pmatrix} \quad \begin{pmatrix} 0.3333 & -0.6667 & 0.6667 \\ -0.6667 & 0.3333 & 0.6667 \\ 0.6667 & 0.6667 & 0.3333 \end{pmatrix}
\end{array}$$

3-3 Criterion for the initiation of mechanical twinning

It is important to understand the factors for the initiation of mechanical twinning. An obvious hypothesis is that twin initiation occurs when the externally applied shear stress, across the twinning plane, resolved in the twinning direction, reaches a critical value, by analogy to Schmid's law for slip. But the results reported in the literature show that the scatter of measured twinning stress in a given material is generally too large and that the range of crystal orientations examined is too small to provide an adequate test of the above hypothesis [Christian and Mahajan, 1995]. However, many investigators believe that twinning is always accompanied (or preceded) by some microscopic slip on a very small scale that is difficult to investigate. Recently Karaman [2000] did the experiments and showed that multiple slip is required for twinning in the theoretically twinning orientations, and Szczerba [2004] claimed that a critical resolved shear stress (CRSS) for twinning in Cu-8 at.% Al single crystal exists, but for other materials the existence of CRSS is not proved yet. However, it is clearly necessary that, when twinning is caused by an external stress, the applied stress does work during the formation of twinning. Hence the criterion used for the initiation of the twinning and for the preference of twinning system in this project is the interaction energy, which is defined as the product of the resolved stress and the twinning shear.

The stress status of each point of the material (Figure 3-3 (a)) can be described by a 3×3 symmetric stress tensor in the basis A as:

$$(\mathbf{A} \mathbf{S} \mathbf{A}) = \begin{pmatrix} \sigma_{11} & \tau_{12} & \tau_{13} \\ \tau_{21} & \sigma_{22} & \tau_{23} \\ \tau_{31} & \tau_{32} & \sigma_{33} \end{pmatrix}$$

where σ_{11} , σ_{22} , σ_{33} are normal stresses and $\tau_{12} = \tau_{21}$, $\tau_{13} = \tau_{31}$, $\tau_{23} = \tau_{32}$ are shear stresses.

When the stress tensor is multiplied by a unit normal \mathbf{p} representing a plane (Figure 3-3 (b)), a traction vector \mathbf{t} representing the direction and magnitude of force per unit area on that plane is obtained by:

$$[\mathbf{A}; \mathbf{t}] = (\mathbf{A} \mathbf{S} \mathbf{A}) [\mathbf{A}; \mathbf{p}] \quad (3-1)$$

The traction \mathbf{t} is then resolved onto the twinning plane to obtain the maximum resolved shear stress, which in turn is resolved along the twinning direction \mathbf{d} . The interaction energy is therefore given by:

$$E = s \cdot \mathbf{t} \cdot (\mathbf{p}/|\mathbf{p}| \times (\mathbf{t}/|\mathbf{t}| \times \mathbf{p}/|\mathbf{p}|)) \cdot \mathbf{d}/|\mathbf{d}| \quad (3-2)$$

where s is a scalar $1/\sqrt{2}$.

Table 3-3 lists the preferential sequence of twinning systems according to this criterion, when a single crystal is tensile tested along [1 2 7].

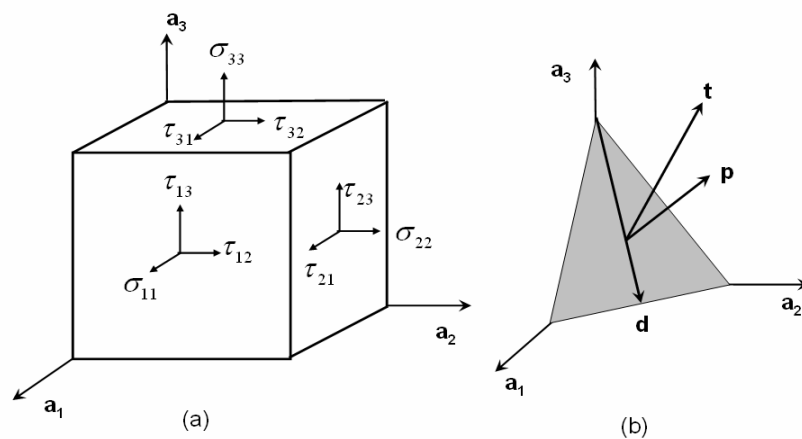


Fig. 3-3: (a) Stress status of a point: σ_{ii} ($i=1,2,3$) are principal stresses and τ_{ij} ($i, j=1,2,3; i \neq j$) are shear stresses, in equilibrium $\tau_{ij} = \tau_{ji}$. (b) The stress tensor applied to a surface gives a traction vector.

3-4 The calculation

FORTTRAN (formula translation) programs have been written in this work to implement the calculation of strain and crystallographic texture due to mechanical twinning in a polycrystalline FCC samples.

A sample reference frame is set identified by the basis symbol S . For convenience, one grain of austenite has its crystallographic axes aligned to the sample reference S . This particular grain is called the reference grain with basis symbol M_1 . Writing M_2 as the basis of another grain in the sample, its coordinate transformation matrix becomes $(M_1 \ J \ M_2)$ which is generated by the computer program. As discussed in Chapter 2, The method of *rotation axis and angle pair* is used to get a textured austenite while

Table 3-3: The preferential sequence of twinning system according to the interaction energy (E) criterion. Applied stress: uniaxial tension along $[1\ 2\ 7]$, 500 MPa.

Twinning system index	operating twinning system	$E / \text{J mole}^{-1}$
1	$(1\ \bar{1}\ \bar{1})[\bar{2}\ \bar{1}\ \bar{1}]$	192.05
2	$(\bar{1}\ 1\ \bar{1})[\bar{1}\ \bar{2}\ \bar{1}]$	157.13
3	$(1\ 1\ 1)[\bar{2}\ 1\ 1]$	152.77
4	$(1\ 1\ 1)[1\ \bar{2}\ 1]$	87.30
5	$(\bar{1}\ \bar{1}\ 1)[\bar{1}\ 2\ 1]$	87.30
6	$(\bar{1}\ \bar{1}\ 1)[2\ \bar{1}\ 1]$	61.10
7	$(\bar{1}\ 1\ \bar{1})[2\ 1\ \bar{1}]$	39.28
8	$(1\ \bar{1}\ \bar{1})[1\ 2\ \bar{1}]$	34.91
9	$(\bar{1}\ \bar{1}\ 1)[\bar{1}\ \bar{1}\ \bar{2}]$	-148.40
10	$(\bar{1}\ 1\ \bar{1})[\bar{1}\ 1\ 2]$	-196.42
11	$(1\ \bar{1}\ \bar{1})[1\ \bar{1}\ 2]$	-226.97
12	$(1\ 1\ 1)[1\ 1\ \bar{2}]$	-240.07

the method of *Euler angles* is capable of generating a randomly distributed matrix.

When generating texture, for example 1000 grains with Goss texture, the reference grain is set in the ideal Goss orientation, that is:

$$\mathbf{RD} ([1\ 0\ 0]_s) \parallel [0\ 0\ 1], \quad \mathbf{ND} ([0\ 1\ 0]_s) \parallel [1\ 1\ 0]$$

$$\text{and } \mathbf{TD} ([0\ 0\ 1]_s) \parallel [0\ 0\ 1] \wedge [1\ 1\ 0].$$

The remaining 999 grains are generated by choosing rotation axes randomly, but limiting the maximum value of the right-handed rotation angle θ .

However when generating a matrix with a fibre texture which has a specific direction pointing along one of the sample reference frame axes, then instead of setting a reference grain, an ideal direction is needed as a reference. Taking α -fibre as an example:

$$\mathbf{ND} ([0\ 1\ 0]_S) \parallel [1\ 1\ 0]$$

By generating any two random numbers a_1 and a_2 ranging from -1 to 1, the \mathbf{RD} and \mathbf{TD} are given as: $\mathbf{RD} \parallel [a_1\ -a_1\ a_2]$ and $\mathbf{TD} \parallel [1\ 1\ 0] \wedge [a_1\ -a_1\ a_2]$.

3-4-1 The calculation of strain

Single crystal

Figures 3-4 (a) and (b) show the deformation of a single grain. According to the published work, at least two twinning systems operate in a given austenite grain when the material is severely deformed [Karaman et al., 2000; Allain et al., 2004a]. Supposing that two twinning systems with the largest two values of interaction energies operate, one denoted as \mathbf{I} with volume percent $V_1\%$ and the other denoted as \mathbf{II} with volume percent $V_2\%$. A vector \mathbf{OP} changes to a new one \mathbf{OP}_1 as a result of the twinning shear. The true strain is consequently given by

$$\varepsilon = \ln (|\mathbf{OP}_1|/|\mathbf{OP}|) \quad (3-3)$$

Dividing vector \mathbf{OP} into five sections, \mathbf{OA} , \mathbf{BC} , \mathbf{DP} remain in the untwinned region and keep constant before and after deformation whereas \mathbf{AB} and \mathbf{CD} in the twinned regions change into \mathbf{AB}_1 and $\mathbf{C}_1\mathbf{D}_1$ after twinning shear, as shown in Figure 3-4 (b). The new vector is therefore the net vector of \mathbf{OA} , \mathbf{AB}_1 , $\mathbf{B}_1\mathbf{C}_1$, $\mathbf{C}_1\mathbf{D}_1$, and \mathbf{DP}_1 ,

$$[\mathbf{M}; \mathbf{OP}_1] = [\mathbf{M}; \mathbf{OA}] + [\mathbf{M}; \mathbf{AB}_1] + [\mathbf{M}; \mathbf{B}_1\mathbf{C}_1] + [\mathbf{M}; \mathbf{C}_1\mathbf{D}_1] + [\mathbf{M}; \mathbf{DP}_1] \quad (3-4)$$

the magnitudes of \mathbf{AB}_1 and $\mathbf{C}_1\mathbf{D}_1$ should be proportional to their volume percents, $V_1\%$ and $V_2\%$, respectively. Denoting the deformation matrix $(\mathbf{M} \mathbf{P}_{T_1} \mathbf{M})$ for twin \mathbf{I} and $(\mathbf{M} \mathbf{P}_{T_2} \mathbf{M})$ for twin \mathbf{II} , then

$$[\mathbf{M}; \mathbf{AB}_1] = (\mathbf{M} \mathbf{P}_{T_1} \mathbf{M}) \times [\mathbf{M}; \mathbf{AB}] = (\mathbf{M} \mathbf{P}_{T_1} \mathbf{M}) \times [\mathbf{M}; \mathbf{OP}] \times V_1\% \quad (3-5)$$

$$[\mathbf{M}; \mathbf{C}_1\mathbf{D}_1] = (\mathbf{M} \mathbf{P}_{T_2} \mathbf{M}) \times [\mathbf{M}; \mathbf{CD}] = (\mathbf{M} \mathbf{P}_{T_2} \mathbf{M}) \times [\mathbf{M}; \mathbf{OP}] \times V_2\% \quad (3-6)$$

$$[\mathbf{M}; \mathbf{OA}] + [\mathbf{M}; \mathbf{C}_1\mathbf{D}_1] + [\mathbf{M}; \mathbf{DP}_1] = (1 - V_1\% - V_2\%) \times [\mathbf{M}; \mathbf{OP}] \quad (3-7)$$

Substituting equation 3-5, 3-6, 3-7 into equation 3-4 gives the new distorted and rotated vector \mathbf{OP}_1 .

Bicrystal

Figure 3-4 (c) shows a bicrystal before deformation. Denoting the basis of grain 1 as M_1 , and grain 2 as M_2 , the coordinate transformation matrix is then $[M_1 \ J \ M_2]$. The distorted and rotated vector $\mathbf{P}_1\mathbf{P}_2$ in grain 2 can be found by following the same procedure as used in the calculation for the single crystal. The components of the net vector \mathbf{OP}_2 with respect to the basis M_1 are given by the equation

$$[M_1; \mathbf{OP}_2] = [M_1; \mathbf{OP}_1] + (M_1 \ J \ M_2) \times [M_2; \mathbf{P}_1\mathbf{P}_2] \quad (3-8)$$

hence the true strain is

$$\varepsilon = \ln (|\mathbf{OP}_2| / |\mathbf{OP}'|) \quad (3-9)$$

If \mathbf{OP}_1 and $\mathbf{O}'\mathbf{P}'$ are normalized, 3-9 can be written as

$$\varepsilon = \ln (|\mathbf{OP}_2| / 2) \quad (3-10)$$

Polycrystalline

The calculation for polycrystalline is simply a repetition of the calculation of bicrystal. For a sample with n grains,

$$\varepsilon_n = \ln (|\mathbf{OP}_n| / n) \quad (3-11)$$

3-4-2 The calculation of texture

Still referring to Figure 3-4 (b), writing T_{11} as the basis of twin **I** in the reference grain 1 then the coordinate transformation matrix between it and its parent is $(M_1 J T_{11})$. Any direction \mathbf{u} in parent and in twin **I** can be represented in the sample reference using equation 2-1 in Chapter 2.

$$[S; \mathbf{u}] = (S J M_1) [M_1; \mathbf{u}] \quad (3-12)$$

and

$$[S; \mathbf{u}] = (S J M_1) (M_1 J T_{11}) [T_{11}; \mathbf{u}] = (S J T_{11}) [T_{11}; \mathbf{u}] \quad (3-13)$$

Similarly for grain 2

$$[S; \mathbf{u}] = (S J M_1) (M_1 J M_2) [M_2; \mathbf{u}] = (S J M_2) [M_2; \mathbf{u}] \quad (3-14)$$

and

$$[S; \mathbf{u}] = (S J M_1) (M_1 J M_2) (M_2 J T_{21}) [T_{21}; \mathbf{u}] = (S J T_{21}) [T_{21}; \mathbf{u}] \quad (3-15)$$

When $[S; \mathbf{u}]$ is projected on the equatorial plane of a stereographic sphere using equation 2-13, then one gets the pole figure; whereas when $(S J M_i)$, $(S J T_{ij})$ ($i=1$, number of grains; $j=1,2$) are compared with the Euler angles representation of coordinate transformation matrix in equation 2-7, one gets the Euler angles of all the grains and their twins by equation 2-9.

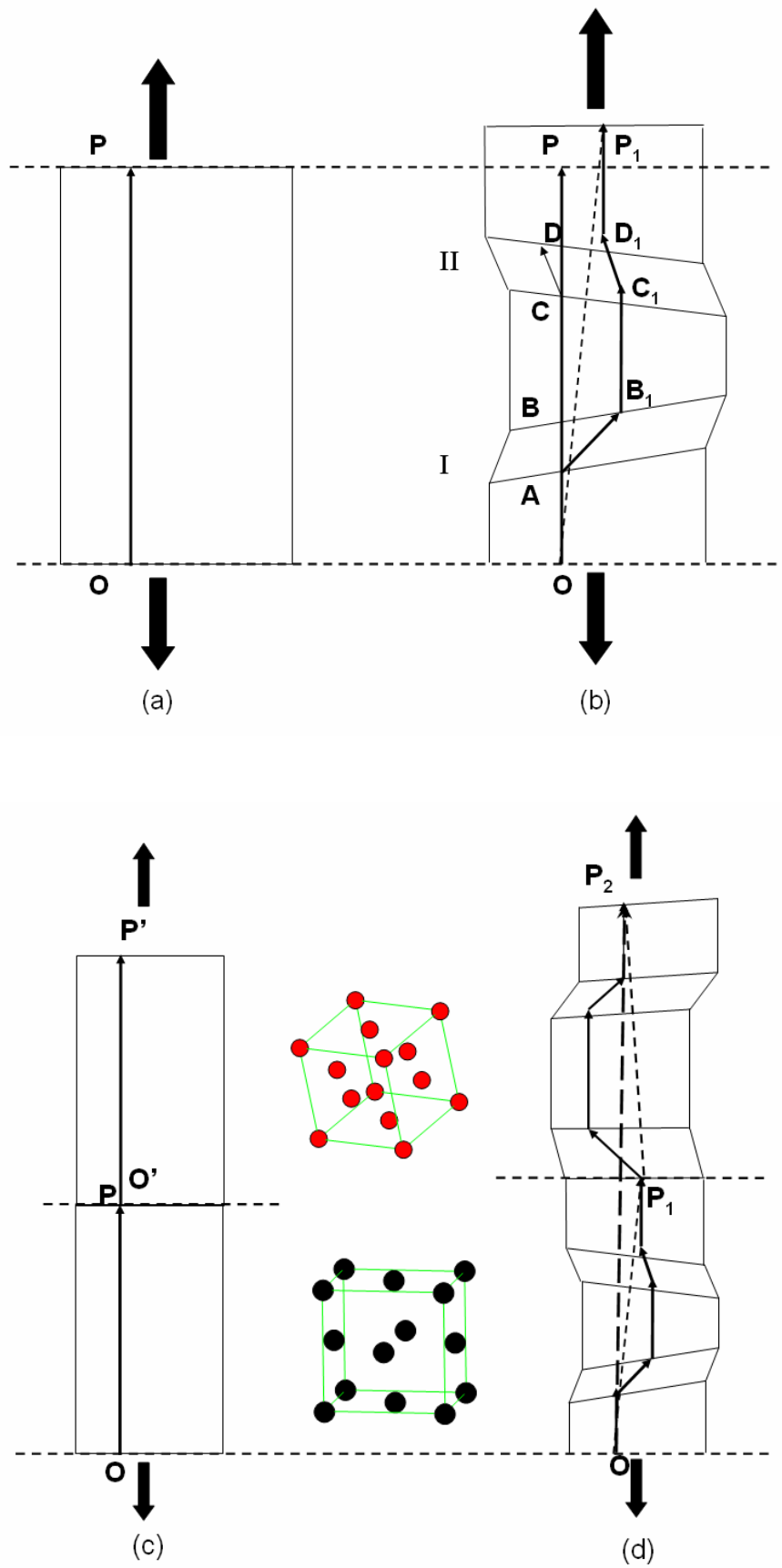


Fig. 4-2 Schematic representation of the deformation of single crystal (a-b) and bicrystal (c-d)

Chapter 4

Results and Discussions

A model has been developed to calculate the strain due to twinning and to simulate the resulting changes in crystallographic texture of TWIP steel. FORTRAN programs were written to implement the calculations. Some results obtained are compared against data in the published literature.

4-1 Texture

4-1-1 Modeling of important orientations in FCC orientations

Crystal orientations in sheets are specified by the Miller indices of the crystal plane which is parallel to the plane of the sheet, and the indices of the crystal direction which in that plane is parallel to the rolling direction, in a form of $\{hkl\} \langle uvw \rangle$.

FCC metals have several important crystal orientations which should be considered when analyzing the evolution of textures. They are all listed in Table 4-1-1. Most of these orientations are located on $\varphi_2 = 45^\circ$ section of the orientation distribution function (ODF), as shown in Figure 4-1-1. Each particular orientation is represented by a two dimensional projection of the FCC unit cell, each plane of which represents a $\{100\}$ plane. The projections are in the normal direction (ND); the tensile direction or rolling direction (TeD or RD) is vertical pointing upwards while the transversal direction (TD) is horizontal pointing to the right.

All the crystal orientations with a $\langle 110 \rangle$ direction parallel to the normal direction, such as Goss orientation $\{110\} \langle 001 \rangle$ and Brass orientation $\{110\} \langle 112 \rangle$, form a fibre which is called α – fibre. The brass orientation is of great importance on this

Table 4-1-1: Important crystallographic orientations of textured pure FCC metals and alloys, their orientation, presence on fibres and Euler angles at $\varphi_2 = 45^\circ$ except for the S-orientation where $\varphi_2 = 63^\circ$ [Vercammen *et al.*, 2004a].

Name	Orientation	Fibre	Euler angles: $g = [\varphi_1 \phi 45]$
C, cube	$\{001\}\langle 100\rangle$	–	[45 0 45]
G, Goss	$\{110\}\langle 001\rangle$	$\alpha\tau$	[90 90 45]
B, brass	$\{110\}\langle 112\rangle$	$\alpha\beta$	[55 90 45]
RG, rot. Goss	$\{110\}\langle 110\rangle$	α	[0 90 45]
E	$\{111\}\langle 110\rangle$	γ	[0 55 45] [60 55 45]
F	$\{111\}\langle 112\rangle$	γ	[30 55 45] [90 55 45]
Cu, copper	$\{112\}\langle 111\rangle$	$\beta\tau$	[90 35 45]
CuT, copper twins	$\{552\}\langle 115\rangle$	τ	[90 74 45]
S	$\{123\}\langle 634\rangle$	β	[59 37 63]

α -fibre: $\langle 110\rangle$ parallel to ND
 β -fibre: $\langle 110\rangle$ tilted 60° from ND towards RD
 γ -fibre: $\langle 111\rangle$ parallel to ND
 τ -fibre: $\langle 110\rangle$ parallel to TD.

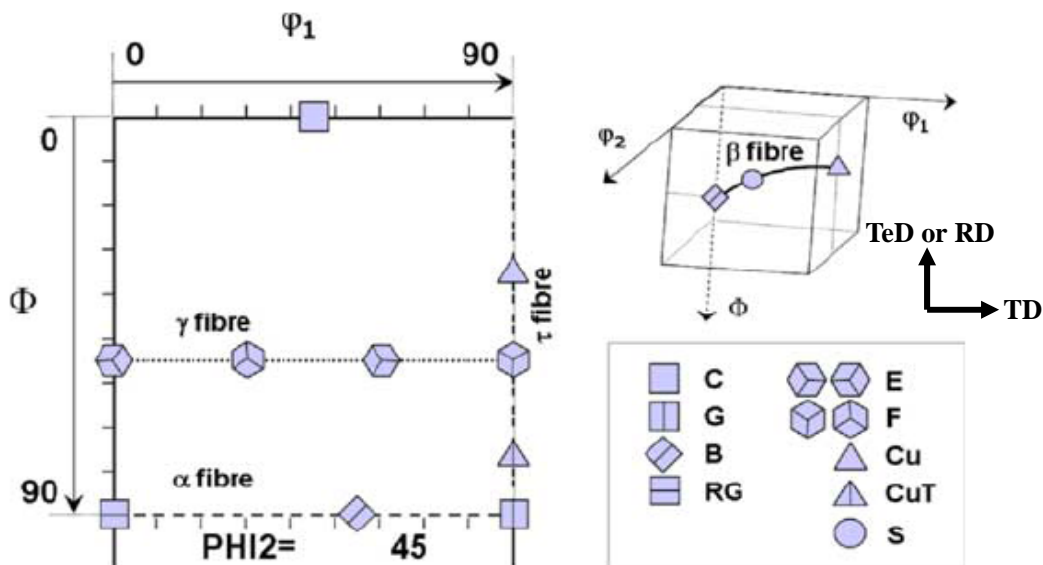


Figure 4-1-1: Schematic representation of the $\varphi_2 = 45^\circ$ section of the ODF of FCC metals. Each particular orientation is represented by a two dimensional projection of FCC structure along the normal direction. The tensile direction is vertical pointing upwards and the transversal direction is horizontal pointing to the right.

fibre especially during cold rolling of low stacking fault energy FCC materials such as brass. A second important fibre on this section is the τ -fibre which contains all crystal orientations with a $\langle 110 \rangle$ direction parallel to the transverse direction, such as the Copper $\{112\} \langle 111 \rangle$ and Goss orientations. The Copper orientation is important for high stacking fault energy FCC materials such as aluminum and pure copper [Hirsch *et al.*, 1988]. Also important fibre is the γ -fibre for grains with $\{111\}$ planes parallel to the normal direction; this fibre indicates that the slip or twinning planes orient parallel to the rolling plane during the deformation of flat samples.

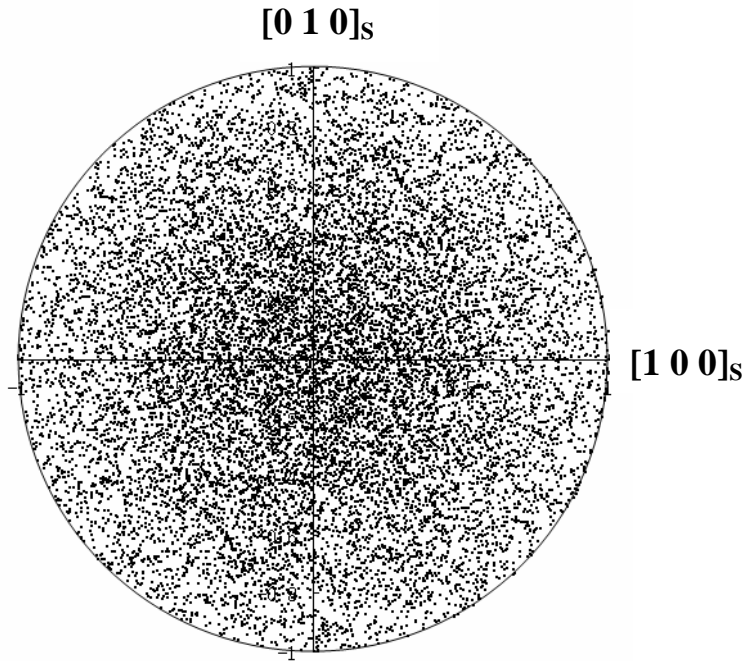
These important orientations are generated by the program.

Figure 4-1-2 (a) shows the calculated 100 pole figures for 2000 grains with a random orientation distribution. Due to the intrinsic angular distortion of stereographic projections, the intensity slightly increases towards the centre of the stereogram.

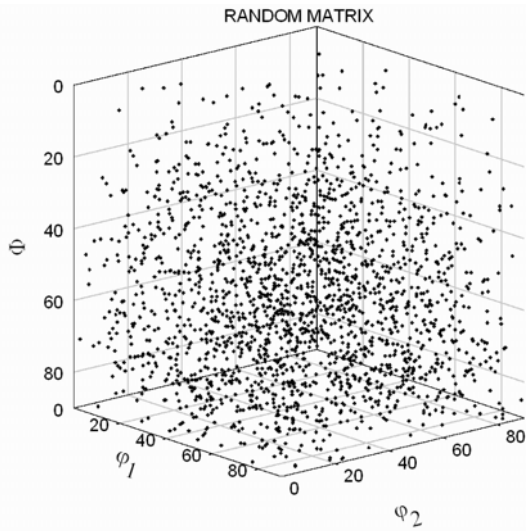
Figure 4-1-2 (b) is the corresponding Euler space representation and Figure 4-1-2 (c) the φ_2 projection.

It is evident from (c) that a random orientation distribution in three-dimensional space is not uniform in Euler space [Bunge, 1982].

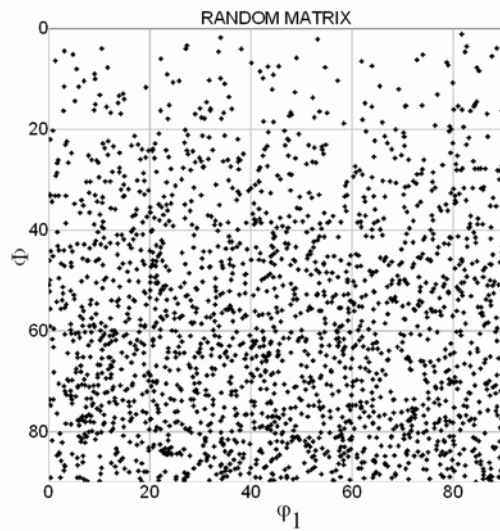
Figures 4-1-3 to 4-1-6 give the computer generated Cube, Goss, Brass, Copper textured austenite matrix respectively, where the term “matrix” refers to the austenite prior to deformation. As indicated previously, the intensity distribution is determined by the rotation angle range. In all these cases, the rotation angle is limited to the range from 0 to 45° . Figure 4-1-7 gives the computer generated α -fibre and γ -fibre in Euler space, the maximum rotation angle θ in these cases being 25° .



(a)



(b)



(c)

Fig. 4-1-2: (a) Model generated 100-pole figure for 2000 randomly oriented austenite grains. (b) Euler space representation and (c) ϕ_2 projection of (b). It is clear from (c) that a random distribution in three-dimensional space does not appear random in Euler space.

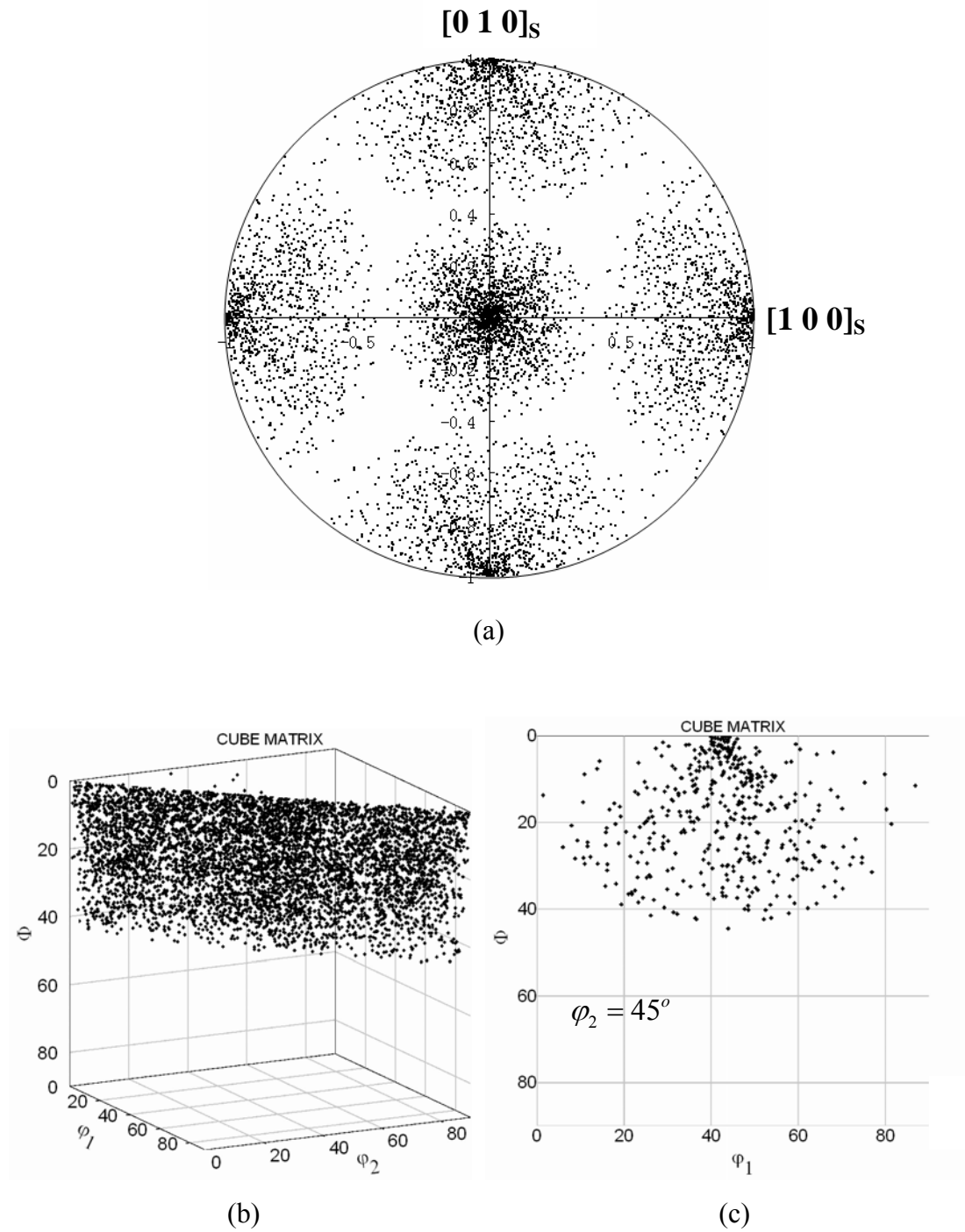


Fig. 4-1-3: (a) Model generated 100-pole figure for 2000 Cube-textured austenite grains. (b) Euler space representation for 6000 Cube-textured austenite grains and (c) $\phi_2 = 45^\circ$ section of (b). Maximum rotation angle $\theta = 45^\circ$.

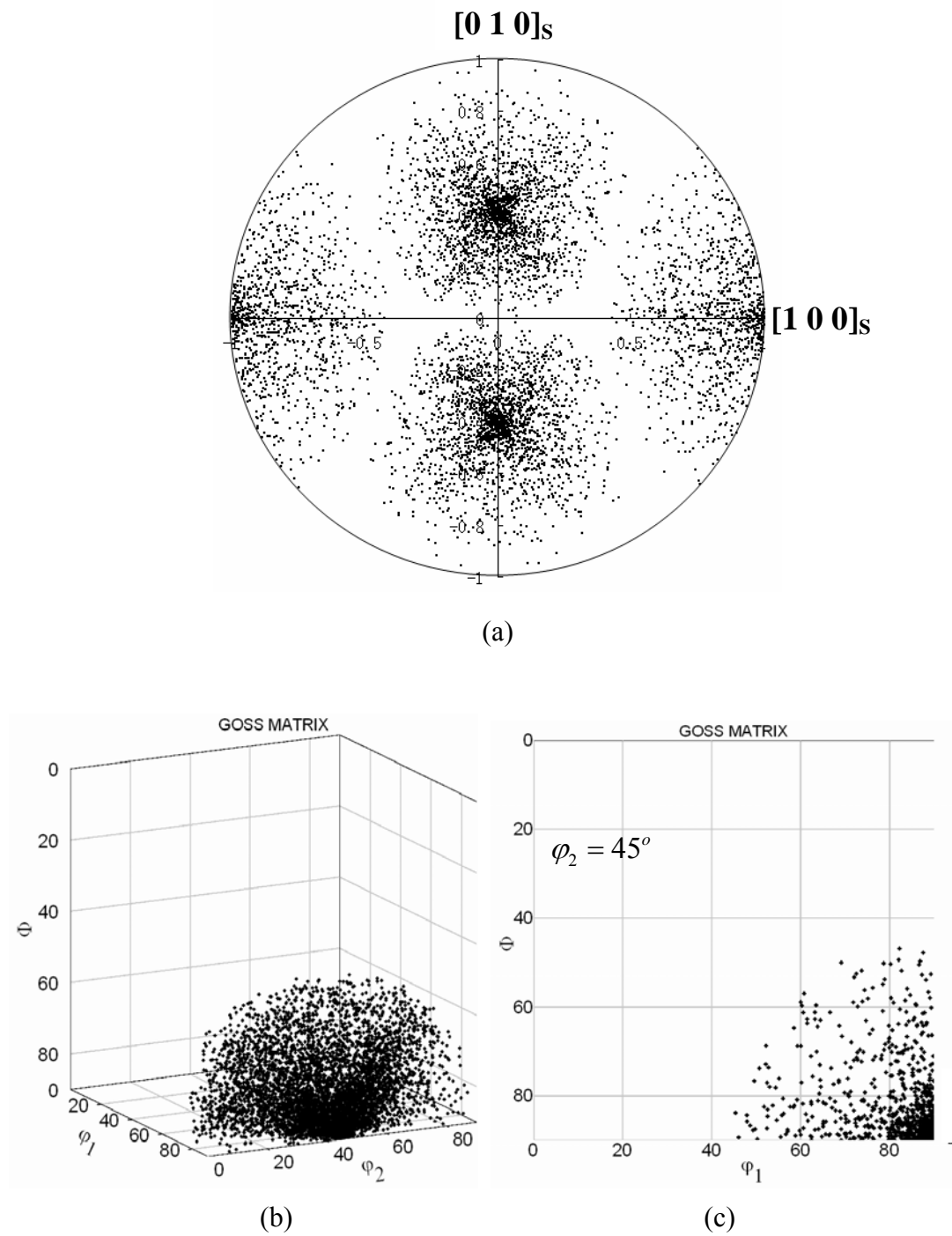


Fig. 4-1-4: (a) Model generated 100-pole figure for 2000 Goss-textured austenite grains. (b) Euler space representation for 6000 Goss-textured austenite grains and (c) $\varphi_2 = 45^\circ$ section of (b). Maximum rotation angle $\theta = 45^\circ$.

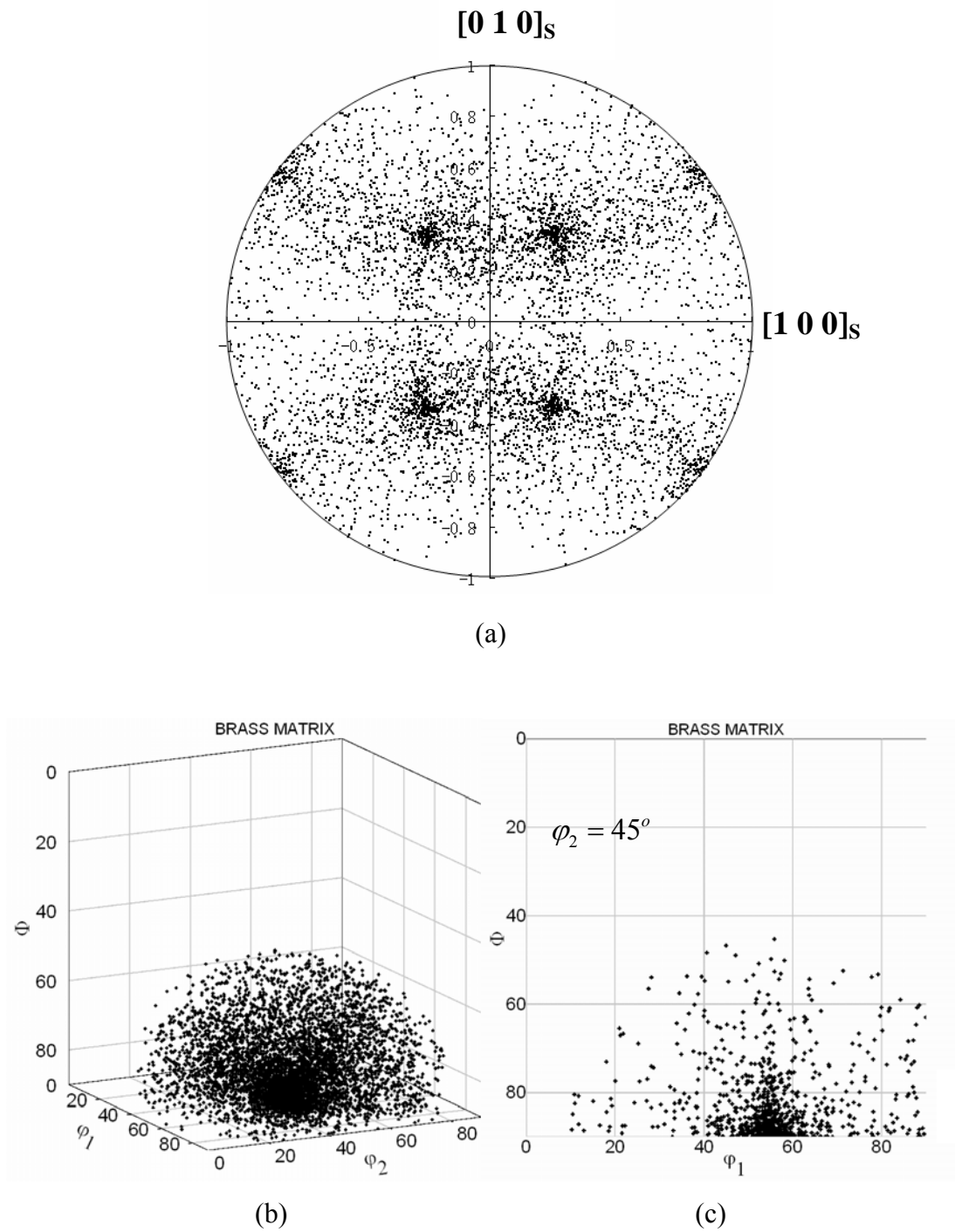


Fig. 4-1-5: (a) Model generated 100-pole figure for 2000 Brass-textured austenite grains. (b) Euler space representation for 6000 Brass-textured austenite grains and (c) $\phi_2 = 45^\circ$ section of (b). Maximum rotation angle $\theta = 45^\circ$.

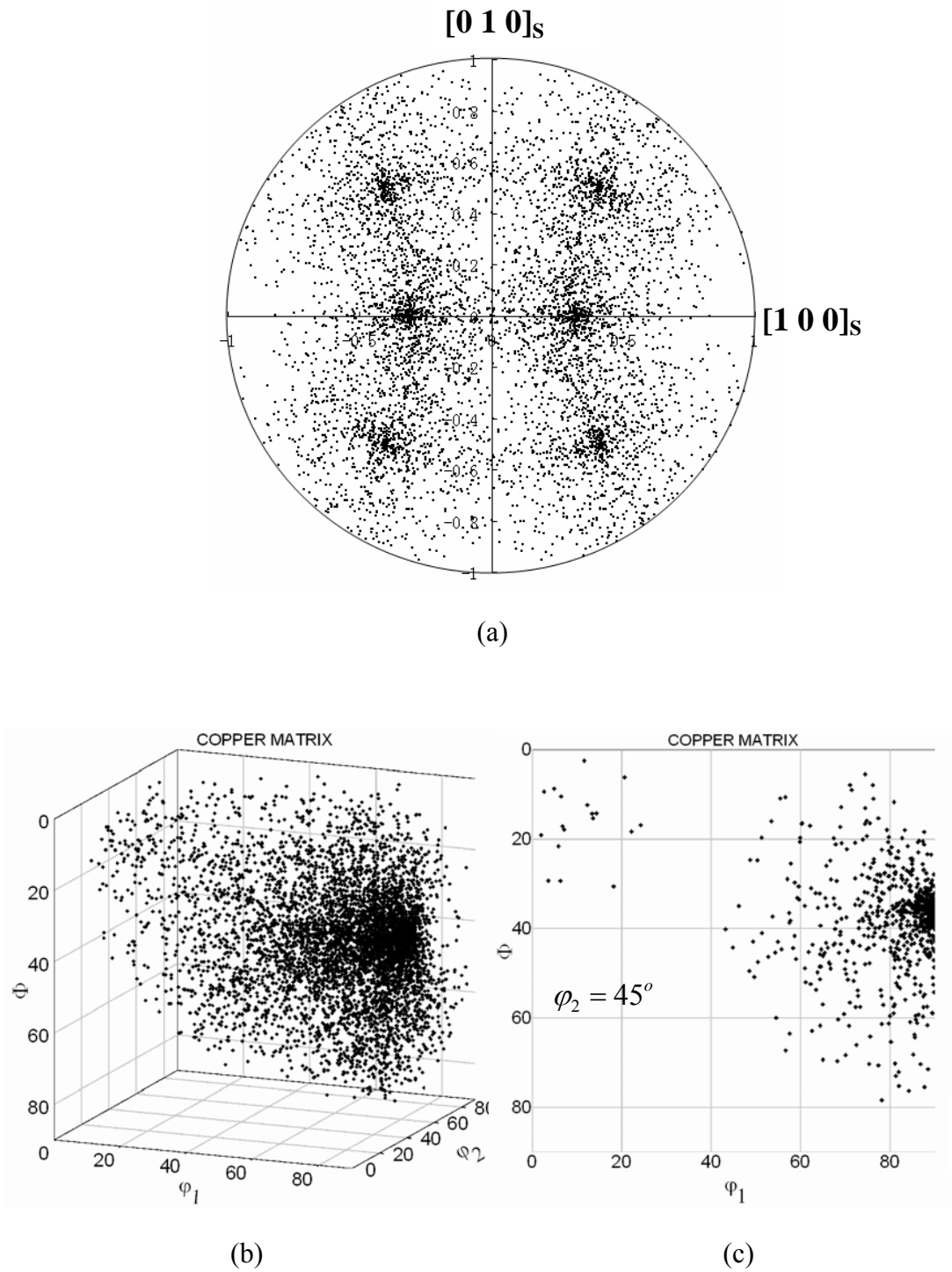
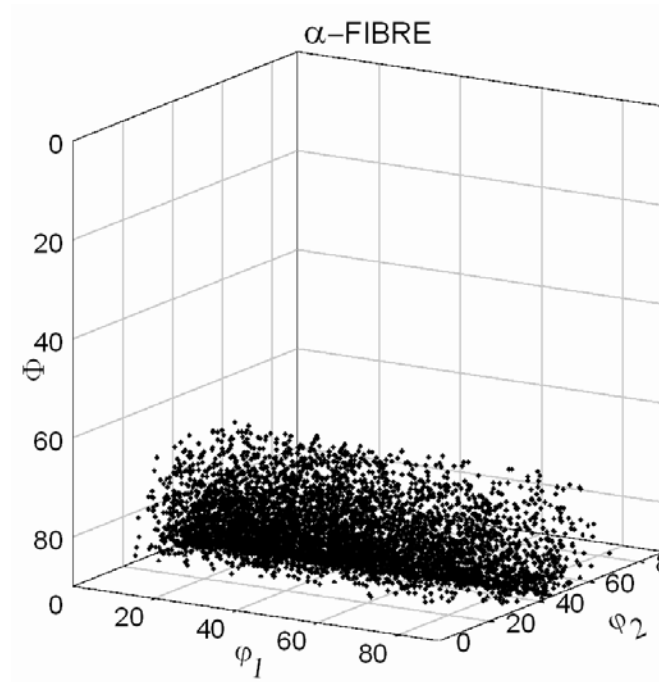
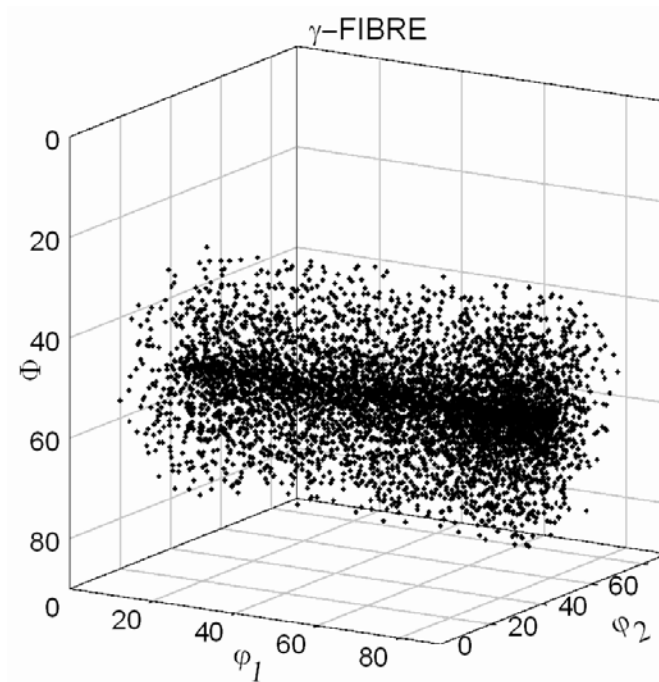


Fig. 4-1-6: (a) Model generated 100-pole figure for 2000 Copper-textured austenite grains. (b) Euler space representation for 6000 Copper-textured austenite grains and (c) $\phi_2 = 45^\circ$ section of (b). Maximum rotation angle $\theta = 45^\circ$.



(a)



(b)

Fig. 4-1-7: Euler space representation of model generated 6000 austenite grains with α – fibre (a) and (b) γ – fibre. Maximum rotation angle $\theta = 25^\circ$.

4-1-2 Twinning effect on textures

In this section, a calculation was done to check how the stress state affects the development of texture.

A tensile test was computed on a piece of Cube textured austenite containing 2000 grain with rotation angle ranging from $0 \sim 45^\circ$ and with a stress tensor in the sample basis S given as

$$(\mathbf{S} \boldsymbol{\sigma} \mathbf{S}) = \boldsymbol{\sigma} \begin{pmatrix} 1 & 0 & 0 \\ 0 & 0 & 0 \\ 0 & 0 & 0 \end{pmatrix}$$

The variant activation criterion had been introduced in Chapter 3. The 100-pole figure and the $\varphi_2 = 45^\circ$ ODF of this parent austenite matrix are in Figure 4-1-3. Figures 4-1-8 and 4-1-9 represent how mechanical twinning under this stress state changes the original Cube texture.

The most favored twinning system in each grain is denoted twin 1, and the second most favored twin 2, and so on. Figure 4-1-8 (1) is the 100-pole figure of the whole piece assuming that every grain was 100% twinned by twin 1; part (2) was assumed to be twinned by twin 2 alone, and so on.

Figure 4-1-9 (1-a) shows the outcome assumed that twin 1 and twin 2 operated in every grain, in equal proportion; in (1-b) assumed that only 66% parent of austenite undergoes twinning so the pole figure remains the 100-poles of parent matrix, whose position circled red. Similarly, (2-a), (2-b) assumed twins 1, 2 and 3 operate and (3-a) (3-b) assumed that the 4 most favored twinning systems operate.

It is interesting to note that the least favored twinning system in tension (twin 12) should be the most favorable system in compression. It is evident that twin 1 and twin 12 are different. However, the difference decreases as the number of operating twinning systems increases.

Figures 4-1-9 (4-a) ~ (6-b) show the superposition for twinning systems 9 ~ 12 and matrix. Compared with Figures 4-1-9 (1-a) ~ (3-b), as number of operating twinning systems increases, the difference in pole figures between tension and compression decreases. This fact may indicate that when the strain is very high so that

two or three twinning systems operate in each grain, twinning effects on texture change may be the same for both tension and compression.

The $\varphi_2 = 45^\circ$ of twin 1 to twin 6, together with their superimpositions, were also calculated and are listed in Figure 4-1-10.

It is evident that twinning due to tensile stress changes the original texture dramatically. However, when the same calculation was performed on Brass and Copper textured austenite, there are some twinning systems which do not change the original orientation much (Appendix A). This is because the orientation of some of the twinned parent is the same as that of another part of parent, but at the moment it has not been explained why this only happens on Brass and Copper textures. This will in future work be investigated by taking the exact Brass / Copper orientation, applying twinning operating and seeing whether there is a superposition of twin and matrix poles.

To check the different effects of the different stress states to the twinning texture, a calculation of the orientation changes of a Cube textured austenite under biaxial

tension, $(S \sigma S) = \sigma \begin{pmatrix} 1 & 0 & 0 \\ 0 & 1 & 0 \\ 0 & 0 & 0 \end{pmatrix}$, was also conducted. The pole figures of individual

twinning systems are listed in Figure 4-1-11. The difference with the uniaxial tensile test is evident.

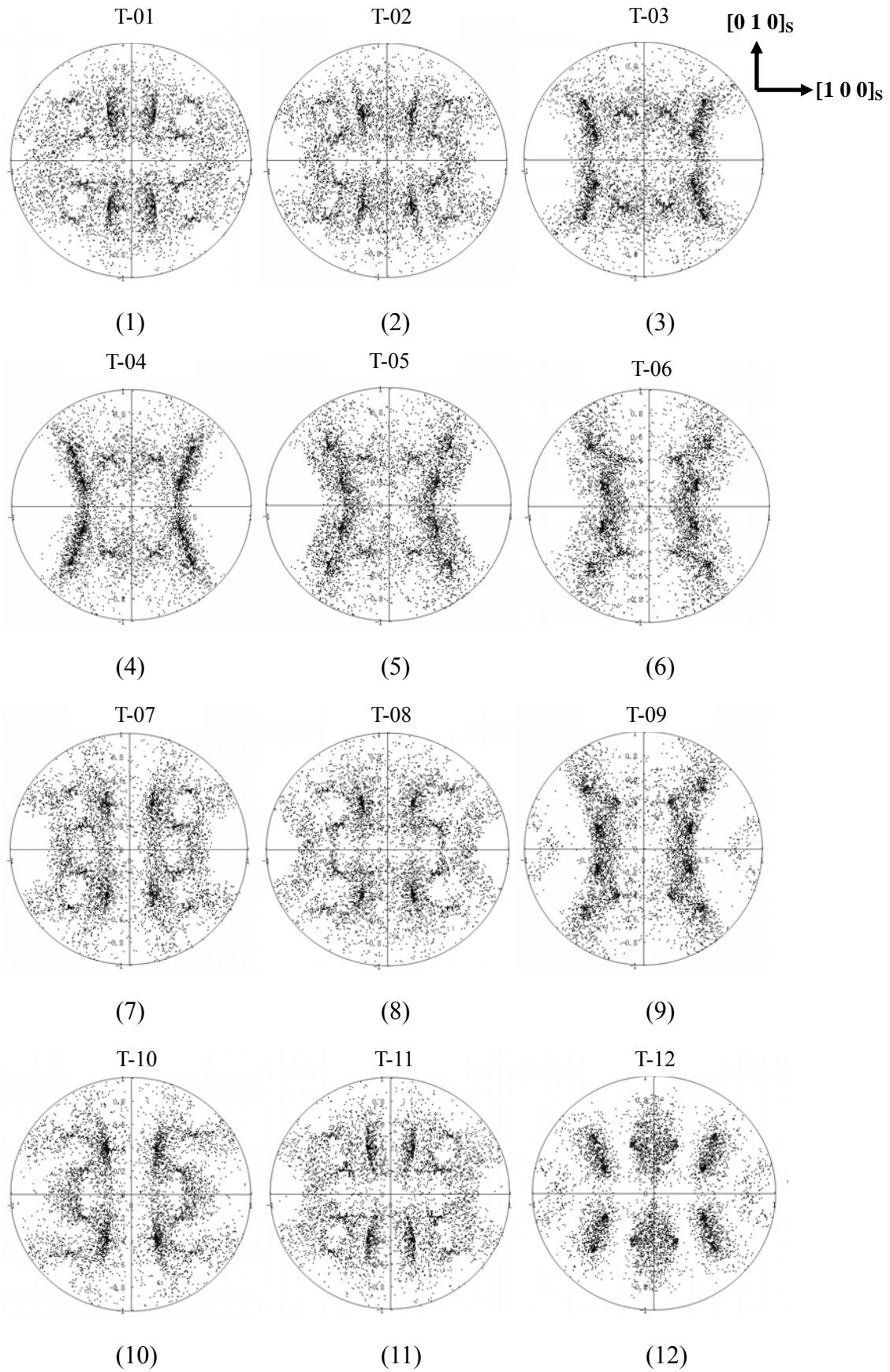


Fig. 4-1-8: 100-pole figures of 12 twinning systems, 2000 grains, tension along $[100]_s$.
 (1) Calculation assuming only the most favored twinning system forming in each grain; (2) ~ (12) assuming only the second to twelfth forming, respectively.

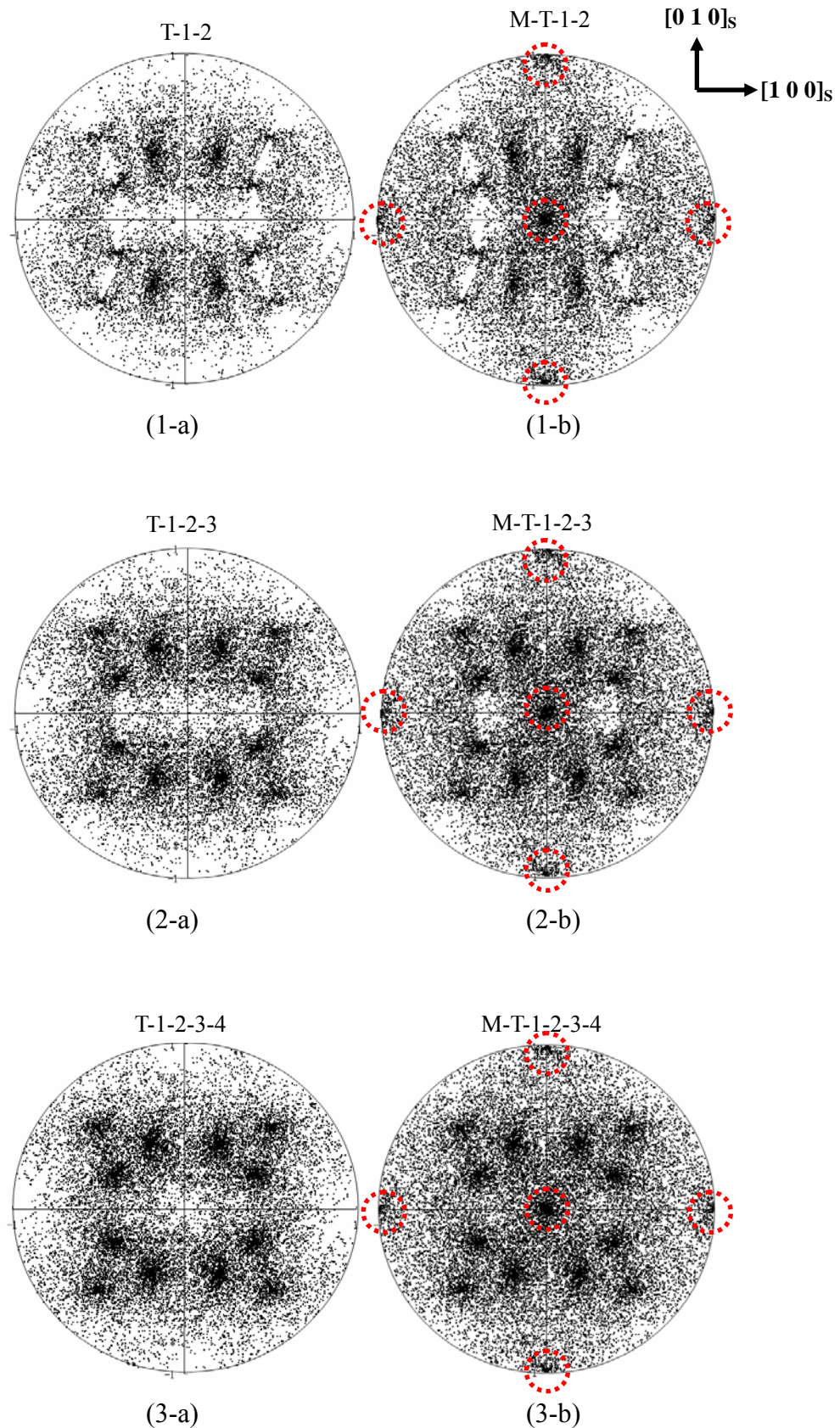


Fig. 4-1-9: Superposition for the individual pole figures in Fig. 4-1-8. (1-a) Superposition of 1, 2; (1-b) 1, 2 and matrix; (2-a) 1, 2, 3; (2-b) 1, 2, 3 and matrix; (3-a) 1, 2, 3, 4; (3-b) 1, 2, 3, 4 and matrix. The ideal positions of Cube are circled red.

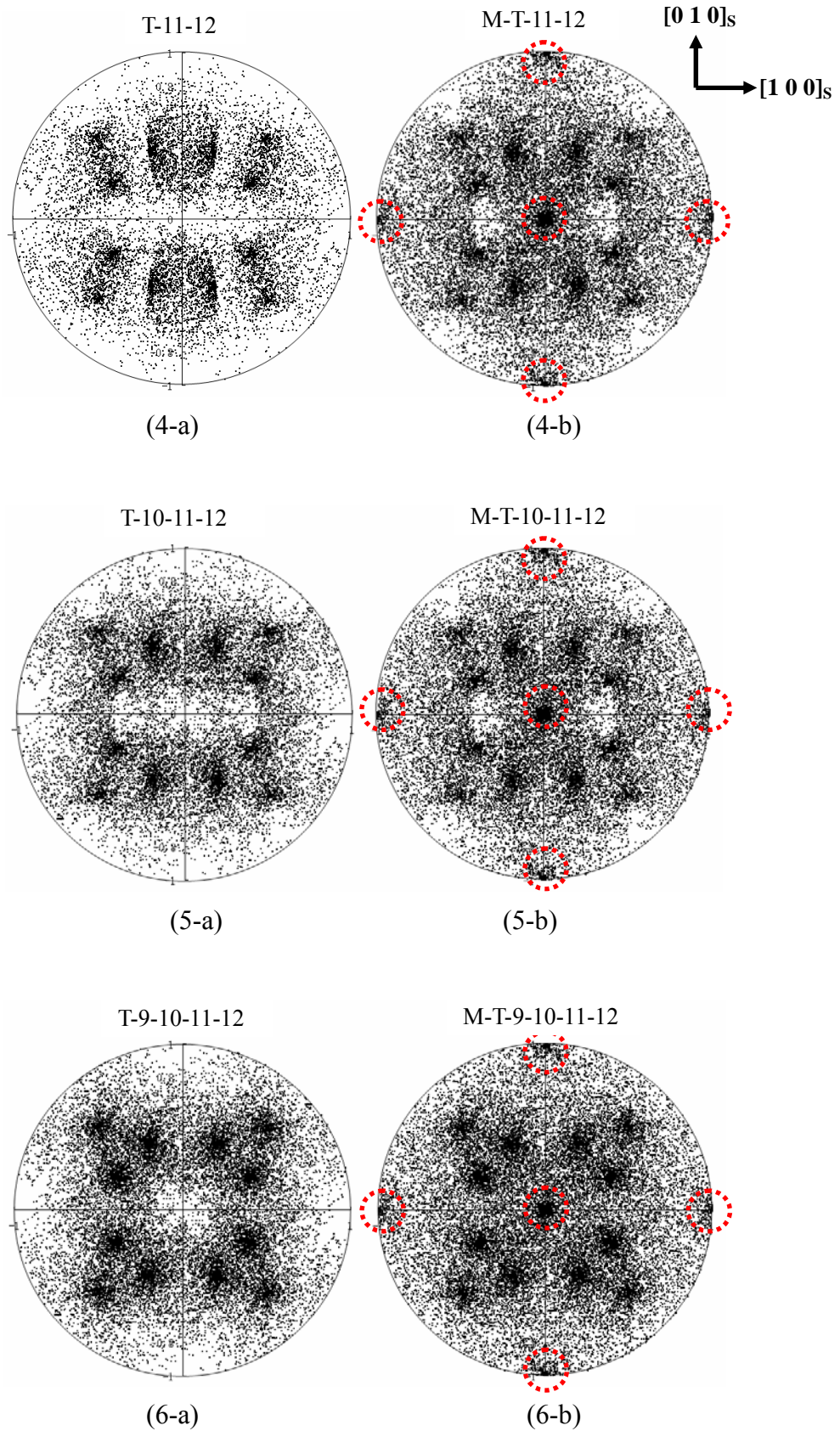


Fig. 4-1-9 continued: Superposition for the individual pole figures in Fig. 4-1-8. (4-a) 11, 12; (4-b) 11, 12 and matrix; (5-a) 10, 11, 12; (5-b) 10, 11, 12 and matrix; (6-a) 9, 10, 11, 12; (6-b) 9, 10, 11, 12 and matrix. The ideal positions of Cube are circled red.

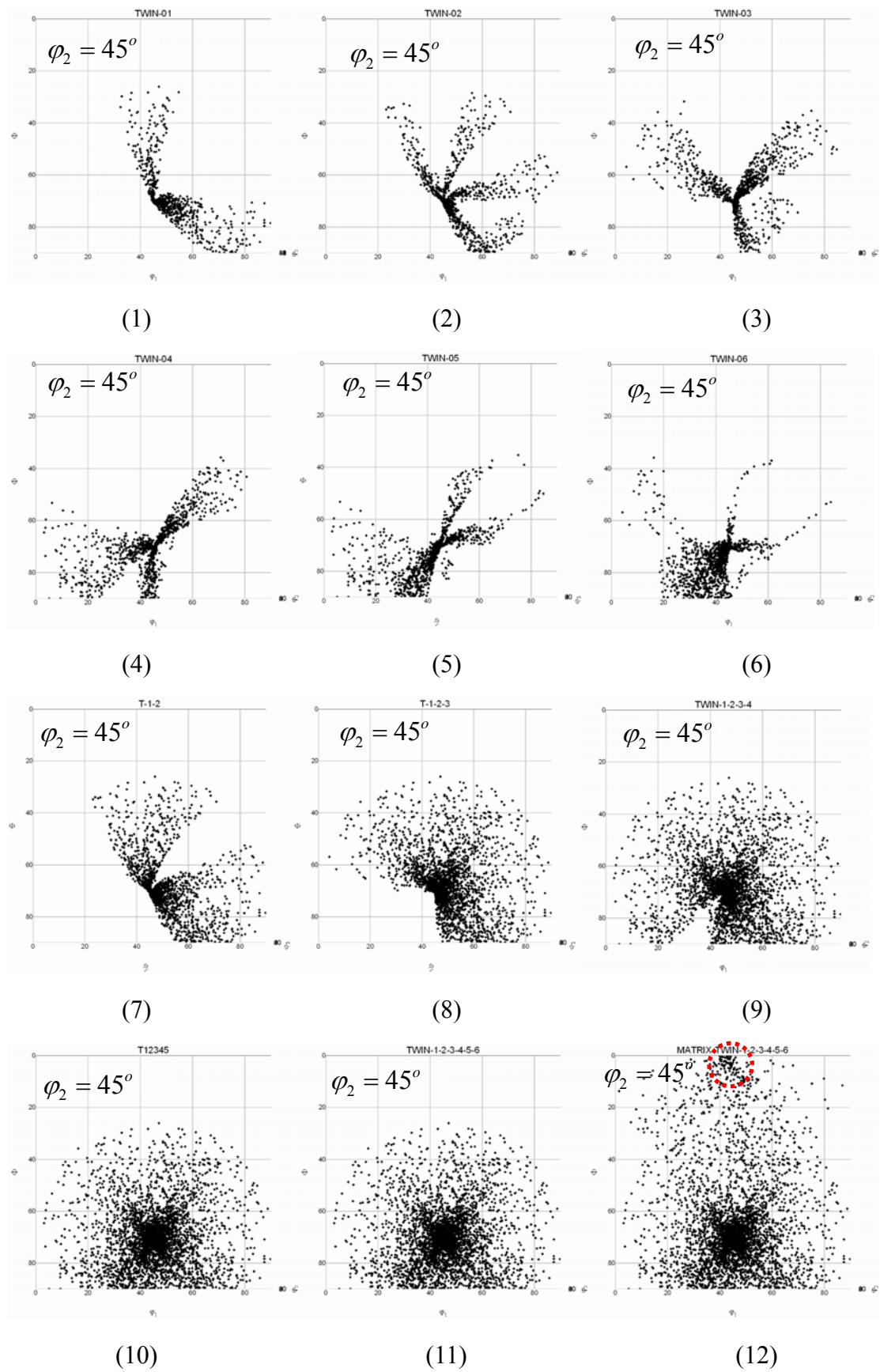


Fig. 4-1-10: Tension along $[100]_s$. $\varphi_2 = 45^\circ$ section ODF. Individual twinning system from the most favored one to the 6th favored one (1-6), and their superimpose (7-12). Position of the red dashed circle is the position of parent austenite on this section.

4-1-3 Comparison with experimental results

Cold rolling

Vercammen [2004b] investigated the tensile testing and cold rolling behaviors of TWIP sheet steel. The sheets were initially hot rolled, then annealed and water quenched. This resulted in a texture of α -fibre and copper components. The maximum intensity was somewhat low and no Cube component was present. This especially-hot treated slab was subsequently cold rolled; the $\varphi_2 = 45^\circ$ ODFs were recorded at different strain levels as shown in Figure 4-1-12

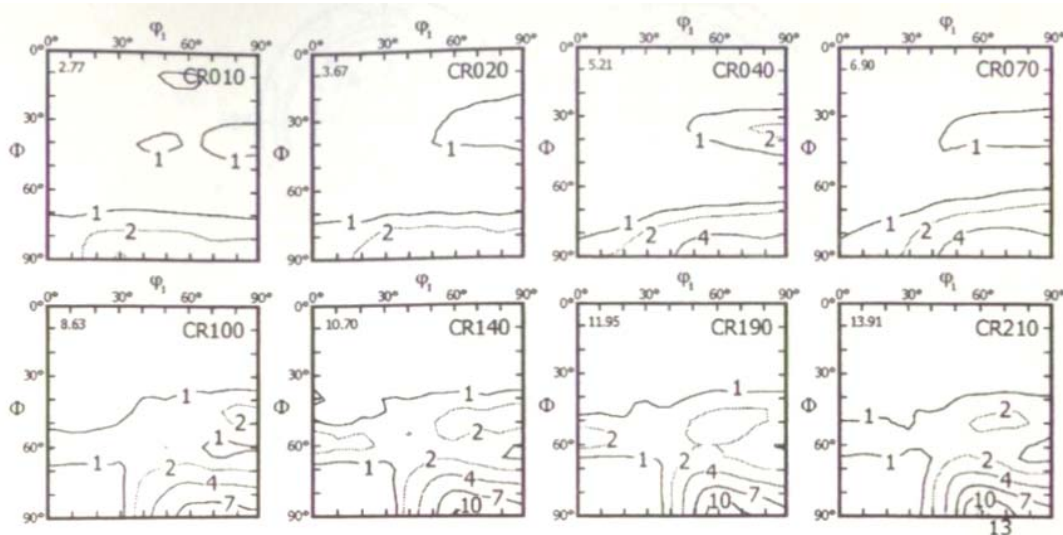


Fig. 4-1-12: Evolution of texture during cold rolling: $\varphi_2 = 45^\circ$ sections of the ODFs of a TWIP-alloy (29.4Mn-3.0Si-3.3Al-0.0033S-0.0049C wt. %) for various rolling strains. The maximum intensity is given in the upper left corner of each section. ‘CRxxx’ stands for cold rolling with xxx% true strain [Vercammen, 2004b].

To reproduce the initial observed texture within the computer model, a combination of austenite texture components was used. Figure 4-1-14 (a) shows a mixture of 50% α -fibre, 25% Copper and the remainder $(112)[\overline{021}]$ for 10000

grains with $\theta = 20^\circ$. This is a reasonable match with the observed texture (Figure 4-1-12, CR010).

It is difficult to estimate the stress state during cold rolling. Kundu [Kundu, 2007] and Mr. Raju Dasu [TATA Steel] assisted with a finite element analysis of an elastic-plastic deformable sheet using commercial software package ABAQUS/Standard (version 6.6) in cold rolling reduction of 60% and suggested a stress tensor

$$(S \sigma S) = \begin{pmatrix} -136 & 0 & -35 \\ 0 & -386 & 0 \\ -35 & 0 & -623 \end{pmatrix}$$

in his research. In this calculation, this tensor is used to simulate the stress state of cold rolling for TWIP steel. At first only one system was assumed to twin the whole of the austenite and the resulting $\varphi_2 = 45^\circ$ ODF section was compared against experimental data to see how the choice of twinning system influences texture. Figures 4-1-14 (b) ~ (f) are these sections for the 6 most favored twinning systems. The combined effects of all 6 systems are illustrated in Figures 4-1-15 and 4-1-16, in an attempt to discover the best match with the observations in Figure 4-1-12.

However, it proved difficult to obtain a reasonable match, perhaps for the following reasons:

The stress state is complicated in rolling, and the one chosen previously may not be realistic. Dislocations are generated during deformation, whose effect is not taken into account. Mechanical twinning is unlikely to be the only deformation mode at large rolling strains. Dislocation plasticity and deformation bands increase and harden the austenite, hindering mechanical twinning. The model based on twinning alone should therefore only apply at rolling strains.

However, when the strain is less than 0.4 (CR040), there is only an increase near Brass and Goss orientation; and twinning systems 1 and 2 do contribute an increase in intensity around Brass and Goss orientation, as denoted by red circles in Figures 4-1-14 (b) and (c), or even twinning system 3 in (d). This may suggest that when the strain is not very high, given the right stress tensor, it should be possible to predict the texture of TWIP steel during the early stages of cold rolling.

Tensile testing

The evolution of the texture during tensile testing is shown in Figure 4-1-13 [Vercammen, 2004b].

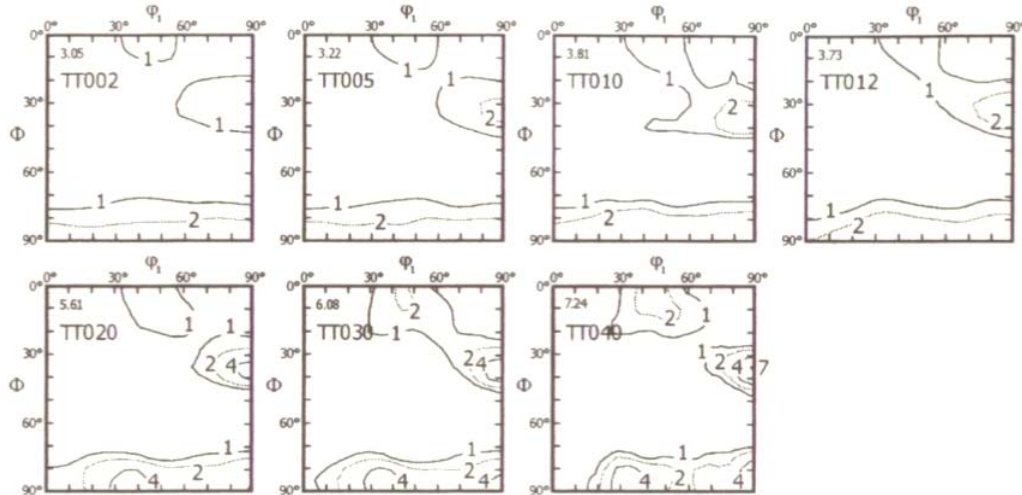


Fig. 4-1-13: Texture formation after tensile testing $\varphi_2 = 45^\circ$ of the ODFs of the TWIP-alloy at different strain levels. The maximum intensity is given in the upper left corner of each section. Levels: 1, 2, 4, and 7. ‘TTxxx’ stands for the tensile testing with a true strain of xxx% [Vercammen, 2004b].

The initial texture was considered as a combination of 50% α -fibre, 25% Copper and 25% Cube, Figure 4-1-17 (a) which matches well with the observed in

Figure 4-1-12, TT002. The stress tensor in this case is $(S \sigma S) = \sigma \begin{pmatrix} 1 & 0 & 0 \\ 0 & 0 & 0 \\ 0 & 0 & 0 \end{pmatrix}$.

The results (Figures 4-1-17 ~ 4-1-19) show that:

- (i) Twinning systems 1 and 2 lead an increase in the vicinity of the cube and Goss orientations, Figure 4-1-17 (b) and (c).
- (ii) During the tensile testing, the orientations are not only redistributed by mechanical twinning, but also by grain rotation. In the absence of grain rotation, there must be a high intensity near $\varphi_1 = 42^\circ$, $\Phi = 70^\circ$ (blue circles), due to twinning on the Cube orientated grains. However, this is not appeared in Figure 4-1-13. This can only be explained by the rotation of grains during

the tensile testing. (Figure 4-1-13 includes true strains ranging from 0.02 to 0.40)

- (iii) There is no significant increase of Rotated Goss orientation on α – fibre and no increase near $\Phi = 20^\circ$ in the experimental Figure 4-1-13. But twinning systems 3 and 4 should appear as denoted in Figures 4-1-17 (c) and (d). It is therefore concluded that these systems are for some reason not activated.
- (iv) The material was not fully twinned because the existence of Copper and Cube orientation would not be expected if the material was fully twinned.

To summarize, in the tensile test, austenite grains twinned partially by twinning systems 1 and 2 and rotated. The superposition of twinning system 1, 2 and matrix, as shown in Figure 4-1-18 (2-b), give a general reasonable match in position with Figure 4-1-13.

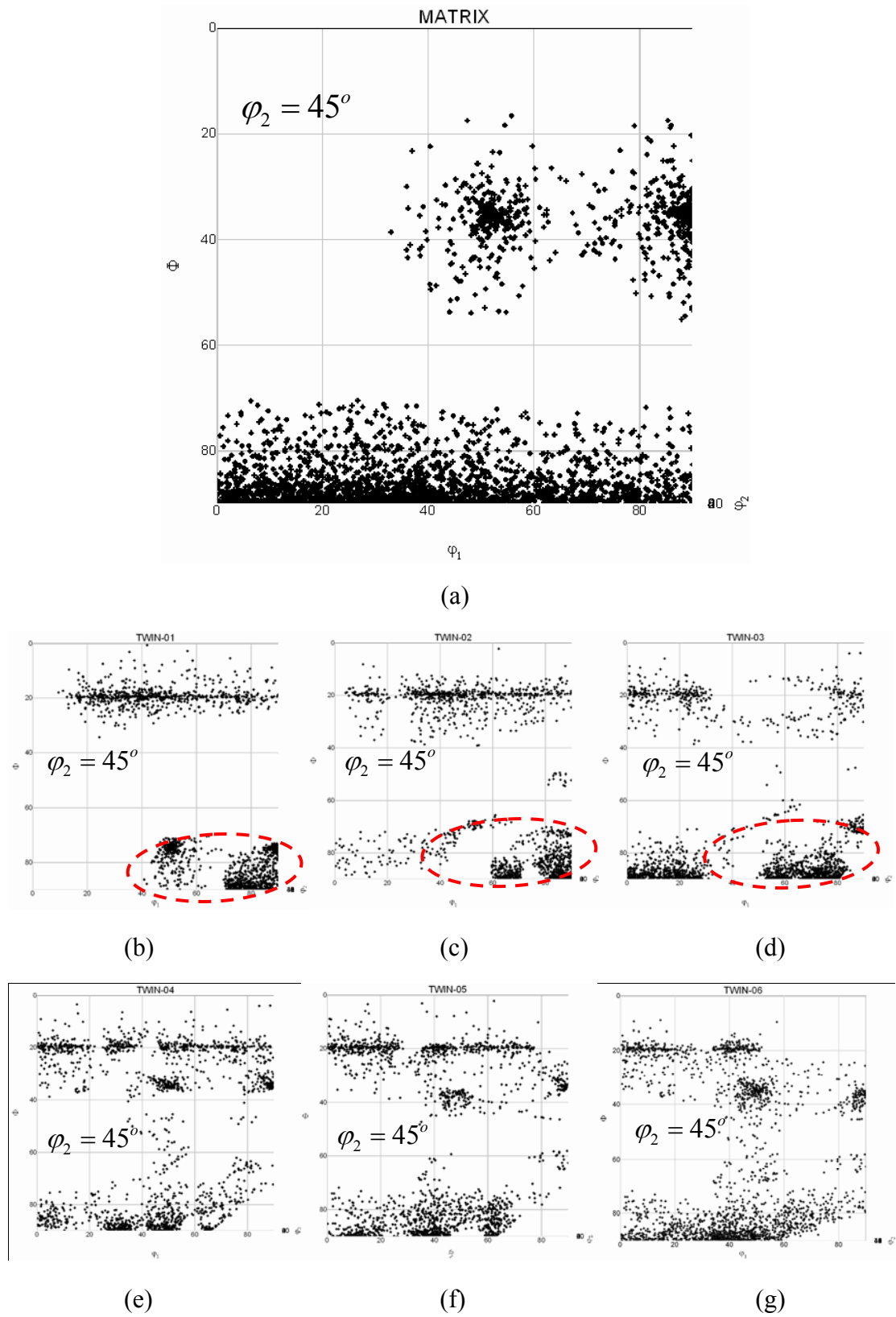


Fig. 4-1-14: Cold rolling. (a) Computer generated texture, in comparison with CR010 in 4-1-11, $\varphi_2 = 45^\circ$ section. (b) ~ (g) $\varphi_2 = 45^\circ$ of individual twin from 1 to 6.

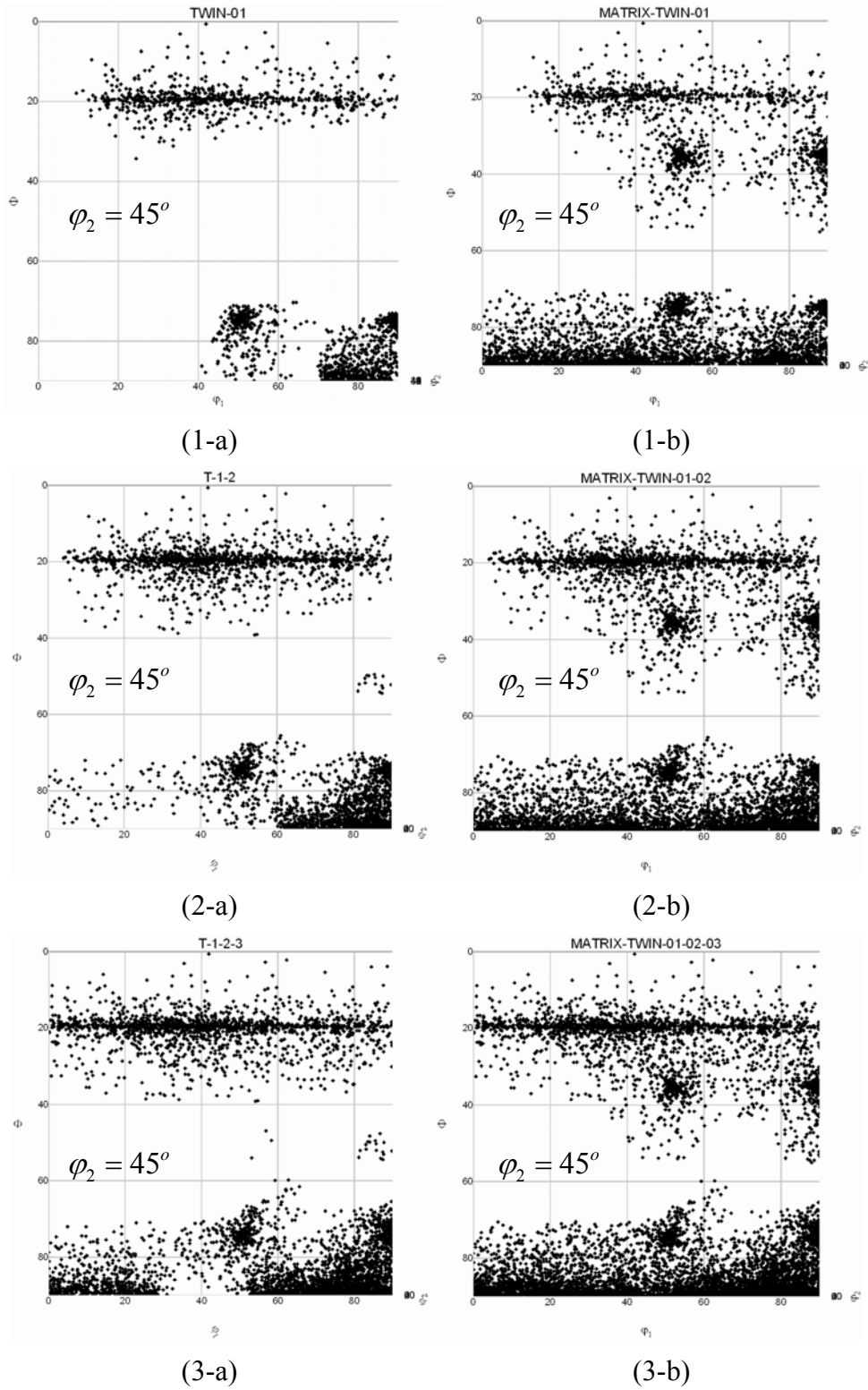


Fig. 4-1-15: Cold rolling. (1-a) Twinning system 1; (2-a), (3-a), superposition of twinning system 1, 2 and 1, 2, 3, respectively; (1-b), (2-b) and (3-b) superposition of (1-a), (2-a), (3-a) with matrix.

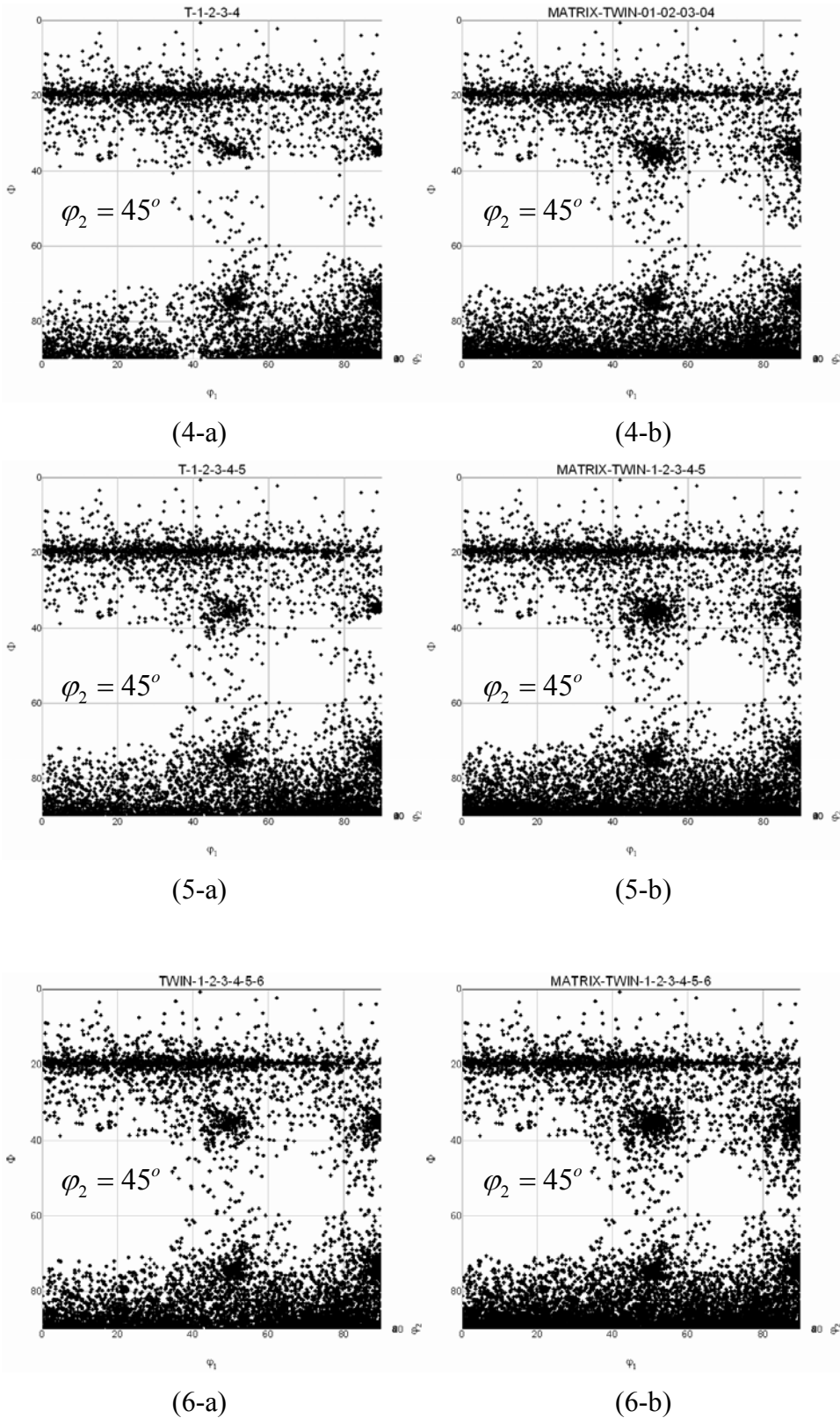


Fig. 4-1-16: Cold rolling. (4-a), (5-a), (6-a), superposition of the favored first 4, 5, 6 twinning systems, respectively; (4-b), (5-b) and (6-b) superposition of (4-a), (5-a) and (6-a) with matrix.

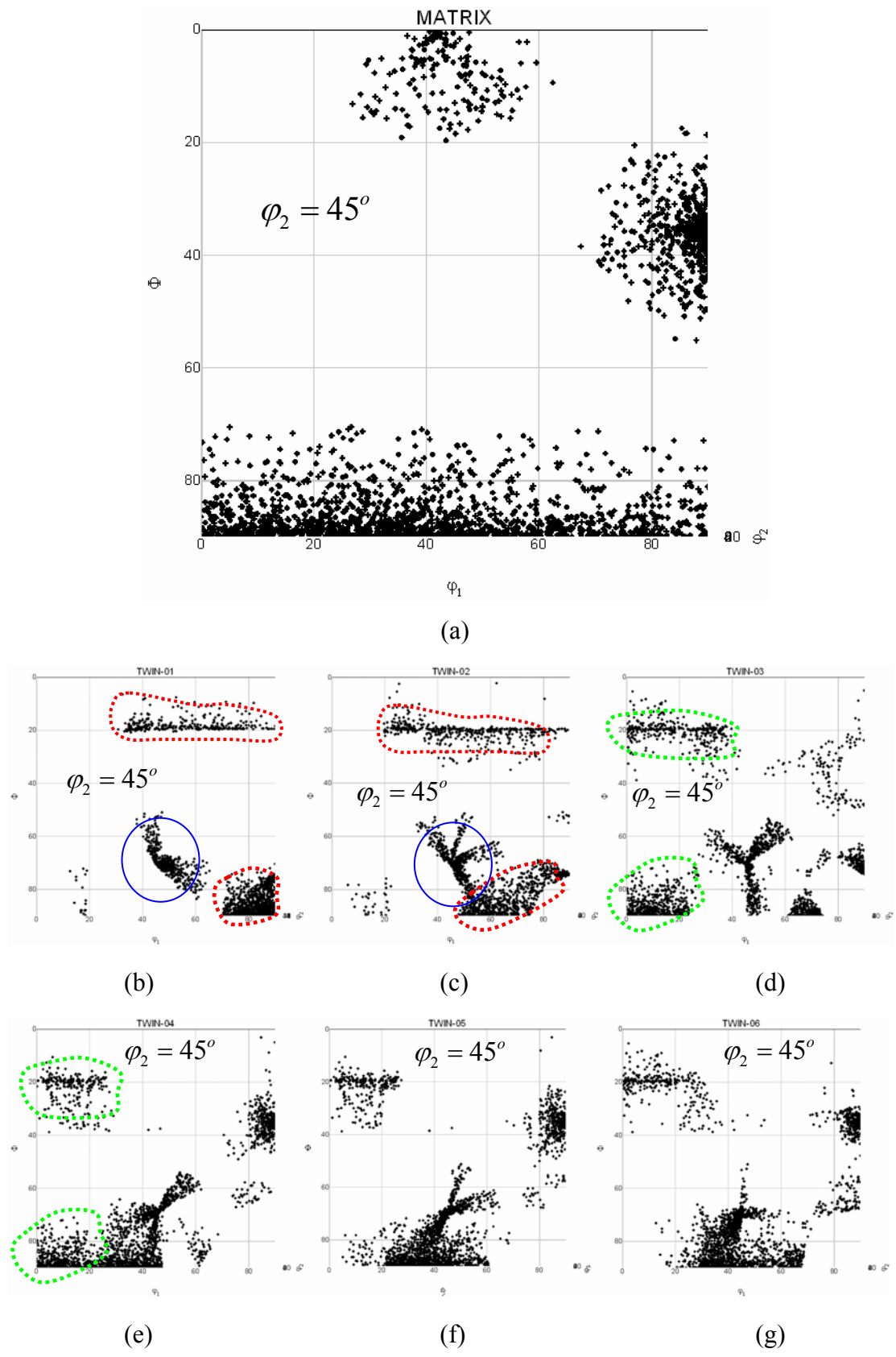


Fig. 4-1-17: Tensile test. (a) Computer generated texture, in comparison with TT002 in 4-1-11, $\varphi_2 = 45^\circ$ section. (b) ~ (g) $\varphi_2 = 45^\circ$ of individual twin from 1 to 6.

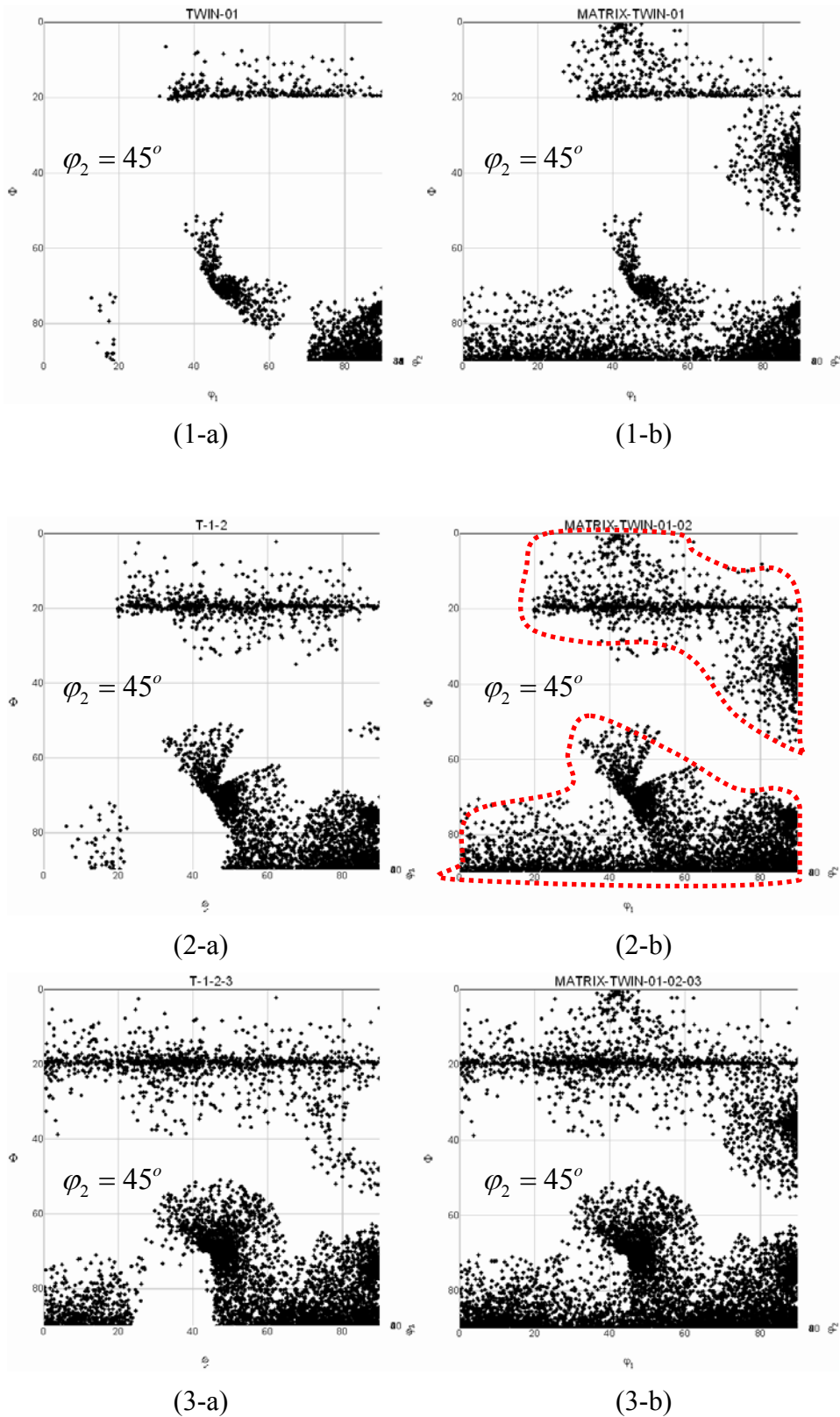


Fig. 4-1-18: Tensile test. (1-a) Twinning system 1; (2-a), (3-a), superposition of twinning system 1, 2 and 1, 2, 3, respectively; (1-b), (2-b) and (3-b) superposition of (1-a), (2-a), (3-a) with matrix.

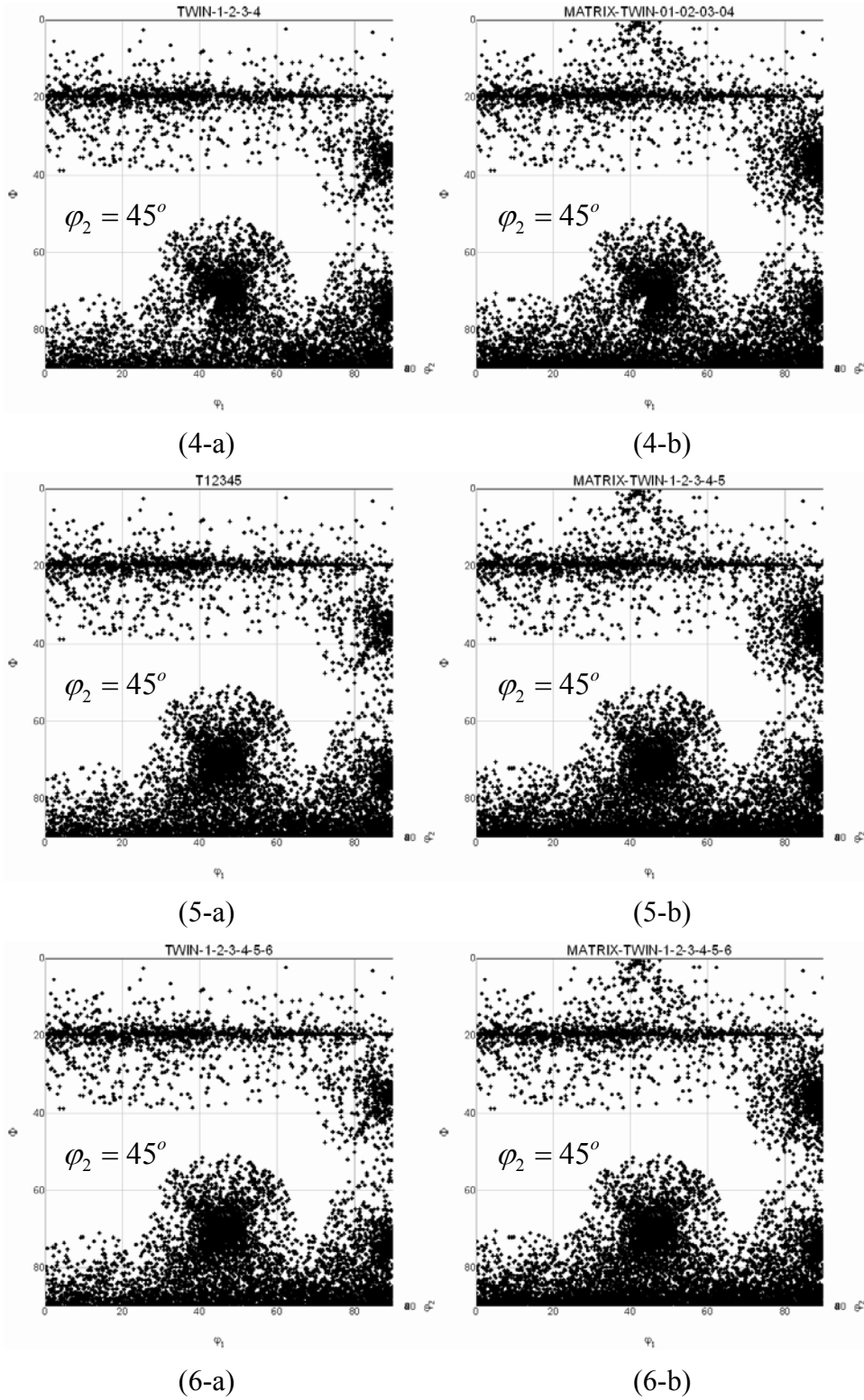


Fig. 4-1-19: Tensile test. (4-a), (5-a), (6-a), superposition of the favored first 4, 5, 6 twinning systems, respectively; (4-b), (5-b) and (6-b) superposition of (4-a), (5-a) and (6-a) with matrix.

4-2 True Strain

In the previous chapter, the true strain was given by equation 3-13-2; but it is necessary to note that that method does not take the rotation of grains into account during the course of twinning deformation. It applies only when the vector \mathbf{OP}' and \mathbf{OP}_2 are parallel to each other, which might not be true case in all possible situations. However in the model used in this work, two reasons can ensure that this procedure is a good approximation which does not lead to large deviations from reality. The first is that in the course of tensile testing the specimen is always constrained by the equipment, which forces the resultant vector \mathbf{OP}_2 to rotate to the position parallel to the initial vector \mathbf{OP}' ; secondly, as proved below, for a polycrystalline sample, when the number of grains increases, the angle between \mathbf{OP}_2 and \mathbf{OP}' (denoted as Φ) becomes small even without considering the constraint of the specimen by the testing equipment.

Consider tensile testing of a sample which is subjected to uniaxial stresses, the simplified stress status of which was given previously. Taking \mathbf{OP}' parallel to $[1\ 0\ 0]_s$, Table 4-2-1 lists the components of vector \mathbf{OP}' and \mathbf{OP}_2 for a polycrystalline specimen with different numbers of randomly oriented grains. Suppose that whole specimen is 100% twinned with different numbers of operating systems, each of which deform the same volume percent of austenite. The result clearly shows that Φ decreases as the number of austenite grains increases. When more than one twinning system is operating, the angle Φ becomes even smaller. In the case of 2000 grains with two twinning system operating in each grain, Φ has a value of that 0.03° , which means \mathbf{OP}' and \mathbf{OP}_2 are almost parallel. In the subsequent calculation of polycrystalline specimen, the number of grains calculated is always chosen above 2000 which makes the difference even smaller.

4-2-1 Orientation dependence of strain, single crystal

Supposing a thin, cylindrical single-crystal of TWIP steel is tensile tested, the tensile axis being along the cylinder axis \mathbf{u} . Assuming that the entire specimen

Table 4-2-1 Angle between \mathbf{OP}' and \mathbf{OP}_2 (Φ) for various number of grains and operating twinning systems.

Number of grains	Number of Operating systems	\mathbf{OP}'	\mathbf{OP}_2	Φ / degrees
1	1	$[1\ 0\ 0]_s$	$[1.6667\ 0.3333\ -0.1667]_s$	12.6
	1, 2	$[1\ 0\ 0]_s$	$[1.6667\ 0.0833\ 0.0833]_s$	35.25
20	1	$[20\ 0\ 0]_s$	$[25.8340\ 1.4925\ 0.4803]_s$	3.47
	1, 2	$[20\ 0\ 0]_s$	$[25.2657\ 0.4378\ 0.1348]_s$	1.04
200	1	$[200\ 0\ 0]_s$	$[260.6316\ 3.9726\ 4.7491]_s$	1.36
	1, 2	$[200\ 0\ 0]_s$	$[254.7677\ -1.2780\ 0.1942]_s$	0.29
2000	1	$[2000\ 0\ 0]_s$	$[2603.7630\ 2.3577\ 12.4698]_s$	0.28
	1, 2	$[2000\ 0\ 0]_s$	$[2547.7570\ -0.4567\ -1.2671]_s$	0.03

deforms by the most favorable twinning system with 100% volume percent, and that the ends of the specimen are always maintained in perfect alignment, a calculation of the plastic strain recorded along the tensile axis can be performed during mechanical twinning.

The method used here was introduced in Chapter 3 and a similar calculation has been reported for α iron with tensile direction \mathbf{u} along $[4\ 4\ 1]$ [Bhadeshia, 2001]. To analysis the strain in polycrystalline, it is interesting and also necessary to find out how the true strain changes as a function of the orientation of the tensile axis \mathbf{u} .

To do that, assuming the basis axes of a single crystal are parallel to the basis axes of reference frame and then the tensile axis $\mathbf{u} = [u_1\ u_2\ u_3]_s$ is obtained by randomly generating its three components. For $\langle 1\ 0\ 0 \rangle_s$ as type **I**, $\langle 1\ 1\ 0 \rangle_s$ as type **II**, and $\langle 1\ 1\ 1 \rangle_s$ as type **III**. The results are shown in Figures 4-2-1 (a) - (h)

In Figure 4-2-1(b), the tensile direction is confined in the $(1\ 0\ 0)_s$ plane with

positive u_1 and u_3 . Each point with coordinate (b, c) in the figure denotes one tensile direction whose components satisfy $u_1 = 0, u_2 = kb, u_3 = kc$ ($k \neq 0$); the distance between the point and the origin O gives the true strain $\varepsilon = \sqrt{b^2 + c^2}$ along that particular tensile direction \mathbf{u} . It is found that the true strain has a maximum value of 0.3466 when the deformation is along type **II** direction, i.e. $[0\ 1\ 1]_S$ in this case, and a minimum value of 0.2027 along type **I** direction, i.e. $[0\ 1\ 0]_S$ and $[0\ 0\ 1]_S$ in the figure.

Figure 4-2-1 (c) shows the strains along the tensile direction when it is confined on the $(\bar{1}\ 1\ 0)_S$ plane. It also shows that the maximum strain is 0.3466 when \mathbf{u} is along type **II** direction, $[1\ 1\ 0]_S$ in this case; and among all directions, a minimum strain is also found along type **III** directions, i.e. $[1\ 1\ 1]_S$ in this case, with the same value as that for type **I** direction.

Figure 4-2-1 (d) gives a ‘strain surface’ along all tensile directions in three-dimensional space. By examining its $[1\ 0\ 0]_S$ projection and $[0\ 1\ 0]_S$ projection, as shown in (e) and (f), it seems it is consisted by 8 ellipsoid balls. This is confirmed by further examining of its $(1\ 0\ 0)_S$ section (g) and $(\bar{1}\ 1\ 0)_S$ section (h).

In Figure 4-2-1 (g), $(1\ 0\ 0)_S$ section of ‘Strain surface’, the curve can be fitted by four circles marked in red dashed lines. Whereas in Figure 4-2-1 (h), $(\bar{1}\ 1\ 0)_S$ section of ‘Strain surface’, a part of the curve can be fitted, but some area as denoted in blue dashed line, can not be fitted using a circle.

These suggest that two axes of each ball are equal and larger than the third axis. A function describing these ellipsoid balls maybe derived mathematically starting from the mathematical crystallographic geography, but this work has not done yet.

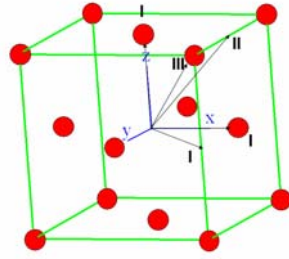
It is interesting to notice that the strain changes continuously with direction. This is reasonable because in certain tensile directions, several twinning systems may be operating simultaneously. When the orientation rotates slightly from those directions, one of these twinning systems continues but the others stop, however, each of these

twinning systems contributes equally to the strain of single crystal.

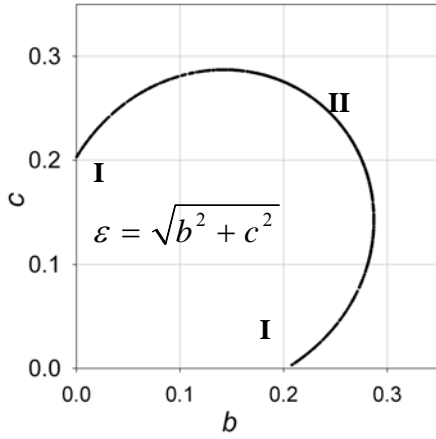
The strains, strain energies and operating twinning system(s) for some tensile directions were calculated and listed in Table 4-2-2.

Table 4-2-2: Operating twinning systems for some directions in single crystal. The strain energy E (J mole⁻¹) is calculated assuming $\sigma=500$ MPa. Because the bases of grain and sample reference frame were set to be parallel, so $[1\ 0\ 0]_s = [1\ 0\ 0]_G$. C, G, Cu, B, E stand for different type of texture as represented in Figure 4-1-1.

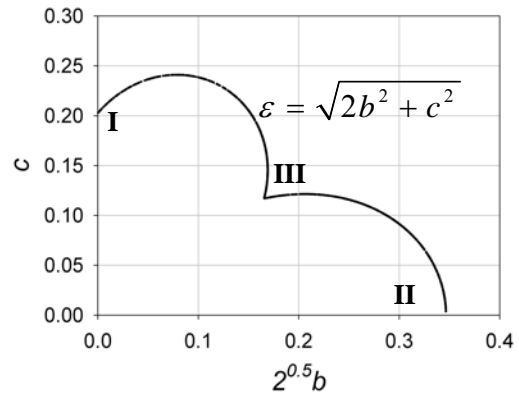
Tensile direction	Operating twinning systems	True strain	$E / \text{J mole}^{-1}$
$[1\ 0\ 0]_G$ (I : C, G)	$(\bar{1}\ \bar{1}\ 1)[\bar{1}\ 2\ 1]$; $(\bar{1}\ \bar{1}\ 1)[\bar{1}\ \bar{1}\ \bar{2}]$; $(\bar{1}\ 1\ \bar{1})[\bar{1}\ 1\ 2]$; $(\bar{1}\ 1\ \bar{1})[\bar{1}\ \bar{2}\ \bar{1}]$; $(1\ \bar{1}\ \bar{1})[1\ \bar{1}\ 2]$; $(1\ \bar{1}\ \bar{1})[1\ 2\ \bar{1}]$; $(1\ 1\ 1)[1\ \bar{2}\ 1]$; $(1\ 1\ 1)[1\ 1\ \bar{2}]$	0.2027	118.75
$[1\ 1\ 1]_G$ (III : Cu)	$(\bar{1}\ 1\ \bar{1})[\bar{1}\ \bar{2}\ \bar{1}]$; $(1\ \bar{1}\ \bar{1})[2\ \bar{1}\ \bar{1}]$; $(\bar{1}\ \bar{1}\ 1)[\bar{1}\ \bar{1}\ \bar{2}]$	0.2027	157.15
$[1\ 1\ 2]_G$ (B)	$(\bar{1}\ 1\ \bar{1})[\bar{1}\ \bar{2}\ \bar{1}]$; $(1\ \bar{1}\ \bar{1})[2\ \bar{1}\ \bar{1}]$	0.2451	196.40
$[1\ 1\ 0]_G$ (II : E)	$(1\ 1\ 1)[1\ 1\ \bar{2}]$; $(\bar{1}\ \bar{1}\ 1)[\bar{1}\ \bar{1}\ \bar{2}]$	0.3466	235.70
Directions near $[1\ 0\ 0]_G$			
$[1\ \bar{0}.01\ 0.02]_G$	$(1\ 1\ 1)[1\ \bar{2}\ 1]$	0.2093	123.73
$[1\ 0.01\ \bar{0}.02]_G$	$(1\ \bar{1}\ \bar{1})[1\ 2\ \bar{1}]$	0.2093	123.73
$[1\ 0.01\ \bar{0}.03]_G$	$(1\ \bar{1}\ \bar{1})[1\ 2\ \bar{1}]$	0.2162	126.09
$[0.98\ \bar{0}.01\ \bar{0}.02]_G$	$(\bar{1}\ \bar{1}\ 1)[\bar{1}\ 2\ 1]$	0.2095	123.85
Directions near $[111]_G$			
$[1\ 1.01\ 0.92]_G$	$(\bar{1}\ \bar{1}\ 1)[\bar{1}\ \bar{1}\ \bar{2}]$	0.2214	172.55
$[1\ 0.92\ 1.01]_G$	$(\bar{1}\ 1\ \bar{1})[\bar{1}\ \bar{2}\ \bar{1}]$	0.2214	172.55
$[1\ 0.92\ 1.03]_G$	$(\bar{1}\ 1\ \bar{1})[\bar{1}\ \bar{2}\ \bar{1}]$	0.2234	174.15
$[0.92\ 1\ 1.03]_G$	$(1\ \bar{1}\ \bar{1})[2\ \bar{1}\ \bar{1}]$	0.2234	174.15



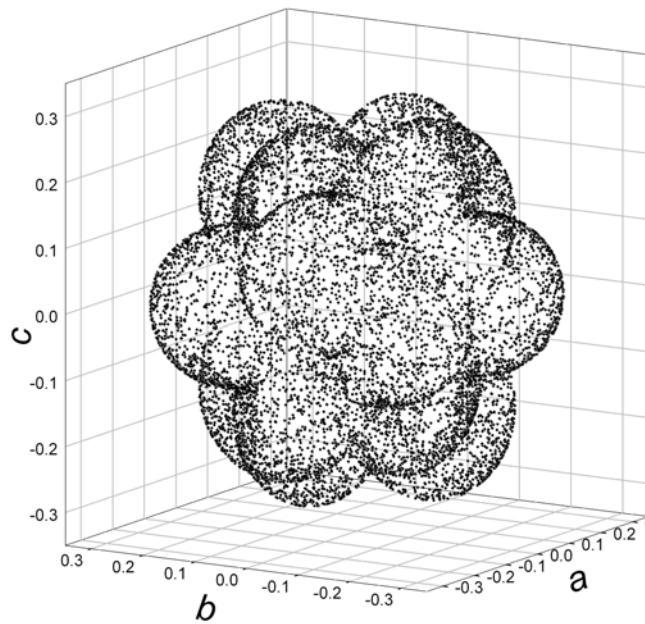
(a)



(b)



(c)



(d)

Fig. 4-2-1 (a) Schematic representation of three types of orientations; (b), (c) and (d): The dependence of strain on deformation directions. In (b) true strain is given as $\varepsilon = \sqrt{b^2 + c^2}$ and in (c) $\varepsilon = \sqrt{2b^2 + c^2}$ whereas in (d) $\varepsilon = \sqrt{a^2 + b^2 + c^2}$.

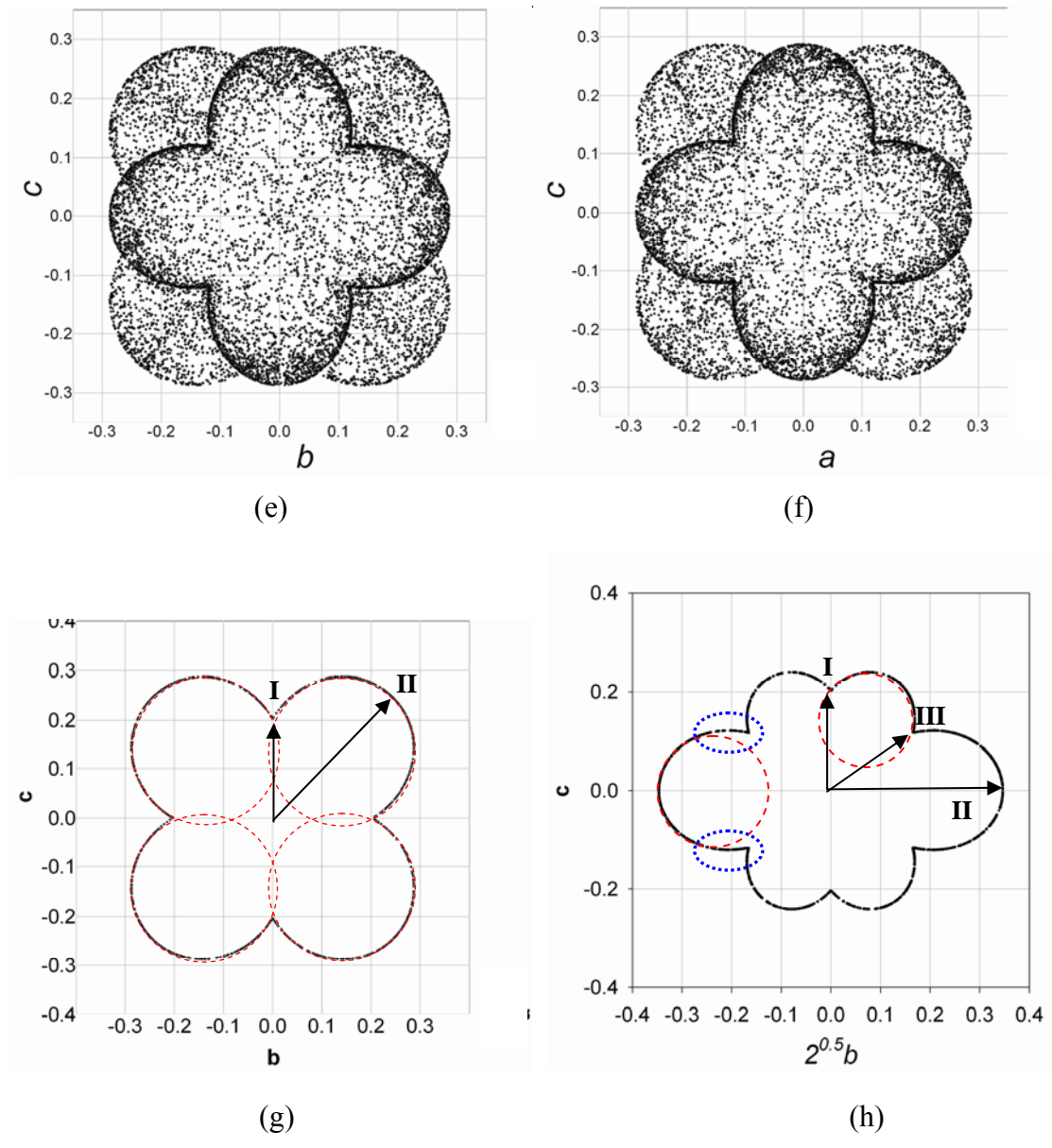


Fig. 4-2-1 continued: 'Strain surface' projected along $[1\ 0\ 0]_s$ (e) and along $[0\ 1\ 0]_s$ (f); $(1\ 0\ 0)_s$ section (g) and $(1\ 1\ 0)_s$ section. Curve in (g) and some part in (h) can be fitted by circles, as marked as red dashed line, but some part can not as rounded by blue dashed line. This suggests an ellipsoid shape. Three types of directions are also denoted in the (g) and (h).

A similar calculation for uniaxial compression for single crystal was also conducted. The ‘strain surface’ is much more complicated than that of tension as shown in Figures 4-2-1 (i) ~ (k). Three features are evident: i) strain does not change continuously in three-dimensional space in compression, as shown in (i) and (k); ii) Generally when true strain along one direction is small in tension then it is large in compression and *vice versa*; iii) strain along $\langle 110 \rangle_s$ is zero. The zero strain is caused by the changing of $\langle 110 \rangle$ to $\langle 0.2357 \ 0.9428 \ -0.2357 \rangle$, resulting the same magnitude. This indicates that the systems which do not comply with the compression strain are being forced to form. In literatures, $\langle 110 \rangle$ is found stable in compression [Yang *et al.*, 2006].

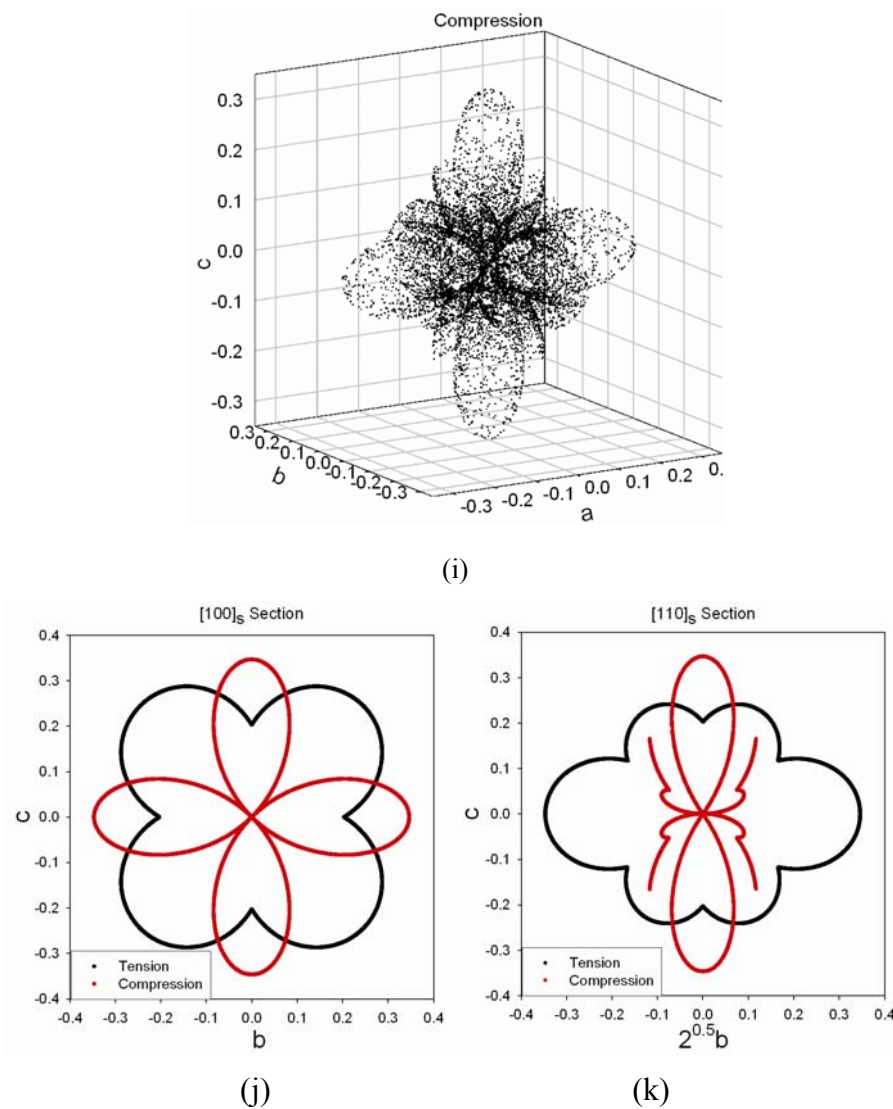


Fig. 4-2-1 continued: ‘Strain surface’ for single crystal in compression (i) and its [100] section (j) and [110] section (k), denoted in red. Dark lines are sections in the case of tension.

4-2-2 Dependence of strain on twinning system

In the calculations presented here, a polycrystalline sample consisting of 10000 randomly orientated grains was subjected to a tensile stress along $[1\ 0\ 0]_s$. It was assumed that each grain was fully twinned with only one twinning system operating, but it did not necessarily the most favoured one. The strain was then calculated for all 12 twinning systems individually, beginning with the most favoured one. Table 4-2-3 lists the strains along three sample reference frame axes, plotted in Figure 4-2-2.

The results reveal at least three features:

(i) The strains are not isotropic, with each set having both negative and positive values. This is reasonable because the mechanical twinning is a simple shear, without any volume change. Since there is an elongation (or compression) along one direction, there must be at least one compression (or elongation) along the other two perpendicular directions. In the case of randomly oriented austenite matrix, strains along $[0\ 1\ 0]_s$ and $[0\ 0\ 1]_s$ are always equal.

(ii) The strain from the most favored twinning system has a maximum value; it then decreases as the twinning system changes from the most favored ones to those which are less favored. This is consistent with the strain energy variant selection criterion used previously because the most favoured system has the maximum strain and consequently the highest energy reduction.

(iii) Starting from twinning system 7, the strain along $[1\ 0\ 0]_s$ becomes negative despite the application of a tensile strain along $[1\ 0\ 0]_s$. This is because the systems which do not comply with the tensile strain are being forced to form in this simulation. Systems 7-12 generally are not favorable from an energy reduction point of view.

It follows that only the six favoured twinning systems should be considered in the calculation. Supposing that in each 100% twinned grain only favoured systems (≤ 6) are allowed to form in equal proportion. Table 4-2-4 lists the results, plotted in Figure 4-2-3. It shows that as the number of operating twinning systems increases, the true strain recorded along $[1\ 0\ 0]_s$ decreases linearly. This is firstly because the

Table 4-2-3: The true strains along three sample reference frame axes as a function of the operating twinning systems. 10000 randomly oriented grains, 100% twinning. Strain energy E (J mole^{-1}) was calculated assuming a tensile stress of 500 MPa.

Operating twinning system index	Strain along $[1\ 0\ 0]_s$	Strain along $[0\ 1\ 0]_s$	Strain along $[0\ 0\ 1]_s$	$E / \text{J mole}^{-1}$
1	0.2635	-0.1633	-0.1635	131.75
2	0.2196	-0.1301	-0.1319	109.80
3	0.1445	-0.0823	-0.0795	72.25
4	0.0843	-0.0451	-0.0449	42.15
5	0.0378	-0.0196	-0.0192	18.90
6	0.0211	-0.0129	-0.0085	10.55
7	-0.0024	0.0041	-0.0017	-1.20
8	-0.0221	0.0118	0.0099	-11.05
9	-0.1458	0.0662	0.065	-72.90
10	-0.2136	0.0912	0.0924	-106.80
11	-0.276	0.1136	0.1142	-138.00
12	-0.297	0.1203	0.1215	-148.50

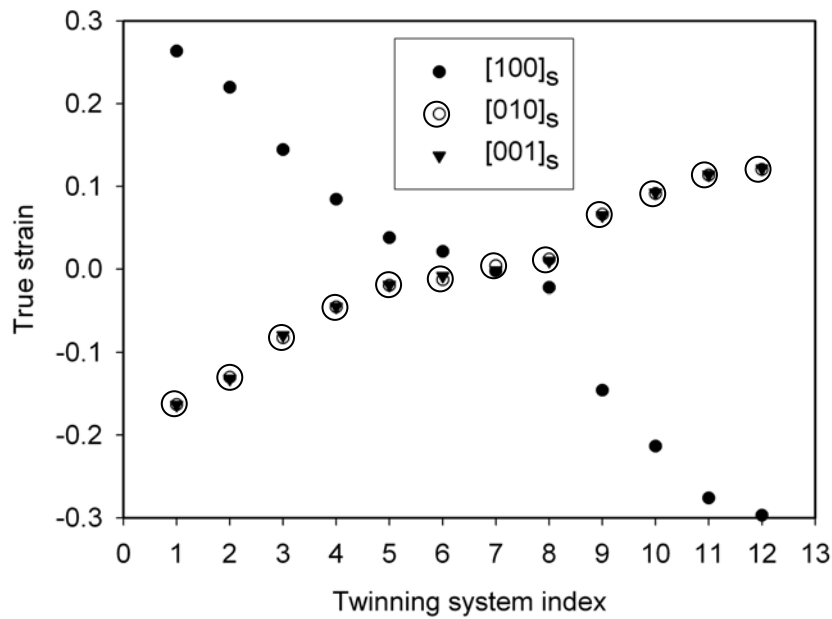


Fig. 4-2-2: The true strain as a function of different operating twinning systems.

contribution of less favoured twinning systems to the strain is less and secondly the strains due to the different systems can mutually compensate.

It is emphasized here that because the relationship between the interaction energy and the fraction transformed is not clear at present. It has therefore assumed that all favoured systems form in equal proportion in spite of their difference in strain energy.

Table 4-2-4: Strains for the groups of most favored systems forming in equal fractions up to 100%

Number of twinning systems	volume of each twin(%)	Strain along $[1\ 0\ 0]_s$	Strain along $[0\ 1\ 0]_s$	Strain along $[0\ 0\ 1]_s$
1	100.00	0.2635	-0.1633	-0.1635
2	50.00	0.2418	-0.1466	-0.1476
3	33.33	0.2104	-0.1247	-0.1244
4	25.00	0.1804	-0.1042	-0.1039
5	20.00	0.1534	-0.0867	-0.0864
6	16.67	0.1325	-0.074	-0.073

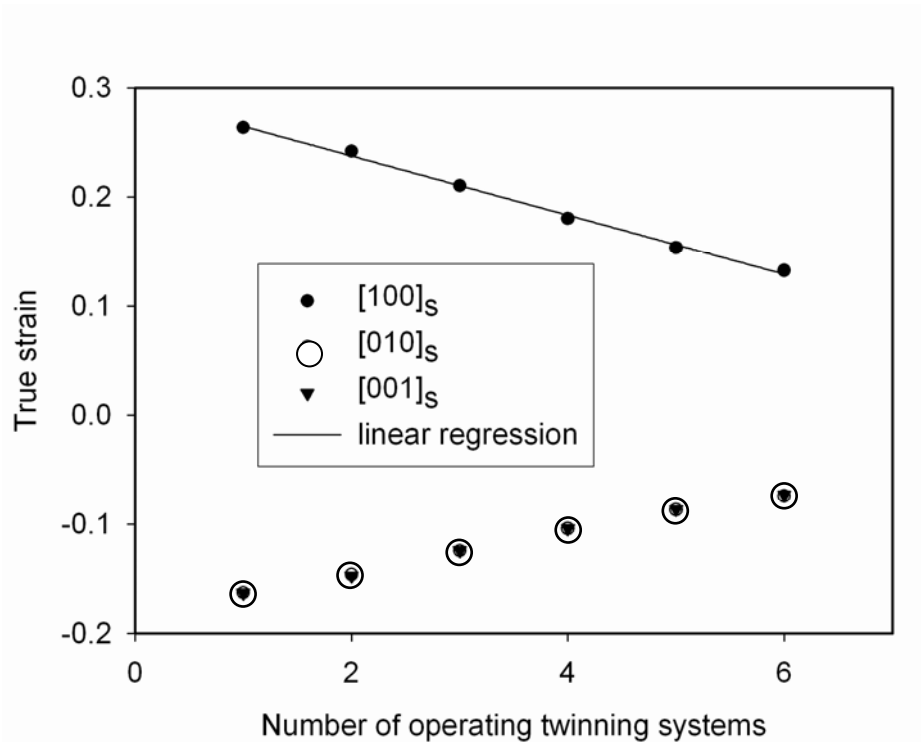


Fig. 4-2-3: Strain varies with the number of operating systems.

4-2-3 Dependence of strains on texture

It is often the case that the parent austenite grains in polycrystalline samples exhibit crystallographic texture. The calculation of strains for textured austenite has also been carried out.

As described previously, the intensity of texture can be changed by altering the maximum rotation angle θ of the axis-angle pair: the smaller the θ , the stronger is the texture. In order to discover the relationship between the true strain from twinning and the intensity of texture, calculations were conducted for 10000 textured grains allowing only the most favoured twinning system to operate with 100% twinning.

Figure 4-2-4 shows the true strain along $[1\ 0\ 0]_s$ when textured austenite polycrystalline undergoes mechanical twinning under the influence of a uniaxial tensile stress applied along $[1\ 0\ 0]_s$. Six types of textures with different intensities were considered and some conclusions can be made from these results:

- (i) Strain varies with texture, but generally the strain of E-orientation textured austenite is largest; strains for both Brass and α -fibre are nearly the same but smaller than E orientation; for Copper strain is even smaller and the smallest strain comes to both Cube and Goss (they are overlapped in the figure).
- (ii) For some orientations such as Brass, Copper and α -fibre, the strain for single crystal (when $\theta = 0^\circ$ the orientations for all grain are the same which means the whole piece can be regarded as a single crystal) is nearly the same as the strain for polycrystalline specimen when the rotation angle is limited to a very small value; whereas for some other orientations such as Cube, Goss and E-orientation, a sudden drop in strain from single crystal to polycrystalline is observed.
- (iii) The strain changes with the intensity of texture. For all the orientations except Copper and E orientations, as θ increases, so does the strain. For Copper and E orientations, it increases at the beginning but later on it decreases. However they all asymptotically tend to the randomly oriented austenite.

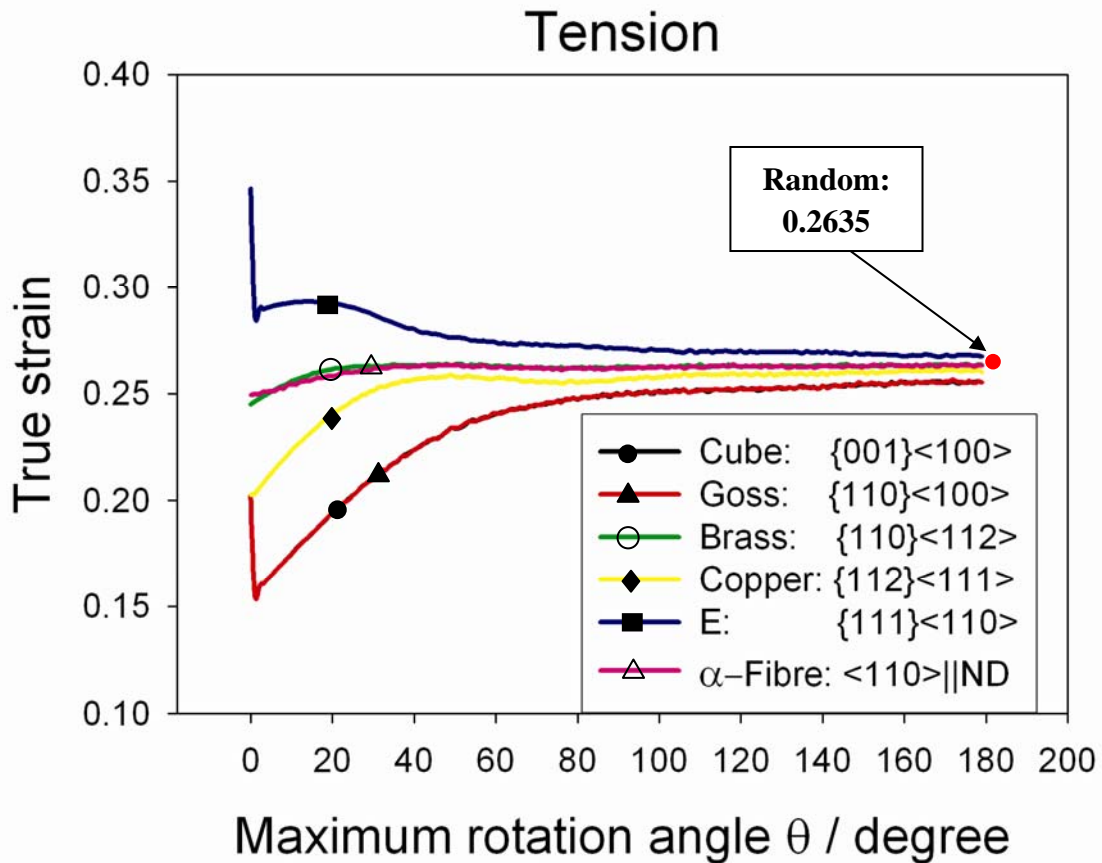


Fig. 4-2-4: The strain along $[1\ 0\ 0]_s$ when austenite polycrystalline samples undergo mechanical twinning under the influence of a uniaxial tensile stress applied along the same $[1\ 0\ 0]_s$ direction, assuming that only the most favored twinning system is operating and the whole sample is 100% twinned. Six different austenite textures are presented: Cube, Goss, Brass, Copper, E and α -Fibre. Cube and Goss overlapped. Red dot denotes the strain of randomly oriented austenite polycrystalline.

Why do some orientations show a sudden drop in strain when the specimen changes from single crystal to polycrystalline?

The directions that are parallel to the tensile axis are $\langle 100 \rangle$ type directions for both Goss and Cube, $\langle 111 \rangle$ for copper, $\langle 112 \rangle$ for Brass, $\langle 110 \rangle$ for E orientation and random for α -fibre textured austenite and randomly oriented austenite. When the rotation angle is small, the tensile direction in each grain rotates little around these directions. This is schematically represented in Figure 4-2-5, $\langle 110 \rangle$

section of 'strain surface' of single crystal.

On the one hand, Figure 4-2-5 shows that the tensile directions near $\langle 110 \rangle$ contribute the most to strain, followed in descending order by $\langle 112 \rangle$, $\langle 111 \rangle$ and $\langle 100 \rangle$.

When the operating twinning system for a single crystal is calculated for these ideal directions, different numbers of twinning systems operate (Table 4-2-2).

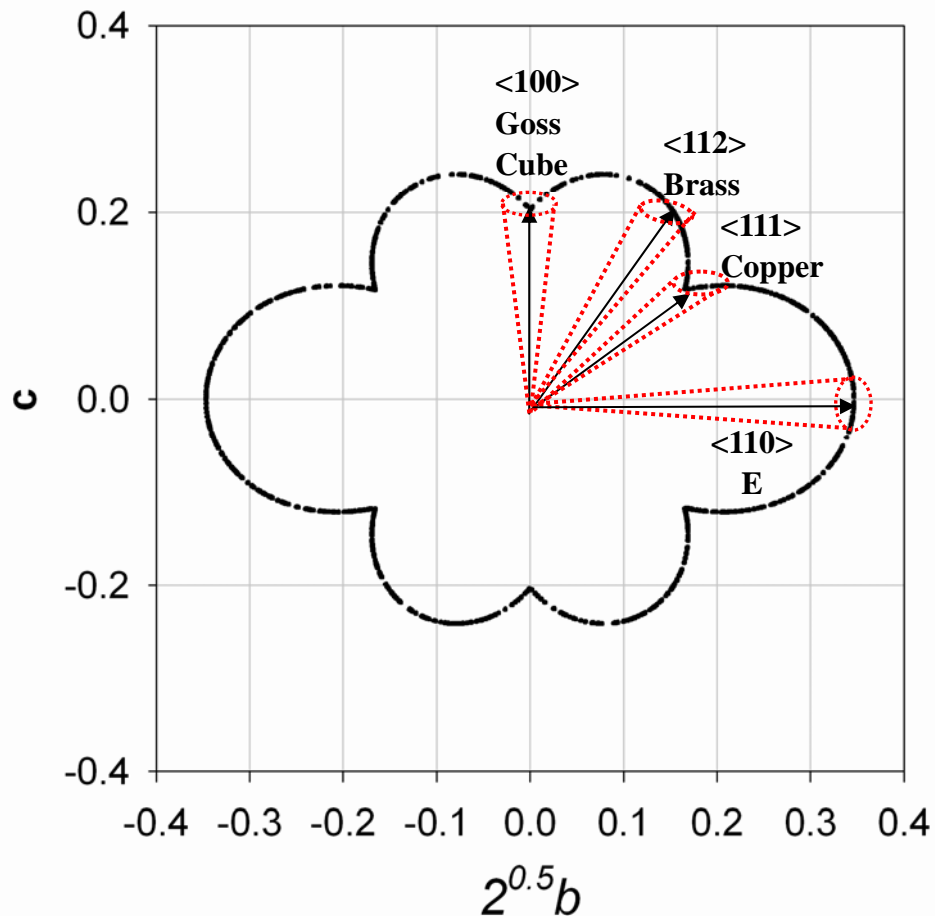


Fig. 4-2-5: $\langle 110 \rangle$ section of 'strain surface' of single crystal. The ideal orientations along $[1\ 0\ 0]_s$ for Goss, Cube, Brass, Copper and E-orientation.

Taking Cube and Copper as an example, notice that for $\langle 100 \rangle$ there are 8 equivalent twinning systems so that when the orientation of a second grain is slightly different from the ideal Cube orientation, there are 8 choices of twinning modes. In other words, given sufficient number of grains, these 8 twinning systems will be operating in the sample. For Copper, three equivalent twinning systems for ideal Copper $\langle 110 \rangle$ direction, hence the operating twinning system for the second grain

which is oriented slightly different from ideal orientation will be one of these three.

But for these three twinning systems, the components of their twinning directions $[\bar{1} \bar{2} \bar{1}]$, $[\bar{2} \bar{1} \bar{1}]$ and $[\bar{1} \bar{2} \bar{1}]$, are all negative, which means the twinning displacement for all the grains will point to one dimension in three-dimensional space, resulting in a small dispersion of twinning displacement. However for eight twinning systems of ideal Cube orientation, their twinning directions are pointing randomly in three-dimensional space, which gives a very large dispersion of twinning displacement. This explains why both Cube and Copper have the same strain from single crystal, but very different in the strain of polycrystalline: twinning directions for Cube texture pointing randomly and hence it has a sudden drop of strain from single crystal to polycrystalline but Copper does not.

A calculation of different number of grains validated this explanation. Details are listed in Table 4-2-5.

Table 4-2-5: Strain along $[1 0 0]_s$ as a function of different number of grains, Cube and Copper case. Maximum rotation angle $\theta = 0.001^\circ$, most favored twinning system operating, 100% twinned.

Number of grain	Strain along $[1 0 0]_s$	
	Cube	Copper
1	0.2027	0.2027
2	0.1592	0.2012
3	0.1553	0.2014
5	0.1546	0.2013
10	0.1550	0.2009

For the ideal Brass orientation, the operating twinning directions all pointing to the same dimension in three-dimensional space, and for Copper this is also the case. A slight change in tensile direction does not change this. The computer program uses the same random number generator for all calculations, so the rotation matrices relating the reference grain and generated grain are the same each time the calculation is

repeated. The magnitude of strain from each grain in the polycrystalline sample makes the main contribution to the final value of strain. For ideal single crystal in Brass orientation, the strain is higher than that of ideal Copper orientation, hence Brass textured polycrystalline has a higher strain.

For Brass, the strain of its single crystal is slightly smaller than that from a randomly oriented matrix, but as θ increases, its strain will gradually increase. For α -Fibre, because its normal direction is $[110]_{M_1} // [010]_S$, hence its tensile direction must be on one of $\langle 110 \rangle$ sections of 'strain surface', so for polycrystalline α -Fibre, its strain should also be an average of the strains for all the directions on this section and increases as θ increases, until it reaches a maximum value.

Considering the sudden drop for the strain of E orientation, which is followed by then an increase and another decrease, the explanation lies in the fact that $[1\ 1\ \bar{2}]$ and $[\bar{1}\ \bar{1}\ \bar{2}]$ do not point to the same dimension. However because the absolute value of its single crystal strain is largest, its starting point for the polycrystalline state is still very high. Then a general increasing rule is followed. But, when rotation angle is higher than a certain angle, around 20° in the figure, the strains for single crystal becomes small so it finally drops to an average value.

A similar explanation applies to Copper strain-angle curve.

The overlap of Cube and Goss strain-angle curve is also naturally expected since they have the same direction, $\langle 110 \rangle_G$ parallel to the tensile direction.

Because the selections of operating twinning system in tension and compression are different, the true strains from twinning for tension and compression must be different. Figure 4-2-6 shows the true strain along $[1\ 0\ 0]_S$ when textured austenite undergoes mechanical twinning under uniaxial compression applied along $[1\ 0\ 0]_S$. The tendency of strain curve for each texture is evidently different from that in the tensile test (Figure 4-2-4).

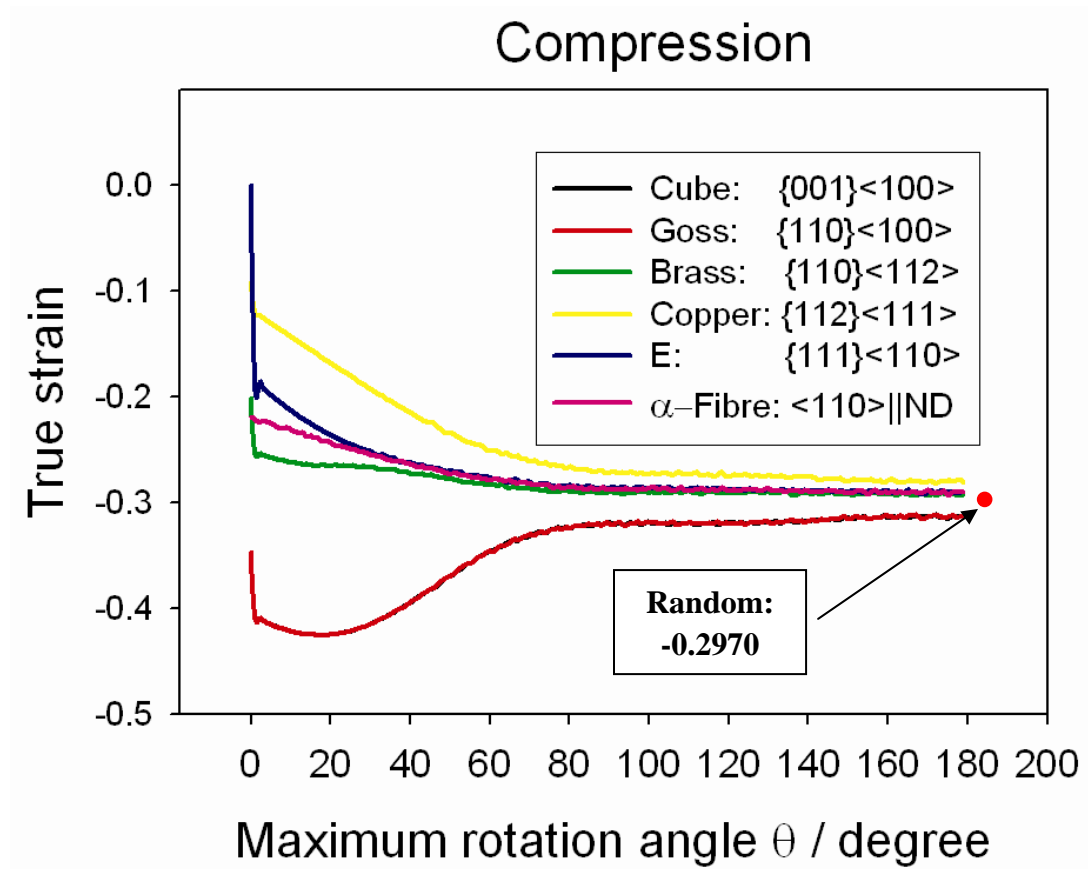


Fig. 4-2-6: The strain along $[1\ 0\ 0]_s$ when austenite polycrystalline samples undergo mechanical twinning under the influence of a uniaxial compression applied along the same $[1\ 0\ 0]_s$ direction, assuming that only the most favored twinning system is operating and the whole sample is 100% twinned. Six different austenite textures are presented: Cube, Goss, Brass, Copper, E and α -Fibre. Cube and Goss overlapped. Red dot denotes the strain of randomly oriented austenite polycrystalline.

The strains along $[0\ 1\ 0]_S$ and $[0\ 0\ 1]_S$ for different types of textures as a function of maximum rotation angle were also calculated, and Figures 4-2-7 (a) ~ (f) show the results in the case of uniaxial tension.

Beside the tendency that all strains asymptotically approach to the strains of randomly oriented austenite, another conclusion is obvious: for Cube, Goss and Copper textured sample, their strains along $[0\ 1\ 0]_S$ and $[0\ 0\ 1]_S$ overlap; however for those others, this character is not observed.

The origin of this difference can also be found by examining their tensile direction: $\langle 1\ 0\ 0 \rangle_{M_1}$ and $\langle 1\ 1\ 1 \rangle_{M_1}$ directions have four-fold and three-fold rotational symmetry, respectively; however for the others, there is no rotational symmetry.

It is this symmetry that causes the same mechanical behaviors along the other two perpendicular directions. However, it is necessary to note that though the strains along $[0\ 1\ 0]_S$ and $[0\ 0\ 1]_S$ are equal, it does not necessarily mean the strain along all directions on $(1\ 0\ 0)_S$ are equal. For instance, the strain along $[0\ 1\ 0]_S$ is different from that along $[1\ 0\ 2]_S$.

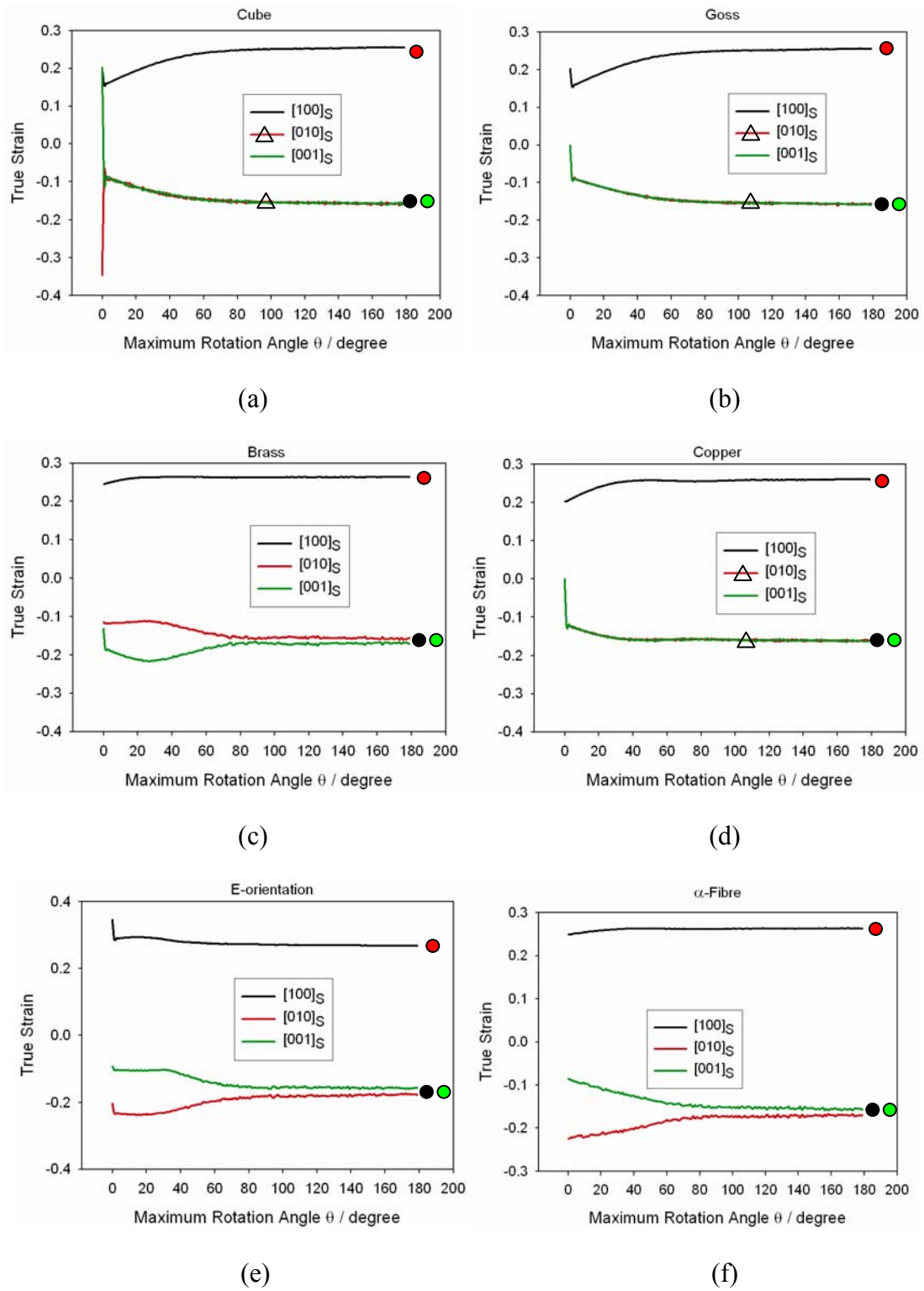


Fig. 4-2-7: Strains along $[1\ 0\ 0]_S$, $[0\ 1\ 0]_S$ and $[0\ 0\ 1]_S$ for different types of textures (10000 grains) as a function of maximum rotation angle: (a) Cube (b) Goss (c) Brass (d) Copper (e) E-orientation (f) α -Fibre. Red, green and black dots in every diagram denote the strain along $[1\ 0\ 0]_S$, $[0\ 1\ 0]_S$ and $[0\ 0\ 1]_S$ for 10000 randomly distributed grains, with the values of 0.2636, -0.1633 and -0.1635, respectively.

4-2-4 Comparison with literature data

Comparisons are made in this part between the calculated results and some published literature data. As emphasized previously, it is nearly impossible to get a grain fully twinned. Due to work hardening of the austenite, the movement of twin boundaries is always stopped by an increase of dislocation density at the later stages of deformation [Choi *et al.*, 1999; Allain *et al.*, 2004a; Vercammen *et al.*, 2004a]. Consequently, it is estimated that the maximum twin fraction should be less than 0.6 [Choi *et al.*, 1999]. It is also a fact that usually two or three twinning systems operate in one grain [Grassel *et al.*, 2000; Allain *et al.*, 2004b; Vercammen, 2004b]. And at the same time it is usually impossible in practice to get a matrix without texture. Thus the calculations of a textured matrix ($\theta = 45^\circ$) with the most favored three twinning systems operating, each of which has a volume percent of 20%, were made and the results are listed in Table 4-2-7.

Table 4-2-8 lists the published data about the strain of TWIP steel in tensile testing.

Comparing the calculated results with the experimental results, the difference is large. The experimental strains are higher than 0.45 for all cases while the true strain calculated is generally less than 0.13 under previous condition. Even for the maximum strain in all the previous calculation, i.e. when the matrix is randomly oriented and fully twinned by the most favorable twinning system, the deformation strain from twinning system itself is 0.2635, which is still far away from the total observed elongation.

This happens because beside the twinning shear, there are other factors which also contribute to the large strain of TWIP steel, such as dislocation slip; interaction between differently oriented twin plates and interaction between dislocations and twin plates together increase the strain hardening rate, leading an increase in the strain hardening coefficient. In a full model of TWIP steel, all these factors would need to be taken into the account.

Table 4-2-7: 10000 grains, the most favorable three twinning systems are operating, each with 20% volume percent, maximum rotation angle θ : 45° .

Matrix texture	Strain along $[1\ 0\ 0]_s$	Strain along $[0\ 1\ 0]_s$	Strain along $[0\ 0\ 1]_s$
Cube	0.1249	-0.0684	-0.0693
Goss	0.1249	-0.0692	-0.0685
Brass	0.1304	-0.0685	-0.0758
Copper	0.1288	-0.0710	-0.0714
α -fibre	0.1299	-0.0772	-0.0667

Table 4-2-8 Experimental data about the elongation of TWIP steel [Grassel *et al.*, 2000]. Values in the round brackets are the converted true strain ϵ .

Composition / wt. %	uniform elongation (ϵ)	total elongation (ϵ)
Fe-25.5Mn-3.9Si-1.8Al	58% (0.4574)	69% (0.5247)
Fe-26.5Mn-3.0Si-2.8Al	80% (0.5878)	94% (0.6627)
Fe-25.6Mn-2.0Si-3.8Al	72% (0.5423)	88% (0.6313)
Fe-28.7Mn-4.0Si-2.0Al	63% (0.4886)	75% (0.5596)
Fe-29.2Mn-3.0Si-2.8Al	75% (0.5596)	88% (0.6313)
Fe-30.6Mn-2.0Si-3.9Al	65% (0.5008)	84% (0.6098)

4-2-5 Multi-axial stresses

In all the cases considered above, the stress status is uniaxial tension. There are circumstances where combinations of stresses are imposed in the course of deformation such as cold rolling and cup drawing. In the case of an idealized cup drawing [Zhou *et al.*, 1996] as shown in Figure 4-2-8 (a), during the drawing of the flange into the die, the material in front of the punch is subjected to tension along the circumferential direction and its stress tensor can consequently be simplified as

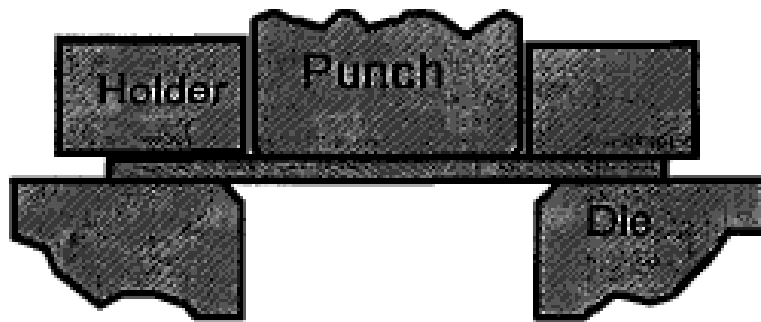
$$(S \sigma S) = \sigma \begin{pmatrix} 1 & 0 & 0 \\ 0 & 1 & 0 \\ 0 & 0 & 0 \end{pmatrix}$$

A similar calculation was done by following the same procedure as that in the case of uniaxial tensile testing. Three different types of matrices, Random, Cube and Brass, were calculated, supposing that the most favored three twinning systems operating. The results are listed in Table 4-2-9

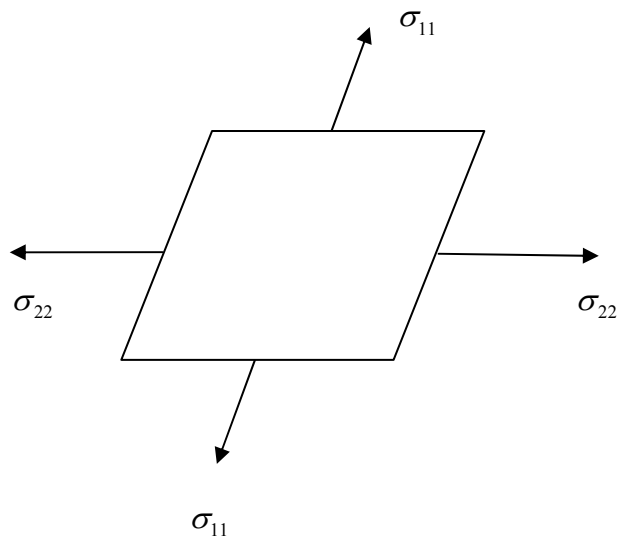
Table 4-2-9: Strains for the idealized cup drawing. 10000 Grains, the most favorable three twinning systems are operating, each with 20% volume percent.

	Strain along	Strain along	Strain along
Matrix texture	$[1\ 0\ 0]_s$	$[0\ 1\ 0]_s$	$[0\ 0\ 1]_s$
Random	0.0663	0.0673	-0.1487
Cube	0.0848	0.0853	-0.1955
Brass	0.0696	0.0514	-0.1333

The results show that for both random and cube type matrix, the strains along $[1\ 0\ 0]_s$ and $[0\ 1\ 0]_s$ are nearly the same, which is good for cup drawing. However for the Brass type matrix, the strain along $[1\ 0\ 0]_s$ is larger than the strains along $[0\ 1\ 0]_s$. This is definitely a disadvantage for cup drawing and consequently the TWIP steel with Brass texture is not a good candidate material for cup drawing.



(a)



(b)

Fig. 4-2-8 (a) Cross-section of a plane strain drawing operation. (b) During drawing of the flange into the die, the material in front of the punch is subjected to tension along the circumferential direction.

4-3 Conclusions

4-3-1 The strain

As calculated, the contribution from twinning to the large elongation of TWIP steel is small, even when the whole piece is 100% twinned by the most favored system. However, twinning does have a major effect on the observed elongation. This is because not only are the grains refined by twin boundaries, but there would be interactions between differently oriented twin plates and between dislocations and twins resulting in strain hardening which may be beneficial in avoiding plastic instabilities.

In a full model of the strain of TWIP steel, all those factors should be taken into account. However in the published literature, the modeling of TWIP effect on work hardening [Bouaziz and Guelton, 2001; Allain *et al.*, 2004a] does not take the contribution from twinning strain into account.

Twinning strain for polycrystalline austenite is influenced by texture. The austenite TWIP steel with textures having type **II** direction, i.e. $\langle 1\ 1\ 0 \rangle_{M_1}$ parallel to $[1\ 0\ 0]_S$ is found to have the maximum strain; those textures with type **III** direction, i.e. $\langle 1\ 1\ 1 \rangle_{M_1}$ parallel to $[1\ 0\ 0]_S$ has medium strain and strain from those with type **I** direction, i.e. $\langle 1\ 1\ 1 \rangle_{M_1}$ parallel to $[1\ 0\ 0]_S$ is smallest.

4-3-2 The texture

The model can, to some extent, estimate the evolution of texture in TWIP steel during deformation, if it is not severely deformed and if the stress state under which the steel is deformed is precisely known. In general, the deformation texture of any kind of material may be modeled as long as its deformation mechanism is mechanical twinning. However this model needs to be improved in two respects:

First the exact intensity of texture cannot be modeled at the moment because the contribution of volume fraction to the intensity of texture has not been taken into account.

Second in the prediction of the positions of textures, this model does not take the effects of dislocation and grain rotation into account.

Chapter 5

Summary and Future Work

5-1 Summary

Austenitic TWIP steels have a low stacking fault energy ($\gamma_{SFE} \sim 30 \text{ mJ m}^{-2}$) and consequently present extensive mechanical twinning when subjected to plastic deformation. Direct consequences of this phenomenon are a combination of both high strength and ductility and a change in crystallographic texture. The main aim of this research was to develop a general physical model to quantitatively estimate the strain of twin in a polycrystalline specimen and to qualitatively estimate the texture change due to twinning.

A general model has been constructed based on the mathematical crystallography of twinning and FORTRAN programs have been written to implement the calculation of transformation strain and transformation texture. In the model, an interaction energy criterion is used for the selection of operating twinning system and the calculation was flexible: on the one hand, the number of operating twinning systems could be chosen to be as large as 12, but since in most literature no more than three twinning systems are observed simultaneously in any grain, this number was therefore generally suggested to be chosen as one, two or three; on the other hand, the volume fraction for each twin was arbitrary but because the relationship between it and the interaction energy is not quite understood, hence the twin volume fraction is chosen to be equal for every operating system.

For the calculation of strain, it was found that the strain of a polycrystalline specimen is influenced by twinning volume fraction and texture. Details of these factors' effects on strain have also been discussed. Generally, in the case of tensile

testing, as the number of twinning systems increases, the strain due to twinning along the tensile direction decreases, if the total twin volume percent keeps constant; for most textures such as Cube, Goss, Brass and Copper, as its intensity decreases strain along TD or TeD increases; but for some other textures such as E-oriented texture, as its intensity increases, the strain increases at beginning and then followed by a decrease until it approaches a constant value. In addition, deformation strain due to twinning as a function of deformation direction was also calculated for a single crystal and the result was found very useful in interpreting the deformation properties of textured polycrystalline specimen. It was found that it is the difference in tensile direction that makes the difference in strain behavior between different types of textures.

The calculation also showed that the true strain from twinning has a reasonable value less than 0.15, which is lower than the true strain of TWIP steel which generally has a value above 0.45.

For the calculation of texture, the model was found to be valid in orientation change in the case of tensile testing. However in the case of cold rolling, it was found difficult to predict texture evolution using this twinning based model. This failure is for two reasons: the difficulty in finding the precise stress tensor which is vital in twinning variants selection and, the ignorance of grain rotation and dislocation gliding, both of which are normal in the case of severe cold rolling.

5-2 Future work

All the results presented in this thesis should be considered as work in progress, and as such, there are many potential directions for continued research.

For the transformation strain, tensile testing experiment on single crystal can be conducted to firstly verify the strain energy criteria and secondly, to examine the relationship between volume fraction of twin and strain energy. Once these factors have been determined, a more precise calculation would be possible.

For the calculation of texture, in the case of tensile testing, only the position change can be calculated at the moment, so next step would be the incorporation the calculation of intensity as a function of twin volume fraction. In the case of cold

rolling, not only the external stress status needs to be precisely determined, but also the effective stress status at any point in the specimen during the cold rolling should be included in the model. Further more, for the severely cold rolled specimen, the influences of dislocation glide and grain rotation should also be incorporated in the model. This may be accomplished by coupling the present twinning based model with traditional theories about texture evolution during cold rolling.

On the other hand, the model assumes that twinning is independent of interactions between grains. In a polycrystalline material, there must be strain compatibility between different grains, which may tend to reduce variant selection. Hence the model also needs to take this into account.

A series of experiments on sheet TWIP steel are also planned.

The variant selection criterion needs to be experimentally proven and the relationship between the interaction energy and twin volume fraction can also be found by experiment.

The idea of predicting simultaneously the crystallographic texture and anisotropy of strain is novel in the content of TWIP steel and the model estimates both. This will be experimentally verified by measuring both the anisotropic strain and texture.

The balance between dislocation plasticity and twinning of TWIP steel will be investigated by tensile testing studies at different testing temperature and atomic force microscopy (AFM) can be used to determine whether the twinning strain is drastically accommodated.

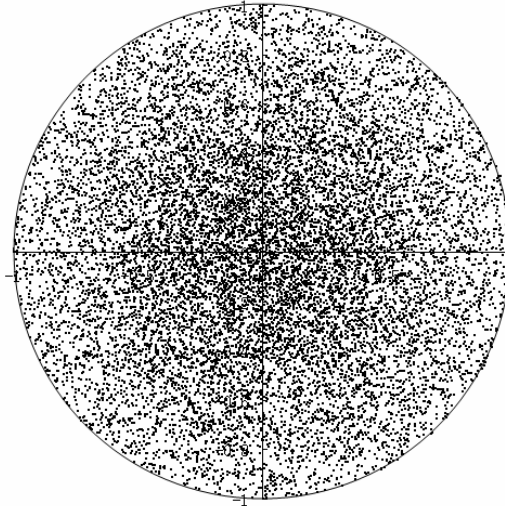
Finally, the twinning effect must be affected by austenite grain size, hence influences the strain and texture evolution. Tensile testing experiments on samples with different grain size are also planned.

Appendix A

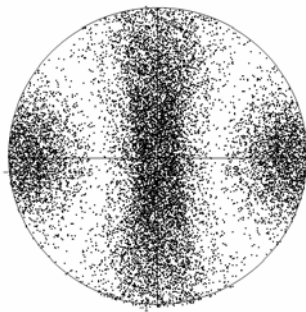
100 Pole figures for Random Orientation and its Twinning systems

(Tension along [100]s)

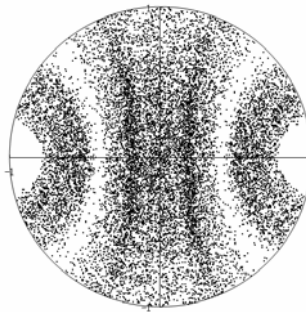
Matrix



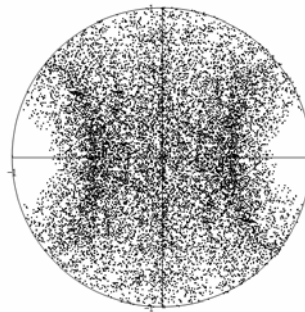
Twin-01



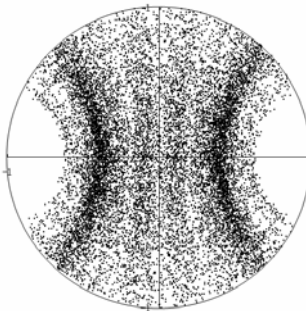
Twin-02



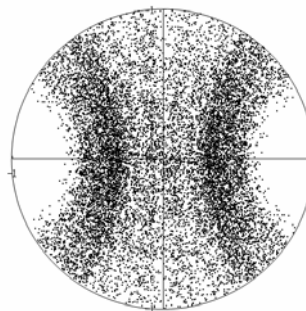
Twin-03



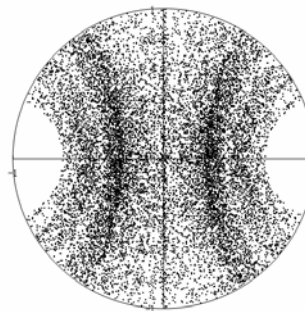
Twin-04



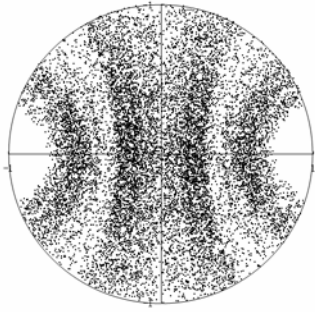
Twin-05



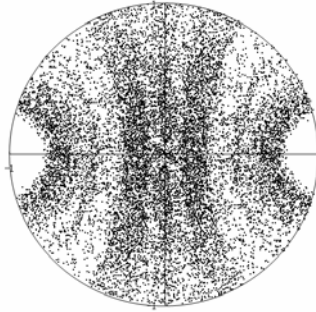
Twin-06



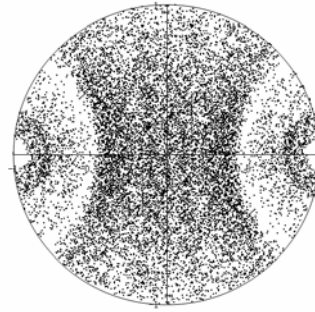
Twin-07



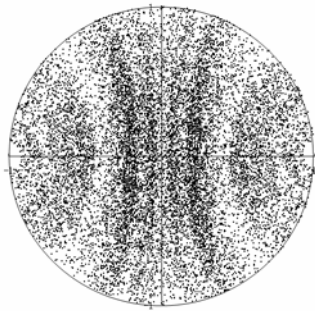
Twin-08



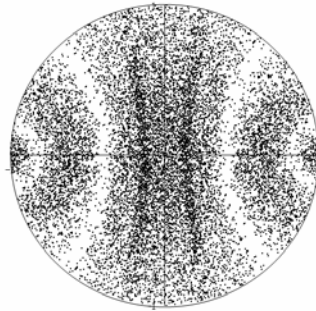
Twin-09



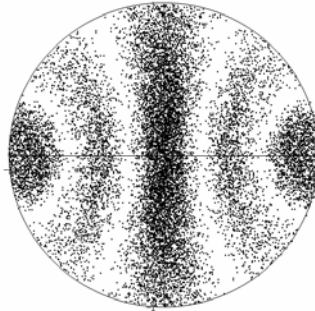
Twin-10



Twin-11

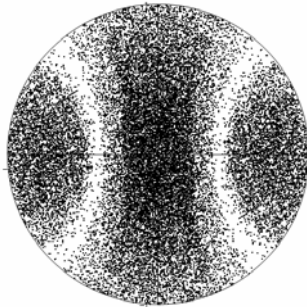


Twin-12

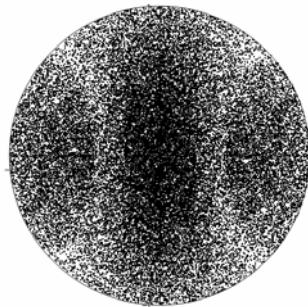


Superposition:

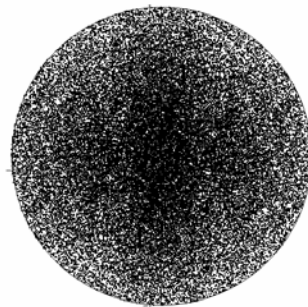
Twin-1-2



Twin-1-2-3



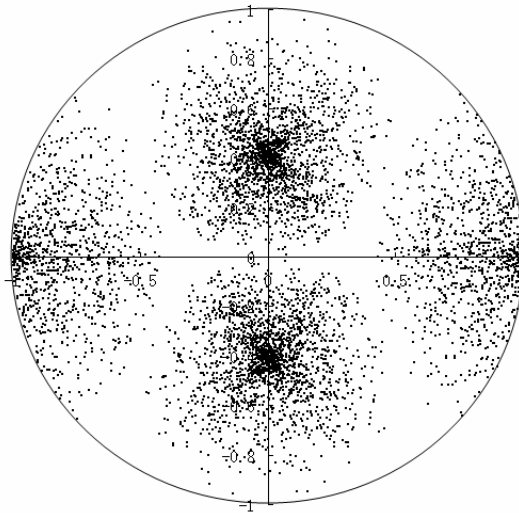
Twin-1-2-3-4



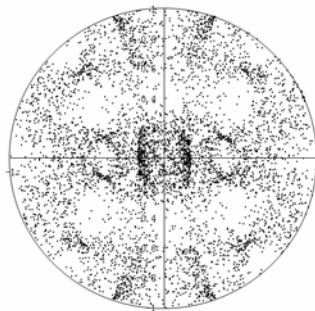
100 Pole figures for Goss Orientation and its Twinning systems

(Tension along [100]s)

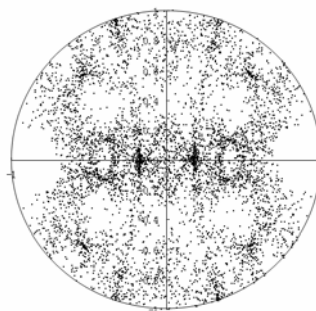
Matrix



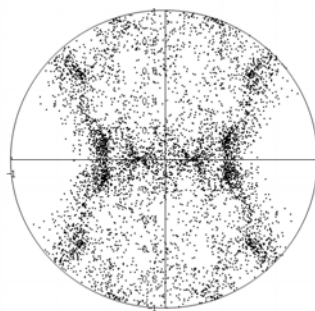
Twin-01



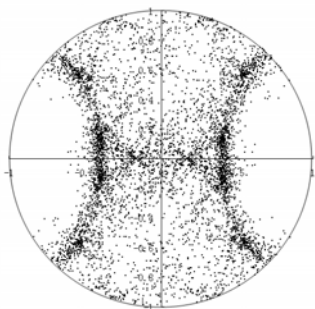
Twin-02



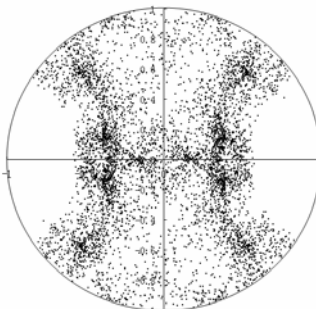
Twin-03



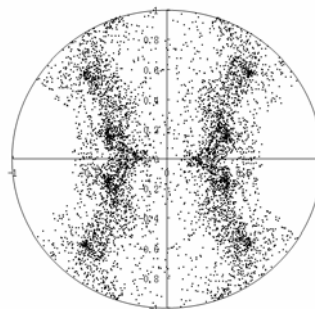
Twin-04



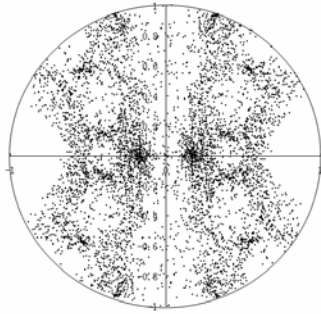
Twin-05



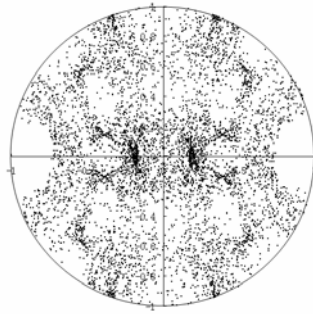
Twin-06



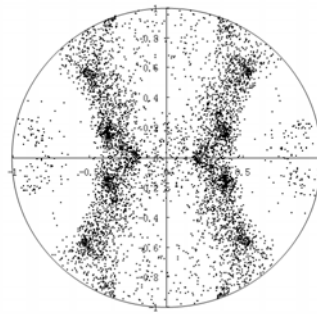
Twin-07



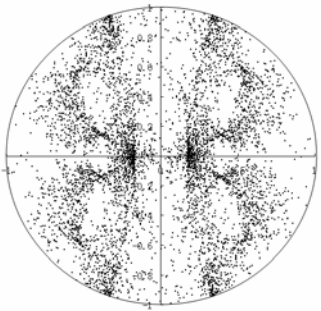
Twin-08



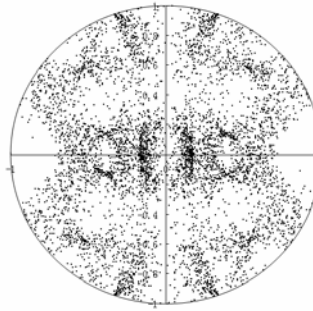
Twin-09



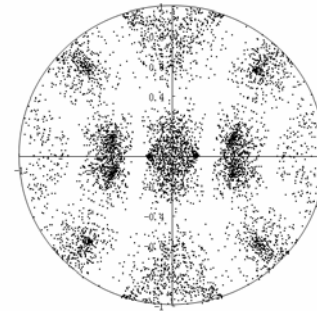
Twin-10



Twin-11

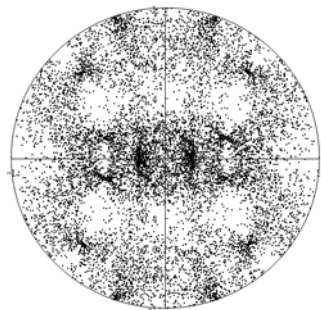


Twin-12

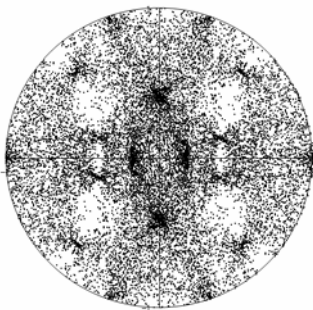


Superposition:

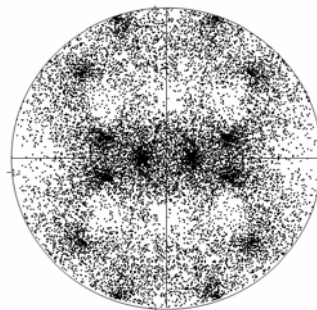
Twin-1-2



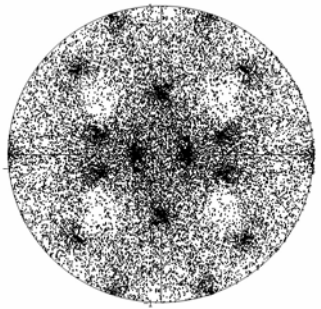
Twin-1-2-3



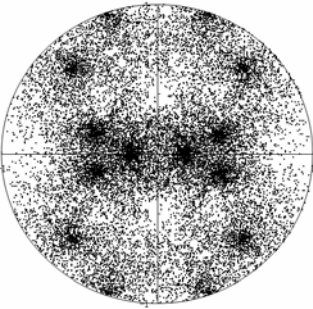
Twin-1-2-3-4



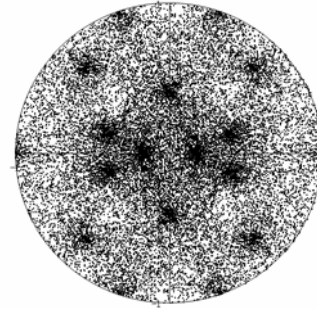
M-T-1-2



M-T-1-2-3



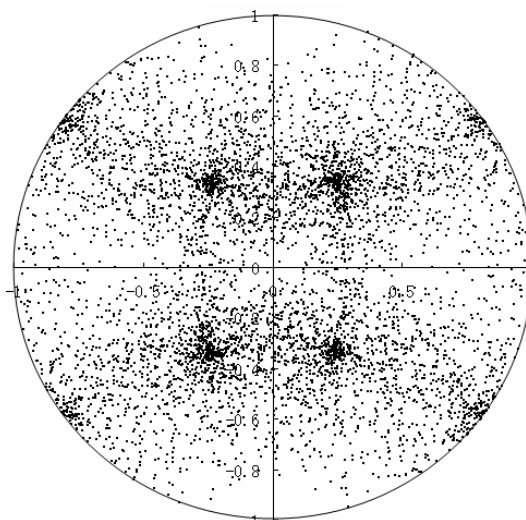
M-T-1-2-3-4



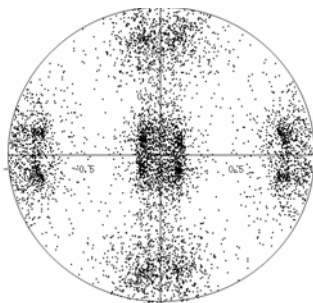
100 Pole figures for Brass Orientation and its Twinning systems

(Tension along [100]s)

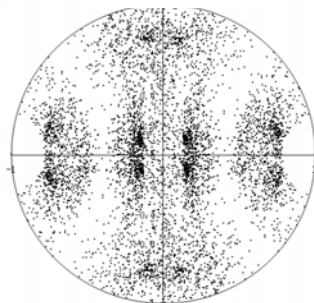
Matrix



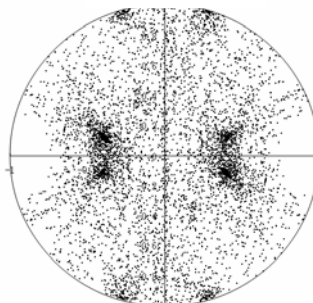
Twin-01



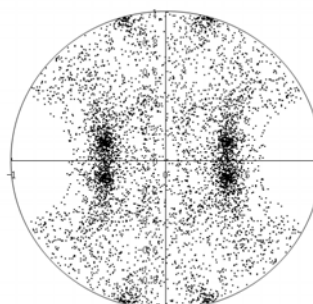
Twin-02



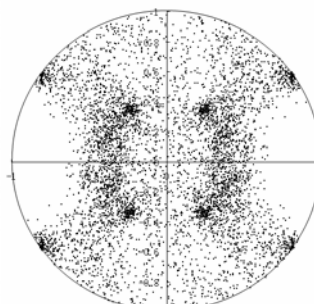
Twin-03



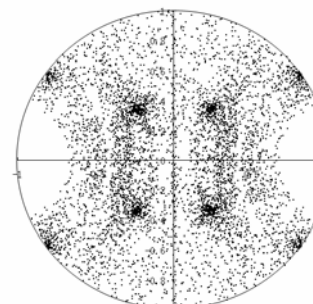
Twin-04



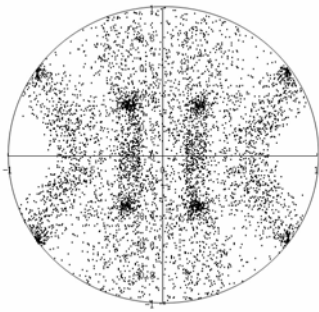
Twin-05



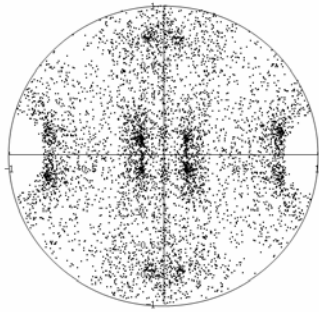
Twin-06



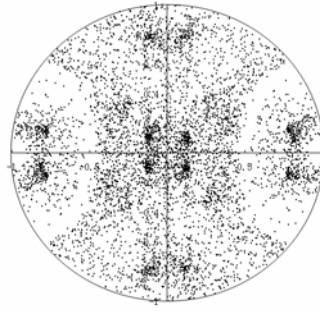
Twin-07



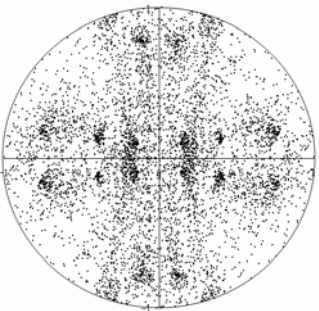
Twin-08



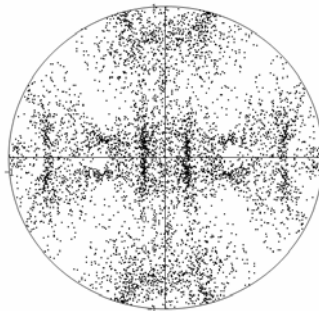
Twin-09



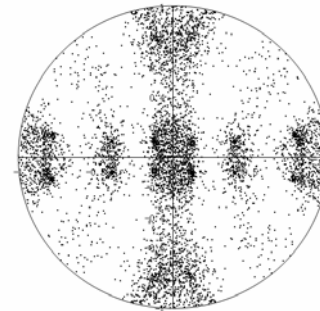
Twin-10



Twin-11

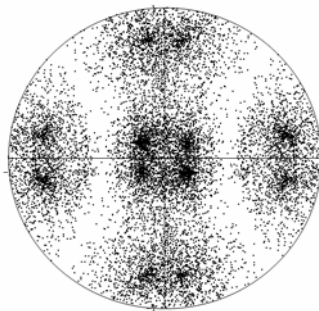


Twin-12

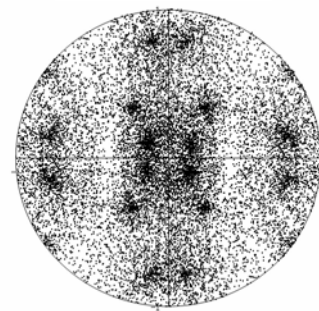


Superposition:

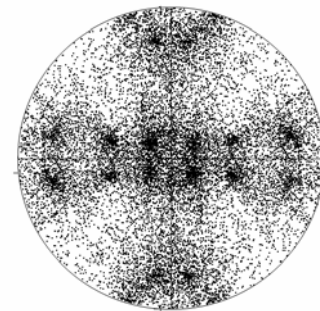
Twin-1-2



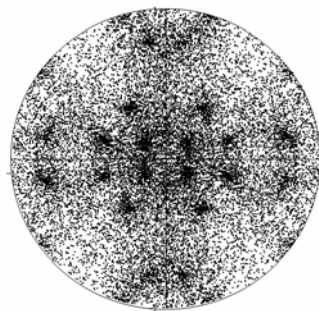
Twin-1-2-3



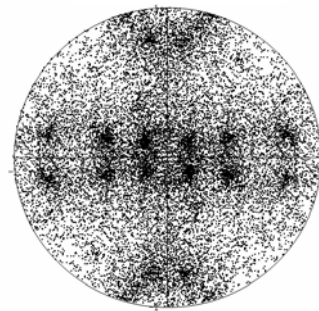
Twin-1-2-3-4



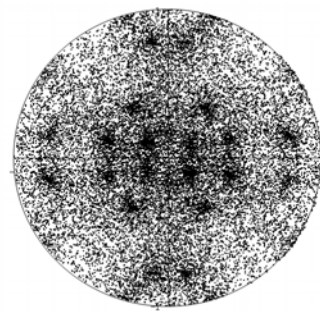
M-T-1-2



M-T-1-2-3



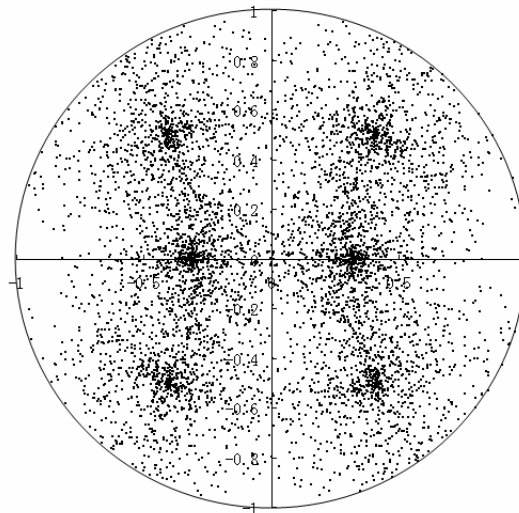
M-T-1-2-3-4



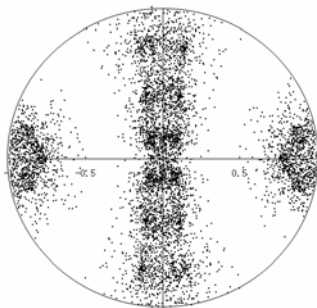
100 Pole figures for Brass Orientation and its Twinning systems

(Tension along $[100]_s$)

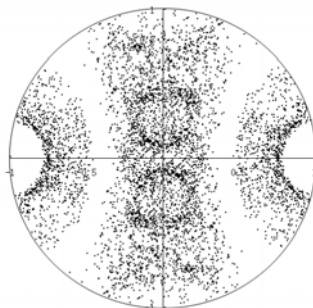
Matrix



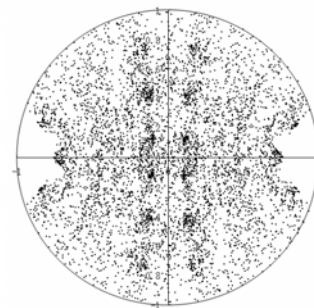
Twin-01



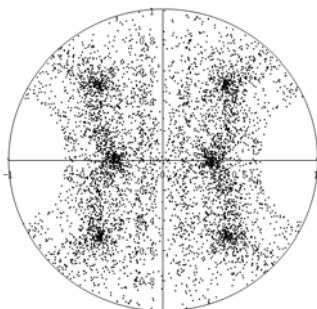
Twin-02



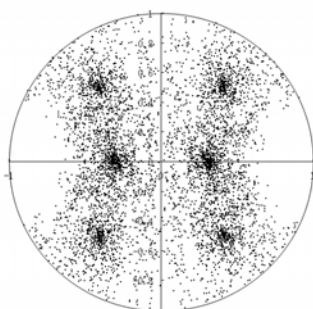
Twin-03



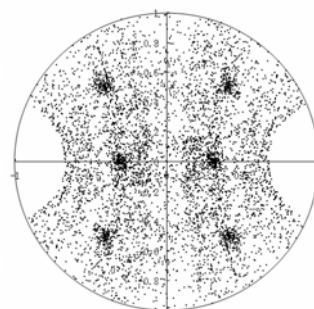
Twin-04



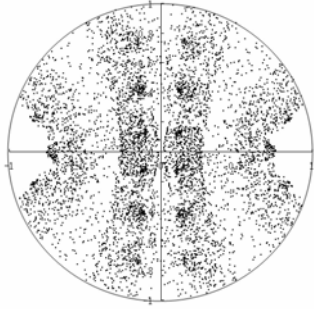
Twin-05



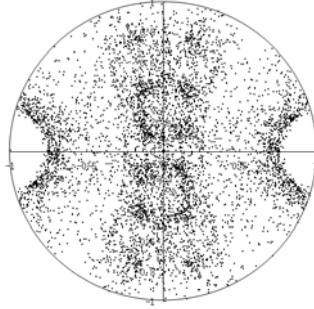
Twin-06



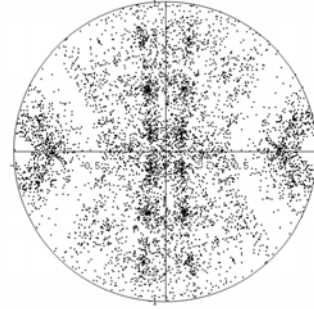
Twin-07



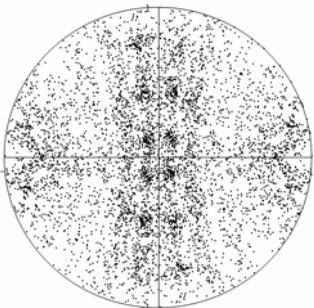
Twin-08



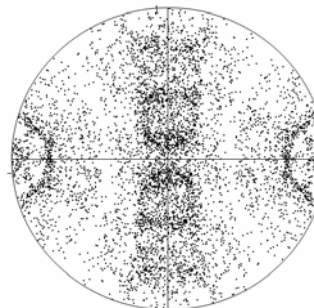
Twin-09



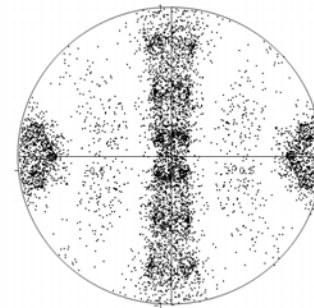
Twin-10



Twin-11

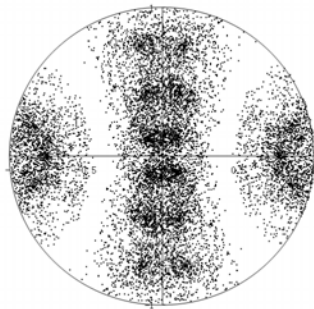


Twin-12

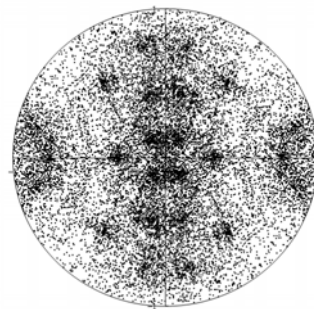


Superposition:

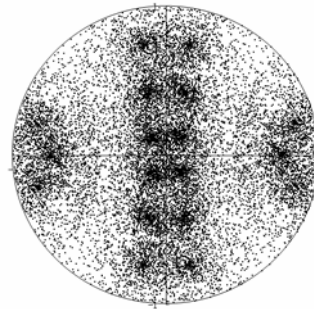
Twin-1-2



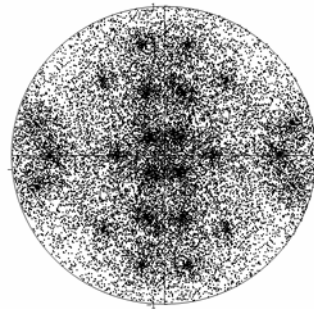
Twin-1-2-3



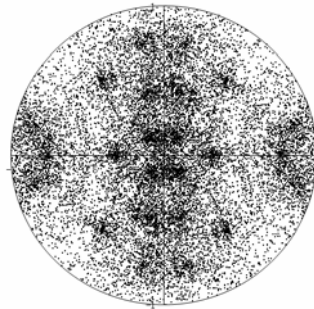
Twin-1-2-3-4



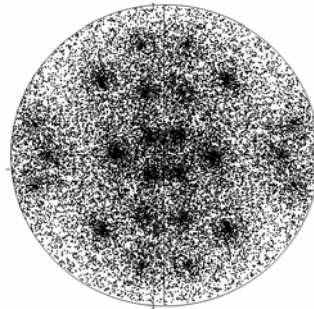
M-T-1-2



M-T-1-2-3



M-T-1-2-3-4



Appendix B

Program MAP_STEEL_TWIP

This appendix presents the model described in Chapter 3 and associated documentation following the MAP format,

<http://www.msm.cam.ac.uk/map/mapmain.html>.

1. Provenance of Source Code

Bo Qin and H. K. B. H. Bhadeshia,
Computation Metallurgy Lab (CML),
Graduate Institute of Ferrous Technology (GIFT),
Pohang University of Science and Technology (POSTECH),
San 31, Hyoja-Dong, Nam-gu,
Pohang, Kyungbuk Republic of Korea
E-mail: zebraf@postech.ac.kr
Added to MAP: July 2007.

2. Purpose

A program for the calculation of texture change due to twinning and true strain from twinning, as a function of twinning volume fraction, texture type and its intensity.

3. Specification

Language: FORTRAN
Product form: Source Code (Windows and Unix)
Operating System : Tested on Linux and PC.

4. Description

MAP_STEEL_TWIP contains the programs which enable the user to calculate the

true strain from twinning and resulting texture change. The results are a function of stress state, number of operating twinning systems, texture type and the intensity of texture. Once uncompressed, MAP_STEEL_TWIP contains:

MAP_STEEL_TWIP_TEXTURE_AND_STRAIN.f

The source code for the calculation of true strain and texture of polycrystalline austenite.

MAP_STEEL_TWIP_STRAIN_INTENSITY.f

The source code for the calculation of true strain as a function of intensity of texture.

MAP_STEEL_TWIP_STRAIN_SINGLE_CRYSTAL.f

The source code for the calculation of orientation dependence of strain for austenite single crystal.

MAP_STEEL_TWIP_TEXTURE_AND_STRAIN.exe

MAP_STEEL_TWIP_STRAIN_INTENSITY.exe

MAP_STEEL_TWIP_STRAIN_SINGLE_CRYSTAL.exe

The executable programs, PC only.

READ_ME.txt

Files containing the instructions for running the program.

5. References

1. B. Qin, Master of Engineering (M. Eng) thesis, Chapters 2 and 3, Pohang University of Science and Technology, 2007.
2. H. K. D. H. Bhadeshia, Geometry of Crystals, Chapters 1, 2 and 3, University of Cambridge.

6. Input Parameters

The user is required to input the stress tensor, number of operating twinning systems and the corresponding volume fractions, pole figures of interesting (i.e. 100, 110 and 111 pole figures), full Euler space or section. Details are given in 'READ_ME.TXT'

7. Output Parameters

The default output parameters are: true strains along , and ; two-dimensional coordinates of the interested poles, for both matrix and 12 twinning systems; three-dimensional coordinates of Euler angles.

Keywords

TWIP, Deformation Strain, Deformation Texture

Bibliography

Adamczyk, J. and Grajcar, A., *Journal of Materials Processing Technology*, **162-163**: 267-274, 2005.

Allain, S., Chateau, J. P. and Bouaziz, O., *Materials Science and Engineering A*, **387-389**: 143-147, 2004a.

Allain, S., Chateau, J. P., Dahamoun, D. and Bouaziz, O., *Materials Science and Engineering A*, **387-389**: 272-276, 2004b.

Asgari, S., El-Danaf, E., Kalidindi, S. R. and Doherty, R. D., *Metallurgical and Materials Transactions A*, **128**: 1781-1795, 1997.

Bhadeshia, H. K. D. H. *Geometry of Crystals*, 2nd edition, Institute of Materials, London, 2001.

Bhadeshia, H. K. D. H., *ISIJ International*, **42**: 1059-1060, 2002.

Bhadeshia, H. K. D. H. and Honeycombe, R. W. K. *Steels: Microstructure and Properties*, 3rd edition, Butterworths-Heinemann, London, 2006.

Biedenharn, L. C. and Louck, J. D. *Angular Momentum in Quantum Physics*, Addison-Wesley, MA, 1981.

Bouaziz, O. and Guelton, N., *Materials Science and Engineering A*, **319-321**: 246-249, 2001.

Bunge, H. J. *Texture Analysis in Materials Science*, Butterworths-Heinemann, London, 1982.

Callister, W. D. *Fundamentals of Materials Science and Engineering: An Integrated Approach*, John Wiley, New York, 2004.

Chen, M. W., Ma, E., Hemker, K. J., Sheng, H. W., Wang, Y. M. and Cheng, X. M., *Science*, **300**: 1275 -1277, 2003.

Choi, H. C., Ha, T. K., Shin, H. C. and Chang, Y. W., *Scripta Materialia*, **40**: 1171-1177, 1999.

Christian, J. W. and Laughlin, D. E., *Acta Metallurgica*, **36**: 1617-1642, 1988.

Christian, J. W. and Mahajan, S., *Progress in Materials Science*, **39**: 1-157, 1995.

Decooman, B. C., *Current Opinion in Solid State and Materials Science*, **8**: 285-303,

2004.

El-Danaf, E., Kalidindi, S. R. and Doherty, R. D., *Metallurgical and Materials Transactions A*, **30**: 1223-1233, 1999.

Frommeyer, G., Brux, U. and Neumann, P., *ISIJ International*, **43**: 438-446, 2003.

Grassel, O. and Frommeyer, G., *Material Science and Technology*, **14**: 1213-1216, 1998.

Grassel, O., Kruger, L., Frommeyer, G. and Meyer, L. W., *International Journal of Plasticity*, **16**: 1391-1409, 2000.

Gray-III, G. T., *Acta Metallurgica*, **36**: 1745-1754, 1988.

Hirsch, J., Locke, K. and Hatherly, M., *Acta Metallurgica*, **36**: 2905-2927, 1988.

Hull, D. and Bacon, D. J. *Introduction to Dislocations*, 4th edition, Butterworth-Heinemann, London, 2001.

IISI, *Reports on Advanced High Strength Steel: Application Guidelines*, 2006.

Ishida, K. and Nishizawa, T., *Transition of Japan Institute of Metal*, **15**: 225-259, 1974.

Karaman, I., Sehitoglu, H., Beaudoin, A. J., Chumlyakov, Y. I., Maier, H. J. and Tome, C. N., *Acta Metallurgica*, **48**: 2031-2047, 2000.

Karaman, I., Sehitoglu, H., Chumlyakov, Y. I. and Maier, H. J., *Journal of Metals*, **54**: 31-37, 2002.

Karaman, I., Sehitoglu, H. and Gall, K., *Scripta Materialia*, **38**: 1009-1015, 1998.

Kundu, S. *Importance of Shape Deformation in Steels: Transformation Strain and Texture*, PhD thesis, University of Cambridge, 2007.

Lacombe, P., Baroux, B. and Beranger, G. *Stainless Steels*, Les Editions de Physiques, Les Ulis, 1993.

Lis, J., Lis, A. K. and Kolan, C., *Journal of Materials Processing Technology*, **162-163**: 350-354, 2005.

Mahajan, S. and Chin, G. Y., *Acta Metallurgica*, **21**: 173-179, 1973.

Meng, L., Yang, P., Xie, Q., Ding, H. and Z.Tang, *Scripta Materialia*, **56**: 931-934, 2007.

- Pan, J. S., Gong, J. M. and Tian, M. B. *Fundamental of Materials Science (In Chinese)*, Tsinghua University Press, Beijing, 1998.
- Panda, S. K., Kumar, D. R., Kumar, H. and Nath, A. K., *Journal of Materials Processing Technology*, **183**: 321-332, 2007.
- Pirouz, P., *Scripta Materialia*, **21**: 1463-1466, 1987.
- Sarwar, M., Ahamd, E., Qureshi, K. A. and Manzoor, T., *Materials & Design*, **28**: 335-340, 2007.
- Srivastava, A. K., Bhattacharjee, D., Jha, G., Gope, N. and Singh, S. B., *Material Science and Engineering A*, **445-446**: 549-557, 2007.
- Srivastava, A. K., Jha, G., Gope, N. and Singh, S. B., *Material Characterization*, **57**: 127-135, 2006.
- Sun, S. J. and Pugh, M., *Materials Science and Engineering A*, **335**: 298-308, 2002.
- Suzuki, H. and Barrett, C. S., *Acta Metallurgica*, **6**: 156-165, 1958.
- Vercammen, S. *Processing and Tensile Behavior of TWIP Steel: Micro-structural and Textural Analysis*, PhD thesis, Katholieke Universiteit Leuven, 2004b.
- Vercammen, S., Blanpain, B., Cooman, B. C. D. and Wollants, P., *Acta Metallurgica*, **52**: 2005-2012, 2004a.
- Wei, X. C., Fu, R. Y. and Lin, L., *Material Science and Engineering A*, in press, 2007.
- Yang, P., Xie, Q., Meng, L., Ding, H. and Tang, Z., *Scripta Materialia*, **55**: 629-631, 2006.
- Zhao, H., Rama, S. C., Barber, G. C., Wang, Z. and Wang, X., *Journal of Materials Processing Technology*, **128**: 73-79, 2007.
- Zhou, Y., Jonas, J. J. and Neale, K. W., *Acta Metallurgica*, **44**: 607-619, 1996.